IONIC POLYMER-METAL COMPOSITE (IPMC): MODELING AND BIO-INSPIRED SENSING APPLICATIONS

By

Montassar Aidi Sharif

A DISSERTATION

Submitted to
Michigan State University
in partial fulfillment of the requirements
for the degree of

Electrical Engineering - Doctor of Philosophy

2019

ABSTRACT

IONIC POLYMER-METAL COMPOSITE (IPMC): MODELING AND BIO-INSPIRED SENSING APPLICATIONS

By

Montassar Aidi Sharif

Ionic polymer-metal composite (IPMC) is a class of electroactive polymers with built-in actuation and sensing capabilities. In this dissertation, the modeling and several bio-inspired sensing applications of IPMC are investigated computationally and experimentally. First, physics-based modeling is studied for a tubular IPMC sensor under pure torsional stimulus. With inspiration from the fish lateral line system, IPMC is then explored for several flow-sensing applications, where modeling of fluid-structure interactions, sensor design, and experimental validation are conducted. Specifically, the sensitivities of IPMC-based artificial superficial and canal neuromasts are examined in terms of their dimensions, shapes, and stiffness properties. A canal lateral line-inspired pressure sensor is further proposed and developed. Another novel flow velocity sensor is proposed, which exploits self-generated von Kármán vortices to produce vibrations that are correlated with the flow speed. Finally, inspired by the vestibular system, an angular acceleration sensor is proposed.

Firstly, the Poisson-Nernst-Planck (PNP) model is used to describe the fundamental physics within the tubular IPMC under torsional excitation, where it is hypothesized that the anion concentration is coupled to the sum of shear strains induced by the torsional stimulus. Finite element simulation is conducted to solve for the torsional sensing response, where some of the key parameters are identified based on experimental measurements using an artificial neural network. Additional experimental results suggest that the proposed model is able to capture the torsional

sensing dynamics for different amplitudes and rates of the torsional stimulus.

Secondly, Inspired by the fish lateral line system, the sensitivity of IPMC-based artificial superficial and canal neuromasts are examined in terms of their dimensions, shapes, and stiffness properties. The PNP model is again used to describe the fundamental physics within the IPMC, where the bending stimulus due to the cupula displacement is coupled to the PNP model through the cation convective flux term. Comparison of the numerically computed cupula displacement with an analytical approximation is conducted.

Thirdly, a novel pressure difference sensor inspired by the canal lateral line is proposed. The sensor output is experimentally characterized as the fish-like body is rotated with respect to a dipole source, which confirms that the sensor is capable of capturing the pressure between the two pores. Finite element modeling that capture fluid-structure interactions and IPMC physics are conducted to shed light on the sensor behavior. Finally, the utility of the sensor in underwater robotics is illustrated via orientation of the fish-like body towards the dipole source using feedback from the proposed sensor.

Fourthly, a novel IPMC flow sensor is proposed that exploits self-generated von Krmn vortices to produce vibrations, the frequency and amplitude of which are correlated with the stream flow. Experiments are conducted in a flow channel to measure the IPMC output and the free-end displacement of the sheath under different flow speeds. The results indicate that the proposed sensor structure can produce significant oscillatory signals for effectively decoding the flow speed.

Finally, inspired by the vestibular system, an angular acceleration sensor by exploiting IPMC sensor is proposed. The sensor has one 3D-printed canal filled with a viscous fluid. Finite-element simulation based Experimental results involving different angular acceleration stimuli show that the sensor is able to capture the angular acceleration for different rates of rotational stimulus.

Dedicated to my parents, my wife, and my kids with all my love and gratitude.

ACKNOWLEDGMENTS

I would like to express my sincere gratitude to my advisor, Prof. Xiaobo Tan, for providing me the opportunity to be part of his team in Smart Microsystems Lab during my doctoral study. His valuable guidance and generous encouragement benefited me a lot in my research and will continue to benefit me for my future career.

I want to thank all my Ph.D. committee members: Prof. Guoming Zhu, Prof. Linxin Dong, and Prof. Wen Li at Michigan State University, for kindly joining my advisory committee and offering me insightful comments. I also thank our research collaborators, Prof. Matthew McHenry at University of California, Irvine, Prof. Derek A. Paley at University of Maryland, and Prof. Kalyanmoy Deb at Michigan State University, for their constant support and kind help in my research projects.

I would like to thank the ECE technical staff, ECE cleanroom committee, and ECE cleanroom colleagues for their advice and assistance on my fabrication work in ECE cleanroom at Michigan State University, in particular, Brian Wright and Karl Dersch. I would also like to thank Dr. Sandrine Martin in the Lurie Nanofabrication Facility (LNF) for her help on my fabrication work in LNF at University of Michigan.

I am grateful to all my colleagues and friends who have offered help in various ways, especially to Mohammed Al-Rubaiai, Dr. Hong Lei, John Thon, Dr. Feitian Zhang, Dr. Jianxun Wang, Dr. Sanaz Behbahani, Dr. Jun Zhang, Dr. Ali Ahrari, Jason Freeberg, Demetris Coleman, Hongyang Shi, Maria Castano, Thassyo Pinto, Pratap Bhanu Solanki, Osama En-Nasr, Cody Thon, Husien Hasan, Ameer Janabi, Ali Al-Awadi, and Maher Al-Sahlani. Their encourgments, comments, and collaboration have helped my research a lot. Thanks also to all of the administrators and staff

members in the ECE department for their assistance over the years.

I would also like to acknowledge the financial support from the Office of Naval Research (N000141512246) and the Higher Committee for Educational Development in Iraq (HCED).

Most of all, I am foremost thankful for my family. I would like to thank my mother, Kareema Khudier Faraj, my father, Aidi Sharif, and my brother, Dr. Montadher Aidi Sharif, for their all-enduring love and everlasting support in this life journey. I would like to express my ultimate gratitude to my brothers and sisters for their everlasting support to pursue my dreams. Special thanks to my wife, Shaimaa Faisal Jasim – I am deeply grateful for her selfless love, support, and encouragement, and to my kids for their love. This dissertation would not have been possible without their years of encouragement and continuous support in both good times and bad times.

TABLE OF CONTENTS

LIST OF TABLES

LIST OF FIGURES

Chapter 1

Introduction

Ionic polymer-metal composites (IPMCs) have inherent sensing properties. They hold strong promise for versatile applications as sensors for their direct mechanosensory property and inherent polarity. A physics-based dynamic model and novel bio-inspired sensing applications of IPMCs are presented in this dissertation. In this introduction, a brief background is first presented, followed by a summary of contributions of this work.

1.1 Ionic Polymer-Metal Composites

Ionic-polymer metal composites (IPMCs) represent a class of electroactive polymers (EAPs), and have built-in actuation and sensing capabilities [3–5]. Basically, IPMCs can convert mechanical energy into electrical energy and vice versa [6]. In the past two decades, they have received significant interest because of their inherent polarity, high sensitivity, and ability to work in wet and dry environments. They are also bio-compatible and amenable to microfabrication [7–11]. In particular, they hold strong promise for versatile applications because they require low-actuation voltages to generate large bending deformation, work in both air and water without stringent packaging requirements, and exhibit direct electromechanical and mechanoelectric transduction, which minimizes the structural complexity in implementation as actuators and sensors [12, 13].

An IPMC typically consists of a thin ion-exchange membrane (e.g., Nafion), chemically plated

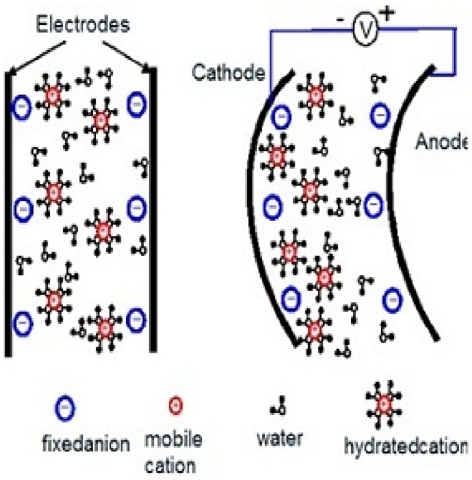

Figure 1.1: Illustration of IPMC sensing principle.

with a layer of noble metal (e.g., platinum) as electrodes on both surfaces [7, 14], as shown in Fig. 1.1. The traditional fabrication of IPMCs follows the process of impregnation, reduction, and ion-exchange [7]. Inside the polymer, anions are covalently fixed to polymer chains and balanced by cations that can move freely in the membrane. A mechanical deformation on an IPMC sensor breaks this charge balance, leading to the redistribution of the cations and accompanying solvent molecules inside the polymer, as well as the generation of a detectable sensing signal across the electrodes, which can be the open-circuit voltage or short-circuit current. Recent studies on characterization, modeling, and modeling of IPMC can be found in [15–22]. Recent applications of IPMC sensing capability span measurement of displacement [23], shear loading [24], curvature [25], structural health monitoring [18], and energy harvesting [26–29]. They are also bio-compatible and amenable to fabrication [7, 8, 10, 11, 30, 31], including 3D-printing [32, 33]. IPMC-based flow applications can be found in [34–38].

1.2 IPMC - based Applications

1.2.1 Ionic Polymer-Metal Composite Torsional Sensor

Reported IPMC sensors typically take the shape of beams because thin Nafion films are often used as raw material in the fabrication. Such IPMC sensors only respond to mechanical stimuli acting perpendicular to the beam plane. There have been reports on IPMC actuators or sensors of tubular [39], cylindrical [40], and columnar [41] shapes, which can bend in all directions. A tube-shaped IPMC transducer [2] with patterned outer electrodes was examined by Kim's group through finite element simulations. Its sensing response was experimentally investigated under bending excitation. The buckling effect of IPMC pipes was analyzed by Shen *et al.* [42]. Our group previously presented a thin-wall tubular IPMC sensor fabricated with Nafion tubing [43]. The sensor had one common inner electrode and four patterned outer electrodes, and its sensing response under tip-bending excitation was captured with a physics-based model [44]. As discussed above, IPMC sensors, regardless of their shapes, have been mostly studied under bending stimuli. We first reported the effect of torsion sensing for a tubular IPMC device and proposed a preliminary model for describing the sensing behavior in [45], where the charge densities at the inner and outer boundaries were assumed to be proportional to the difference of shear stresses at the two boundaries. While that model showed some agreement in magnitude frequency response with empirical measurement, the match in phase response was less than satisfactory. In particular, the model's phase response shows appreciable positive offset (error) from the empirical data when the frequency is above 4 Hz. Furthermore, since the charge density depends on the densities of both anions and cations, and the (mobile) cation density itself is a state variable that evolves with dynamics, assuming a prescribed charge density at the boundary is unnatural. In this work, we present an alternative, physics-based modeling approach for the torsional sensing response of an IPMC tube. Compared with [45], this approach not only adopts a more natural assumption, which prescribes the anion concentration in terms of the local shear strain state induced only by the torsion, but also is supported by extensive experimental results that involve transient responses.

In this work the Poisson-Nernst-Planck (PNP) model is adopted to describe the fundamental physics within the IPMC. In particular, the Nernst-Planck equation is used to describe the ionic current inside the polymer, due to cation diffusion, electric field-induced migration, and convection. Poisson's equation is used to describe the electric potential, which affects the cation migration flux. The external torsional stimulus is coupled to the PNP model through the cation convective flux term, where the cation velocity is affected by the solvent pressure, which is related to the polymer pressure caused by the applied mechanical stimulus, as adopted in [2]. A key innovation of the current work is that, we further assume that the anion concentration is perturbed by the local shear strain states induced by the torsion. This is inspired by the assumption used in [2], which relates the *volumetric* strain caused by the bending stimulus to the anion concentration. Based on the proposed model, time-dependent 3D finite element simulation is conducted for a tubular IPMC sensor under torsional excitation. Experiments are further conducted to compare the sensor response under torsional load with the simulation results, where a novel artificial neural network-based method is used to estimate key parameters of the physical model.

1.2.2 A Bio-inspired Artificial Lateral Line System

The lateral line system is a flow-sensing organ found in fishes and amphibians. The lateral line is flow-sensing involved in various biological behaviors, such as schooling [46], predator detection, prey capture [1], and obstacle avoidance [47]. The lateral line system is comprised of arrays of

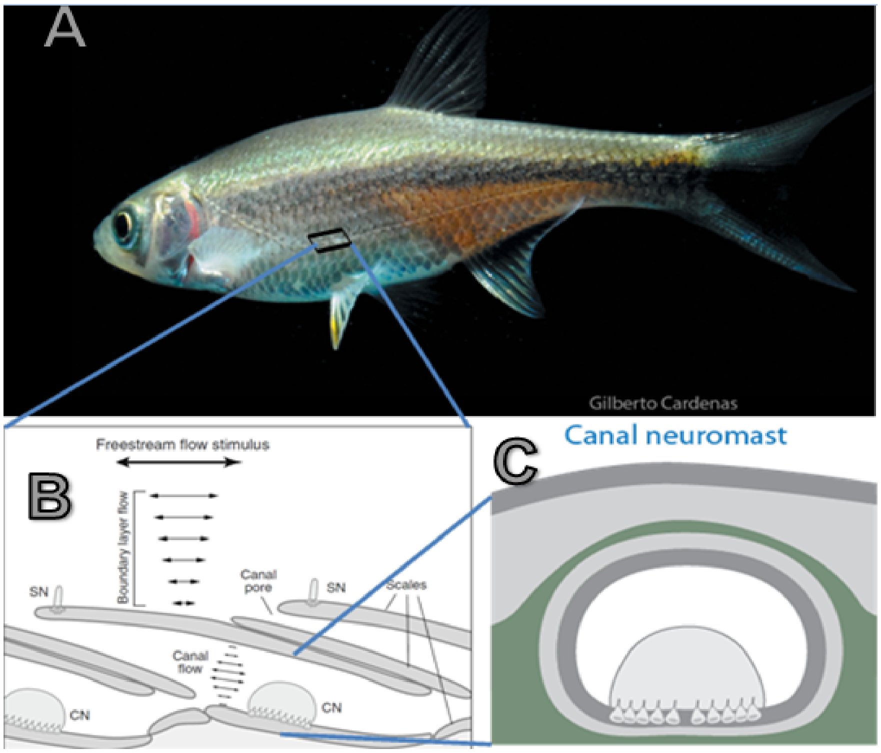

Figure 1.2: Distribution of a lateral line system [1], (a) A fish with lateral line systems; (b) The lateral line system with the superficial and canal neuromasts; (c) Canal neuromasts (CN).

flow sensors, which are mechanoreceptive units called neuromasts. A neuromast consists of a bundle of sensory hair cells enveloped in a gelatinous cupula [48]. There are two types of neuromasts, superficial neuromasts and canal neuromasts, as shown in Fig. 1.2. The superficial neuromasts extend from the skin and are directly exposed to the flow, where they tend to respond to the local flow velocity [49]. The canal neuromasts are found in canals recessed in the skin below the scales of fish [50] and they tend to react to the local pressure gradients, as illustrated in Fig. 1.2 (c). The response of the neuromasts in response to the interaction with the flow motion, in the form of action potentials, is transmitted to the central nervous system for further information processing [51].

The lateral line system of fishes has inspired a numerous number of efforts in designing and developing an engineering equivalent of similar sensing modality to facilitate the navigation, coordination, control of underwater robots and vehicles [52], object tracking [53], and dipole source characterization [37]. Such an artificial lateral line system offers the potential to introduce a novel and noiseless flow sensing modality complementary to traditional underwater vision sensors and sonars. Several research groups have reported hair cell-inspired flow sensors that to varying degrees have been motivated by fish neuromasts, exploiting micro-fabrication techniques [54, 55], optical transduction [56], and novel sensing materials such as ionic polymer-metal composites (IPMC) [30, 38, 41, 57]. While the majority of these sensors emulate the superficial neuromasts, some efforts have focused on canal-type lateral lines [58–60].

Modeling of the lateral line system plays a key role in understanding the dynamic behavior of the neuromasts and optimizing the design of artificial lateral lines. Much of the modeling literature focuses on the computation of flow fields around the fish body [61–64]. On the other hand, analytical or semi-analytical approaches have been employed in understanding the dynamics of superficial neuromasts [65] and canal neuromasts [66, 67] in response to flow stimuli.

In this work IPMC sensors are exploited to create artificial lateral line sensors, where both superficial and canal-type artificial neuromasts are investigated. Additional bio-inspired sensors are proposed, designed, modeled, and experimentally characterized. A more detailed account of the contributions follow.

1.2.2.1 Superficial lateral line system

Modeling of the lateral line system plays a crucial role in understanding the dynamic behavior of the superficial neuromast and then optimizing a lateral line device. McHenry et al. in [65] modeled the boundary layer created by the flow field around the superficial neuromasts and its influences on the cupula sensitivity when the stiffness and the size of the cupula changes. Further more, Sharif

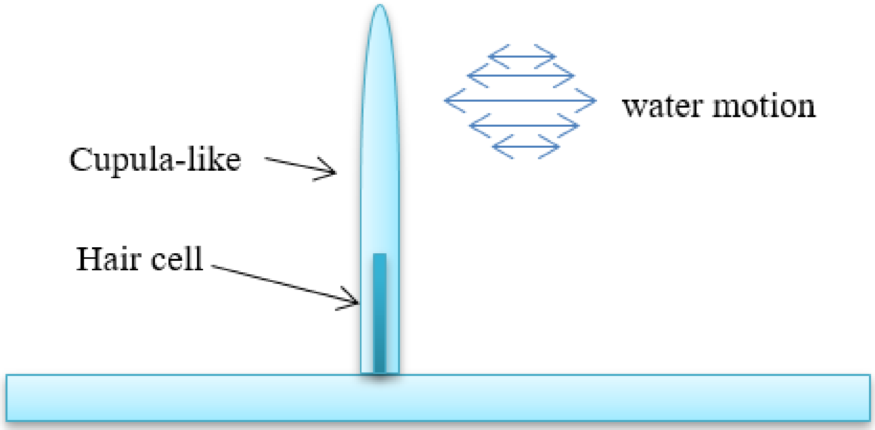

Figure 1.3: The schematic of a lateral line system, showing a single superficial neuromast and a hair cell sensor under oscillatory flow.

et al. in [68] reported that the sensitivity of the cupula is significantly influenced by the shape and stiffness of the cupula. In particular, the sensing performance of a superficial neuromast depends on mechanical properties of the cupula as well as the cupula morphology. Generally, the shape and size of the cupula affect both the fluid forces that may be generated by a stimulus and the structural resistance to these forces [65].

Fig. 1.3 shows the schematic of the lateral line system under consideration, where one superficial neuromast is considered. This configuration provides a reasonable approximation to the biological superficial neuromast and resembles the setup considered in [65], where the mechanical sensitivity of the neuromast under an oscillatory flow was analytically derived. A finite-element modeling approach is taken in this work for several reasons. First, as a higher-fidelity model, the finite-element model is instrumental in exploring the validity of the analytical model in [65]; due to its analytical but also physical nature, the latter, if validated, could serve as a convenient tool in the design of artificial lateral lines. Second, the proposed approach is expected to be useful when dealing with sensors larger than the scale of biological neuromasts, in which case some assumptions made in [65] start to fail. Third, the proposed approach enables natural integration with the physical model of IPMC, thus allowing the analysis of electrical output of the IPMC-based canal neuromast in response to flow stimuli.

1.2.2.2 Canal-type lateral line system

We model a canal-type lateral line system with an emphasis on the mechanical behavior of the hemisphere-like canal neuromast. We further consider that an IPMC beam, embedded in the cupula, serves as an artificial hair cell sensor that produces an electrical output in response to the motion of the cupula. The use of IPMC sensors for superficial lateral line systems has been reported in the past [30, 57, 64, 65], and this work, for the first time, investigates its use in canal-type lateral line systems. We validate the finite element model experimentally with a custom-made artificial canal-type lateral line. The canal is composed of a rigid cylindrical canal, which is filled with a viscous fluid. The prototype is comprised of one IPMC flow sensor, embedded in a cupula-like structure and placed at the middle of the canal, serving as an artificial hair cell sensor that produces an electrical output in response to the cupula motion. Experiments are conducted in an AC flow generated by a dipole source. The magnitudes of the IPMC short-circuit current output are extracted from the collected data to compare the sensor response under the dipole flow with the simulation results. A novel parameter identification approach from [69] is used to estimate key parameters of the finite element model. Fig. 1.4 shows the schematic of the system under consideration, where one canal-type neuromast is considered. This configuration provides a reasonable approximation to the biological canal neuromast and resembles the setup considered in [66], where the mechanical sensitivity of the neuromast under an oscillatory flow was analytically derived. A finite-element modeling approach is taken in this work for several reasons. First, as a higher-

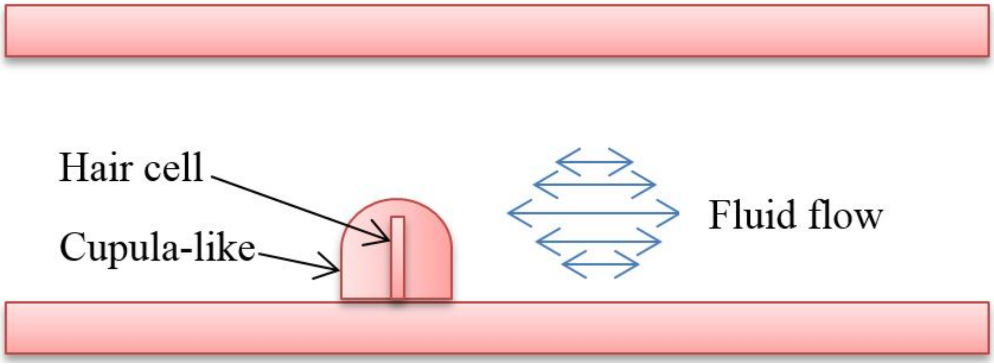

Figure 1.4: The schematic of a canal-type lateral line system schematic, showing a canal neuromast containing a hair cell-like sensor.

fidelity model, the finite-element model is instrumental in exploring the validity of the analytical model in [66]; due to its analytical but also physical nature, the latter, if validated, could serve as a convenient tool in the design of artificial lateral lines. Second, the proposed approach is expected to be useful when dealing with sensors larger than the scale of biological neuromasts, in which case some assumptions made in [66] start to fail. Third, the proposed approach enables natural integration with the physical model of IPMC, thus allowing the analysis of electrical output of the IPMC-based canal neuromast in response to flow stimuli.

1.2.3 A Pressure Gradient Sensor Inspired by the Canal Neuromasts of Fish

It is of interest to develop and implement an engineering counterpart of the biological lateral line system for underwater applications. The artificial lateral line system will provide a novel sensing modality for navigation and control of underwater robots and vehicles [34], and offers a cryptic complement to existing vision sensing modules such as sonar and camera. There have been a number of efforts in developing artificial lateral lines [52, 70]. Inspired by the fish neuromasts, some groups have reported hair cell-inspired flow sensors by exploiting micro-fabrication [54], optical transduction [56], and novel sensing materials such as ionic polymer-metal composites

(IPMCs) [30, 38, 41, 57, 71]. While the majority of these sensors emulate the superficial neuromasts, some works have focused on emulating canal-type neuromasts [60, 68]. The canal-type neuromasts-based sensing applications have also been explored, including, for example, determination of object position and vortex shedding frequency [56], source localization [72], and hydrodynamic detection [67, 73].

In this work, we present, to our best knowledge, the first pressure difference sensor inspired by the canal neuromasts of fish. Such a sensor could be used by underwater robots and vehicles for object detection, angle of attack measurement, and source localization. Unlike most of the aforementioned artificial lateral line systems on pressure sensing or object localization, where an array of sensors were used, the proposed sensor utilizes one sensing element embedded in a cupula-like structure, which is immersed in a canal (a "semicircular" channel) filled with a viscous fluid. The employed sensing element, which is an IPMC sensor, serves as an artificial hair cell sensor that produces an electrical output in response to the motion of the cupula. As an illustration, the pressure difference sensor is integrated within a fish-like body, and the two ends of the semicircular channel are "pores" like the ears of a fish. Unlike a fish canal that has open ends to the surface of the body, the two pores of the proposed sensor are covered with a thin latex membrane, to prevent the canal fluid from mixing with the ambient fluid.

Fig. 1.5 shows the schematic of the proposed sensor. Experiments are conducted in an AC flow generated by a dipole source, when the fish-like body is at different angles with respect to the dipole. The magnitudes of the IPMC short-circuit current output are extracted from the collected data. It is found that the sensor clearly responds to the pressure difference between the pores. To further understand the sensor behavior, time-dependent 3D finite-element simulation is conducted, where both fluid-structure interactions and IPMC physics are accommodated. With experimentally

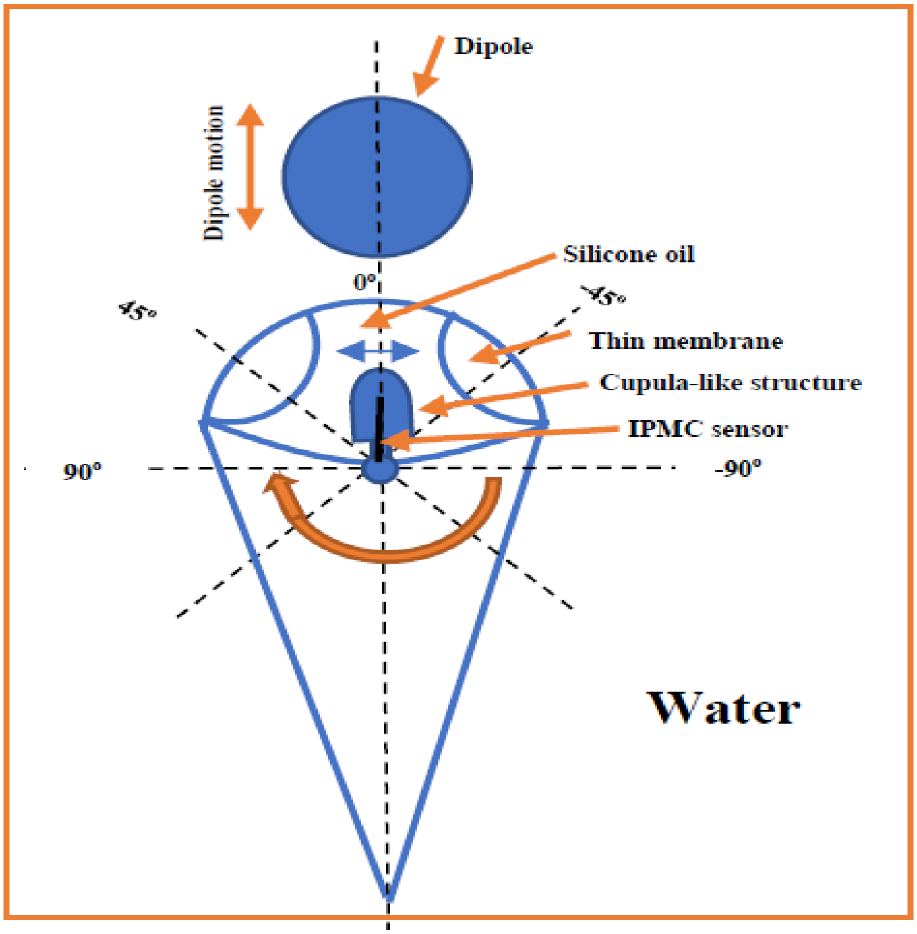

Figure 1.5: The schematic of the proposed sensor, showing a fish-like structure with two pores on the front and the artificial canal neuromast consisting of an IPMC sensor embedded in a cupula-like structure.

identified model parameters, the proposed model is able to capture the sensor behavior and shed light on pore membrane deflection and cupula displacement under an oscillatory flow of different angular displacements. To further demonstrate the use of the proposed sensor in potential robotic applications, feedback control experiments are conducted, to orient the fish-like body towards the dipole source based on the sensor output, starting from an arbitrary initial orientation. In particular, a sliding discrete Fourier transform (SDFT) algorithm [74, 75] is used

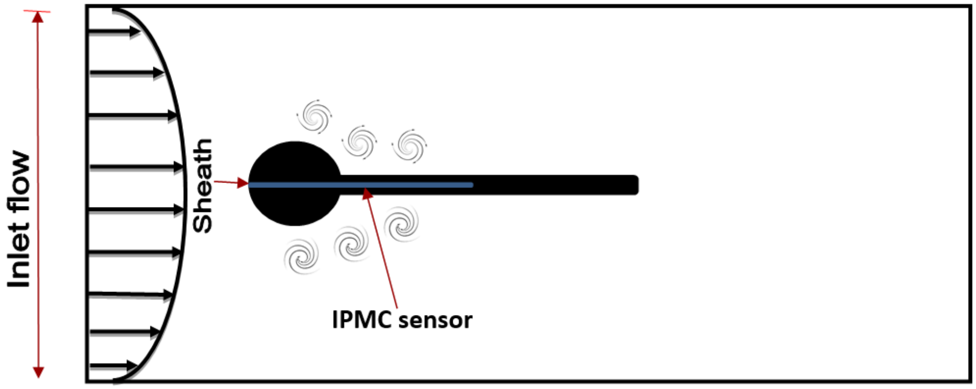

Figure 1.6: The schematic of the proposed IPMC flow sensing structure with self-generated vortices.

1.2.4 IPMC Flow Sensor Exploiting Self-Generated Vortices

IPMCs-based underwater sensing applications have also been widely investigated. More specifically, proposed application examples have included tracking of a moving dipole [76], flow sensor [34, 38, 71, 77], a vortex-shedding flowmeter [78], and a turbulent flow sensor [79].

In this work, a novel IPMC flow sensor structure is investigated. The proposed device exploits the self-generated von Krmn vortices to produce vibration of the sensor. Unlike the system described by Di Pasquale et al. [78], where an IPMC sensor was rigidly mounted on a circular flow pipe wall from one end and a cylindrical bluff body was attached on the free end of the IPMC to generate vortices, the proposed 3D-printed sensor structure consists of a rigid sphere, which is used to form the von Krmn vortices, and a soft cylindrical sheath that houses the IPMC flow sensor, as shown in Fig. 1.6. The response of the IPMC sensor due to vortex-induced sheath vibration is investigated empirically. In particular, experiments are conducted in a flow channel. The magnitudes and the frequencies of the free sheath vibration and those of the IPMC short-circuit current output are extracted from the collected data.

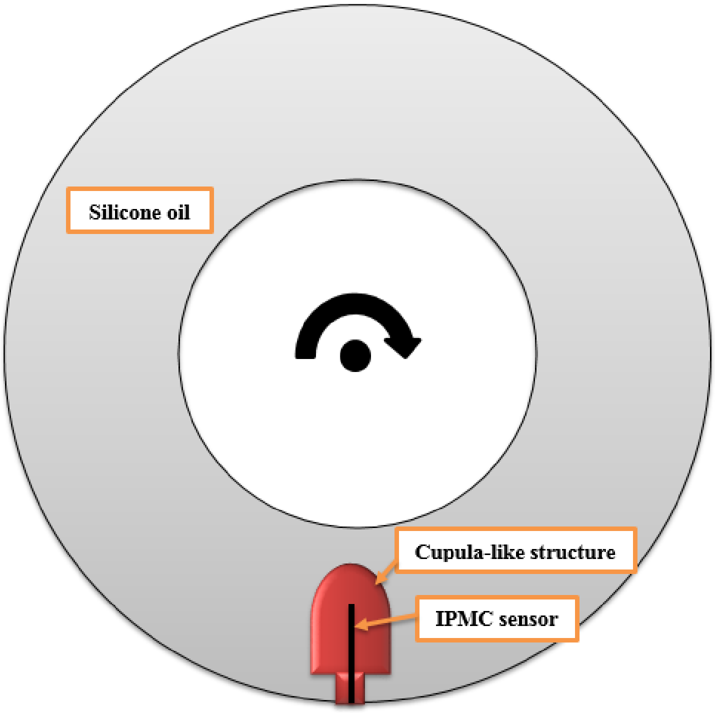

Figure 1.7: The schematic of the proposed sensor, showing a circular canal consisting of an IPMC sensor embedded in cupula-like structure.

1.2.5 Angular Acceleration Sensor Inspired by the Vestibular System

It is of interest to develop and implement an engineering counterpart of the biological vestibular system for robotic applications. An artificial vestibular system is of interest in robotics, for example, for stabilizing the gaze during the robotic head motion or the body movements [80–83]. Angelaki and Cullen [84] reported a vestibular system to used as an inertial sensor contributing to both spatial orientation and navigation. Developing an engineering equivalent of the biological semicircular canals to detect the angular acceleration is not reported yet.

In this work, a novel angular acceleration sensor based on artificial vestibular sensor is investigated. Unlike the biological counterpart of the vestibular system, which has three semicircular canals, the proposed 3D-printed sensor is composed of one rigid circular canal (a “torus” channel

), which is filled with a viscous fluid to emulate the biological equivalent. In this work, we reduce the three-dimensional sensing ability of the vestibular system to one-dimensional to gain more insight about the sensor performance. An IPMC flow sensor, embedded in a cupula and placed on the top wall of the canal, serves as an artificial hair cell sensor that produces an electrical output in response to the motion of the cupula.

Fig. 1.7 shows the schematic of the system under consideration, where one circular canal with one cupula is considered. Experiments are conducted with rotational stimuli at different accelerations. The IPMC short-circuit current output signals are collected as results of the the accelerations. To further understand the behavior, time-dependent 3D-finite element simulation is conducted for an artificial vestibular canal under rotational stimuli.

1.3 Overview of Contributions

The contributions of this research mainly lie in the physics-based modeling of IPMC sensors and the design and fabrication of several novel sensors based on IPMC. The details are as follows.

First, Poisson-Nernst-Planck (PNP) model is adopted to describe the fundamental physics within the tubular IPMC. The Nernst-Planck equation is used to describe the ionic current inside the polymer, due to cation diffusion, electric field-induced migration, and convection. Poisson's equation is used to describe the electric potential, which affects the cation migration flux. The external torsional stimulus is coupled to the PNP model through the cation convective flux term, where the cation velocity is affected by the solvent pressure, which is related to the polymer pressure caused by the applied mechanical stimulus. A key innovation of the current work is that, we further assume that the anion concentration is perturbed by the local shear strain states induced by the torsion.

Second, while the use of IPMC sensors in the superficial lateral line systems has been reported in the past, and this work, for the first time, investigates its use in canal-type lateral line systems. We have validate the finite element model experimentally with a custom-made artificial canal-type lateral line. Based on the latter finite-element model, the role of morphology of in sensitivity of artificial superficial lateral lines has investigated.

Third, a novel pressure gradient sensor inspired by the canal neuromasts of the fish is investigated based on 3D-printed ("U" channel) integrated with IPMC flow sensor. Unlike the fish canal that has open ends to the surface of the body, the two pores of the sensor are covered with thin latex membrane, to prevent the canal fluid from mixing with the ambient fluid.

Fourth, in this work, a novel IPMC flow sensor structure is investigated. The proposed device exploits the self-generated von Krmn vortices to produce vibration of the sensor. The proposed 3D-printed sensor structure consists of a rigid sphere, which is used to generate the von Krmn vortices, and a soft cylindrical sheath that houses the IPMC flow sensor. The response of the IPMC sensor due to vortex-induced sheath vibration is investigated empirically.

Fifth, a novel angular acceleration sensor inspired by the vestibular system is investigated using circular channel, which is filled with a viscous fluid to emulate the biological equivalent. An IPMC flow sensor, embedded in a cupula and placed on the top wall of the canal, serves as an artificial hair cell sensor that produces an electrical output in response to the motion of the cupula.

Chapter 2

Ionic Polymer-Metal Composite Torsional Sensor: Physics-based Modeling and Experimental Validation

We have developed a new physics-based model for a tubular IPMC sensor subjected to a torsional load. The model is built upon the Poisson-Nernst-Planck (PNP) equations for capturing the movement of cations. A key innovation of this work is the proposal of relating the shear strains to the local anion concentration. An experimental setup is created for applying twist at one end of the IPMC tube while keeping the other end fixed. Experiments involving stimuli of different magnitudes, loading orientations, and loading/unloading speeds have been conducted, and the proposed model was shown to be able to capture the trends observed experimentally.

2.1 Physics-based Modeling of the Tubular IPMC Sensor under Torsion

The transport of cations within the IPMC under applied loads is governed by the Nernst-Planck equation (NP) and the electrical potential is related to the charge density via Poisson's equation (P). These two equations, collectively known as the Poisson-Nernst-Planck (PNP) equations, along with appropriate coupling relating the mechanical stimulus to the charge density, provide a physical model for the IPMC sensor. Much of our model development and finite element modeling implementation follows the approach in [2] for the case of an omnidirectional *bending* sensor; however, there is a key difference in terms of how the external mechanical stimulus (torsion versus bending) is incorporated into the model.

2.1.1 PNP Model

For an IPMC sensor subjected to an external mechanical load, the induced ion movement leads to the redistribution of the charge density. The transport of cations is governed by the Nernst-Planck equation [40]. The flux vector J of cations consists of terms from diffusion, electromigration, and convection:

$$J = \underbrace{-D\nabla C^{+}}_{Diffusion} - \underbrace{zD\frac{1}{RT}FC^{+}\nabla\phi}_{Electromigration} - \underbrace{D\frac{1}{RT}C^{+}\Delta V\nabla P}_{Convection}, \tag{2.1}$$

where C^{+} is the cation concentration, z is the charge number of the cation, D is the diffusion coefficient, R is the gas constant, T is the absolute temperature, F denotes Faraday's constant, ϕ is the electric potential, ΔV is the molar volumetric change, which represents how much the polymer volume swells after taking water, and $\bigtriangledown P$ is the solvent pressure gradient. As treated in [2], the solvent pressure gradient is considered to be balanced by the gradient of the polymer pressure, $\bigtriangledown p$,

$$\bigtriangledown P = -\bigtriangledown p, \tag{2.2}$$

where p is the average normal stress of the polymer, resulting from solid mechanics calculation subject to the external load.

From the continuity equation

$$\frac{\partial C^+}{\partial t} = - \bigtriangledown \cdot J, \tag{2.3}$$

where "$\bigtriangledown\cdot$" denotes the divergence, one gets the NP equation:

$$\frac{\partial C^+}{\partial t} + \nabla \cdot (-D\nabla C^+ - z\frac{D}{RT}FC^+\nabla\phi - \frac{D}{RT}C^+\Delta V\nabla P) = 0. \tag{2.4}$$

The electric potential inside the polymer is related to the charge density ρ

$$\nabla^2\phi = -\frac{\rho}{\kappa_e}, \tag{2.5}$$

where "$\bigtriangledown^2$" denotes the Laplace operator, and κ_e is the effective dielectric constant of the polymer. The charge density is related to the ionic concentrations as follows:

$$\rho = F(C^+ - C^-) \tag{2.6}$$

where C^- is the local anion concentration, which is considered to be related to the local shape change under the applied torsional excitation, as discussed next.

2.1.2 Mechano-electrical Coupling

The anion concentration C^- can be related to the local deformation induced by the mechanical stimulus. This was first done in [2], where the authors relate C^- to the local volume change (approximated by the divergence of local displacement $\bigtriangledown \cdot u$) under a bending stimulus,

$$C^{-} = C_0(1 - \bigtriangledown \cdot u), \tag{2.7}$$

where C_0 represents the nominal anion concentration in the absence of deformation, and $u = (u_1, u_2, u_3)^T$ represents the displacement along x, y, and z directions, respectively. For a tube under pure torsion, $\bigtriangledown \cdot u = 0$, thus there would be no change in C^{-} under (2.7). Since the displacement under torsion is induced by shear, we propose instead

$$C^{-} = C_0(1 - \gamma) \tag{2.8}$$

where γ is the sum of the shear strains [85]:

$$\gamma = \varepsilon_{xy} + \varepsilon_{yz} + \varepsilon_{zx}. \tag{2.9}$$

2.2 Sensor Fabrication and Experimental Characterization

2.2.1 Fabrication of Tubular IPMC Sensors

The fabrication of tubular IPMC sensors generally follows the traditional impregnation, reduction, and ion-exchange process [44]. The Nafion tubing (TT -110, Perma Pure LLC) was used as the raw material, which had an inner diameter of 2.4 mm, outer diameter of 2.93 mm, and wall thickness of 265 μm. It was first rinsed with acetone then methanol to clean the tubing and to ensure that the surfaces of the sensor were free from impurities that might affect the fabrication process. Then the Nafion tubing was boiled in dilute hydrochloric acid (2 wt%) for 30 min to remove impurities, and then boiled in deionized (DI) water for another 30 min to remove the acid and swell the film. After these pre-treatment steps, the Nafion tubing was immersed in a platinum complex solution ($[Pt(NH_3)_4]Cl_2$) for more than 4 hours (usually 4–8 hours) to allow platinum ions to diffuse into the Nafion polymer completely through the ion-exchange process. After a rinse with DI water, the tubing was immersed in a water bath at 40°C for 30 min. After the temperature was raised to 60°C, a sodium borohydride solution (5wt% $NaBH_4$ aq) was added to the water bath as a reducing agent at a rate of 2 ml every 30 min. Once the platinum deposition was complete, those steps were repeated, from acid treatment to water-bath reduction, to deposit the platinum for the second time. The tubing was then boiled in DI water for one hour to release the internal stress. After that, it was put into a sodium chloride solution to exchange the residual platinum ions with sodium ions. The tubing was then cut into segments of desired lengths. Finally, a tubular IPMC sensor was formed by attaching two wire connectors to the inner and outer surfaces of the IPMC, respectively. Fig. 2.1 shows the pictures of a fabricated tubular IPMC sensor.

2.2.2 Experimental Setup

To characterize the sensor behavior under torsional excitation, we impose a pure torsional load at the tip of the tubular IPMC sensor. The short-circuit current between the inner and outer electrodes is taken as the sensor output. Fig. 2.2 (a) shows the major elements of the setup, including the torsion assembly that imposes a torsional load on the IPMC tubular sensor, the conditioning circuit [86] that filters and amplifies the sensing output, and the dSPACE system (RTI 1104) for data acquisition. Fig. 2.2 (b) shows the details of the torsion assembly. The tubular IPMC sensor is fixed with two drill chucks, one on each end. The chucks securely hold the sensor and ensure no

Figure 2.1: Fabricated tubular IPMC sensor.

slip when a torsional load is applied. The top end of the IPMC sensor is fixed on a 3D-printed plate, which is rigidly connected to a metal frame. The lower chuck is attached to a stepper motor (SparkFun Electronics - ROB 10846) which is used to generate a programmed angle of twist on the lower end of the IPMC. The stepper motor is controlled via a microcontroller (Arduino-uno).

2.2.3 Sensor Characterization

The responses of the tubular IPMC sensor are characterized with a sequence of torsional stimuli, to examine both its transient and steady-state behaviors. In particular, the angle of the stepper motor first ramps up from 0° to an angle θ in the clockwise direction, holds for 2 s, and then ramps back down to 0°; it then holds for 2 s, ramps up to θ in the counterclockwise direction, holds for 2 s, and finally ramps back down to 0°. Fig. 2.3 shows an example of the motor trajectory, where θ is 10°, and the speed of the motor when ramping up and down is 360°/s. We note that the chosen sequence of the motor movement allows us to examine a number of sensor behaviors,

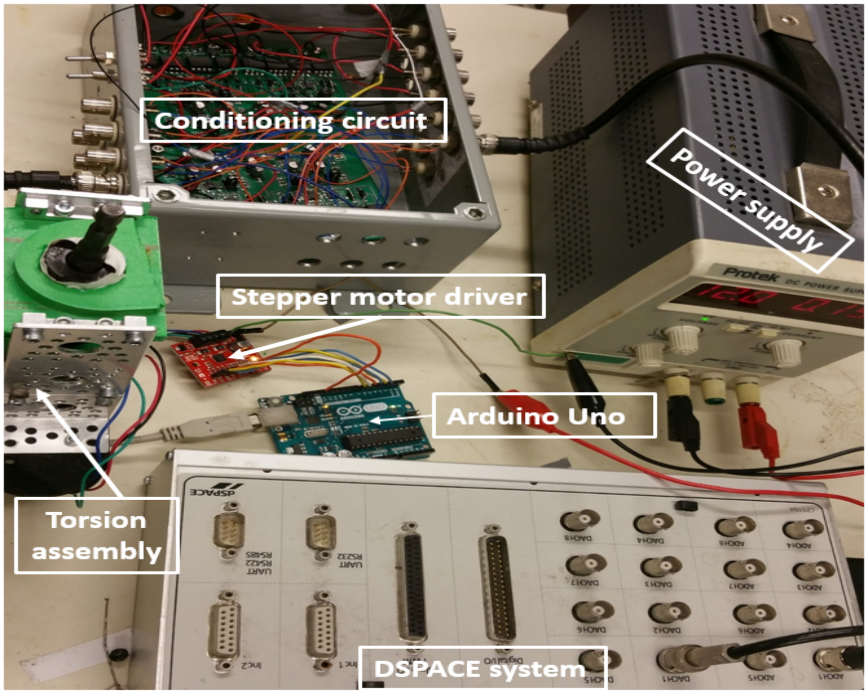

(a)

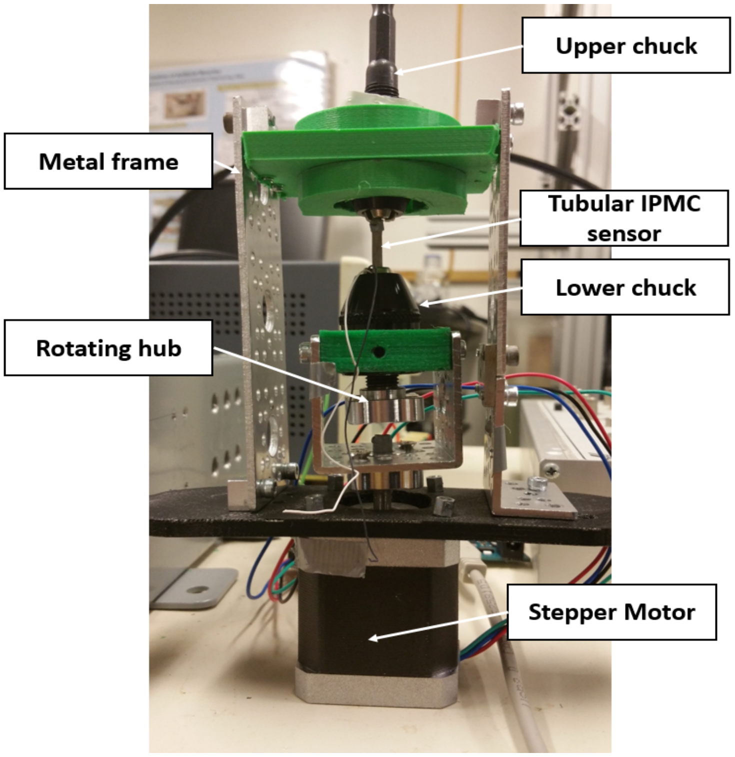

(b)

Figure 2.2: (a) Experimental setup involving the torsion assembly, conditioning circuit for the sensing output, and dSPACE system for data acquisition;(b) Details of the torsion assembly.

including both the dynamic behavior during transients and the steady state behavior (when the torsion angle is held constant for 2 s), the polarity of the sensing current during loading/unloading of the torsional stimulus, and the polarity of the sensing output when the sensor is twisted in one direction versus the other. Fig. 2.3 also shows the short-circuit current response from the sensor under the corresponding motor input. It can be seen that, when the torsion is loaded or unloaded, the sensor current produces a spike, which then approaches zero at the steady state. Furthermore, the polarities of the spikes during loading and unloading are opposite, and the polarity is independent of the loading orientation (clockwise or counterclockwise). These rich behaviors offer good tests for the proposed model. In addition, as will be discussed in Section 2.3, the model will be further tested by examining its ability to predict the sensor responses under different loading/unloading speeds and magnitudes.

2.3 Parameter Identification and Model Validation

2.3.1 Parameter Identification

Parameters for the model proposed in Section 2.1 are determined and used in model validation. The sensor dimensions, including the length, the inner and outer diameters, and the thickness of the platinum electrode layers, are obtained directly through measurement. In particular, the thickness of the platinum layers is computed using the measured thickness of the polymer tubing before fabrication and that of the fabricated IPMC tube. For the tubular IPMC sensor used in experiments, the dimensions are: length 15 mm, inner diameter 2.31 mm, outer diameter 3.02 mm. The physical constants in the model include the temperature (T), which is measured directly using a thermometer, density (ρ), which is obtained through measuring the sensor weight and volume, the Faraday

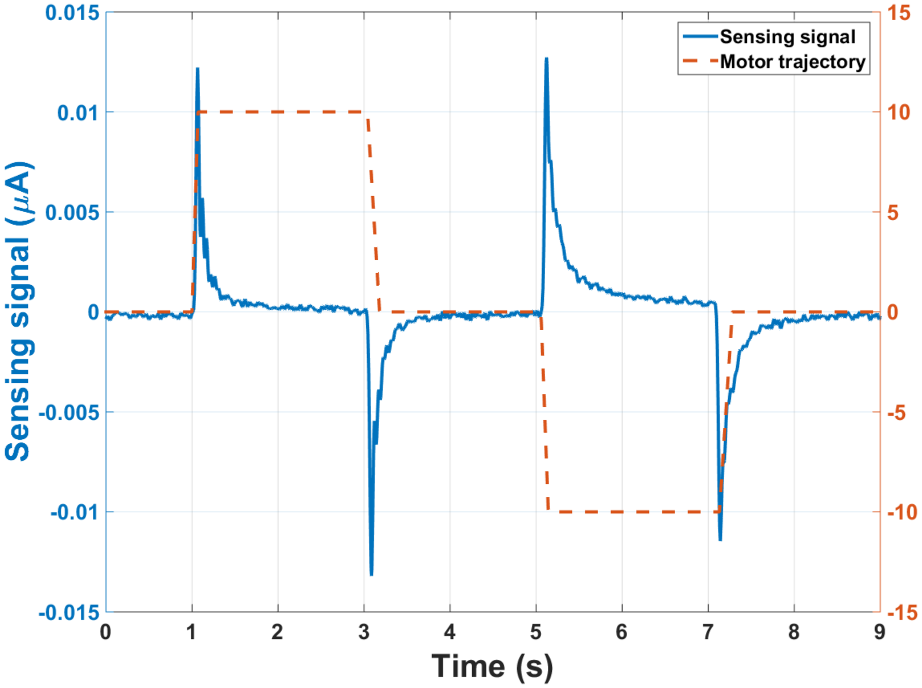

Figure 2.3: The applied sequence of motor inputs in loading/unloading the torsion, first in one direction and then in the other, and the corresponding sensing signal. Here the motor speed in ramping up/down is 360 °/s and the twist angle magnitude is 10°.

constant (F), and the gas constant (R). The value of anion concentration C_0 was taken from [44]. The electrical conductivity of the electrode (σ) was determined with the measured sensor surface resistance and the dimensions of the electrode. Table 2.1 lists the aforementioned parameters and constants.

The remaining parameters include the Young's modulus Y, diffusion coefficient D, and dielectric constant ε, all of which are obtained through an artificial neural network-based data fitting process. The Matlab toolbox ($nnstart$) is used to prepare a neural network with three inputs, which represent the parameters to be tuned, and one output, which represents the model fitting error. We have used a multilayer perceptron (MLP) network that contains one hidden layer with 10 nodes. The number of hidden layers and nodes are chosen according to [87]. Specifically, we use the imposed motor angle trajectory and the corresponding sensing signal in the first two seconds of the experiment shown in Fig. 2.3, for the purpose of parameter identification, and these same parameters will be used in other scenarios (different loading/unloading magnitudes and rates) of the experiments for model validation. Since the proposed model for the torsion sensor does not have an analytical input-output relationship expressed in terms of the parameters, finite element simulation is used to obtain the predicted sensing signal trajectory for the prescribed torsion stimulus, for any given set of parameters.

The simulation of tubular IPMC sensor model under torsional excitation, as described in Section 2.1, is implemented with COMSOL Multiphysics 5.1 finite element software packages. Four physics packages are used to implement the sensor model: solid mechanics, transport of diluted species, general-form PDE to generate the electrical potential within the nafion, and electrical current physics. The solid mechanics module is used to describe the linear elastic material under torsional excitation. The PNP model, which is used to describe the electrical potential and the cation concentration inside the Nafion during the deformation, is realized through the transport of diluted species physics and the general-form PDE physics. The implementation of the IPMC model under torsional stimuli is achieved with two separate computations. The deformation of the IPMC sensor is calculated first, followed by the execution of the PNP model, which uses the deformation data from the first study computation as input. A short-circuit current is collected by imposing the electrodes with zero potential and integrating the collected current density throughout the electrode surface.

We follow a tutorial provided by Matlab Inc. [88] to implement the neural network model, which offers a step-by-step instruction on how to use the command ($nnstart$). The neural network model requires a number of input-output data sets to start the training. In addition, the neural network needs to dedicate some of the input-output sets to test and validate the network after the training is completed. The average error between the predicted and measured sensing signals is treated as the output of the neural network for the corresponding input values (i.e., the parameters used in the simulation). A total of 120 sets of parameters, chosen within feasible ranges of these parameters, are used in conducting the simulation. Ninety sets of the obtained input-output data are used to train the neural network, 10 sets are used to test the neural network (cross validation), while 20 sets are used to validate the obtained neural network mode. An overall match of 98% is achieved between the trained neural network model and the experimental data. The 98% match is used as stopping criterion to stop the training process which is the highest matching we get in this process. The established neural network model is then used to serve as a fitness function to the optimization toolbox ($optimtool$) to find the optimal input vector that minimizes the output, which produces the optimal parameters (Y, D, ε) for the data fitting. The obtained values for these parameters are

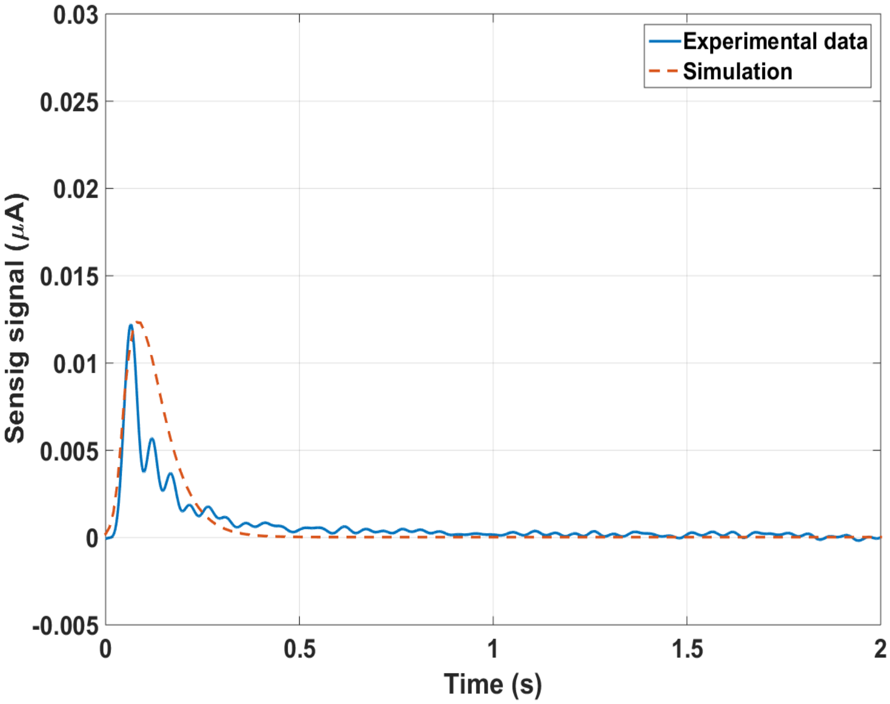

Figure 2.4: Testing results: a comparison between the experimental measurement and the simulation model after applying 10° twisting angle.

Table 2.1: Model Parameters of the Tubular IPMC Sensor.

F (C mol^{-1})	R (J mol^{-1}K^{-1})	T (K)	z	σ (S m^{-1})
96487	8.3143	290	1	7000.1
D (m^2 s^{-1})	C_0 (mol m^{-3})	ε (F m^{-1})	ρ (kg m^{-3})	E (Pa)
3.2×10^{-11}	1056	5×10^{-3}	2130	3.4×10^8

also listed in Table 2.1. Fig. 2.4 shows the comparison between measured signal and the model prediction based on the identified parameters. It can be seen that overall the model captures well the magnitude and transient behavior of the sensing response under the given stimulus.

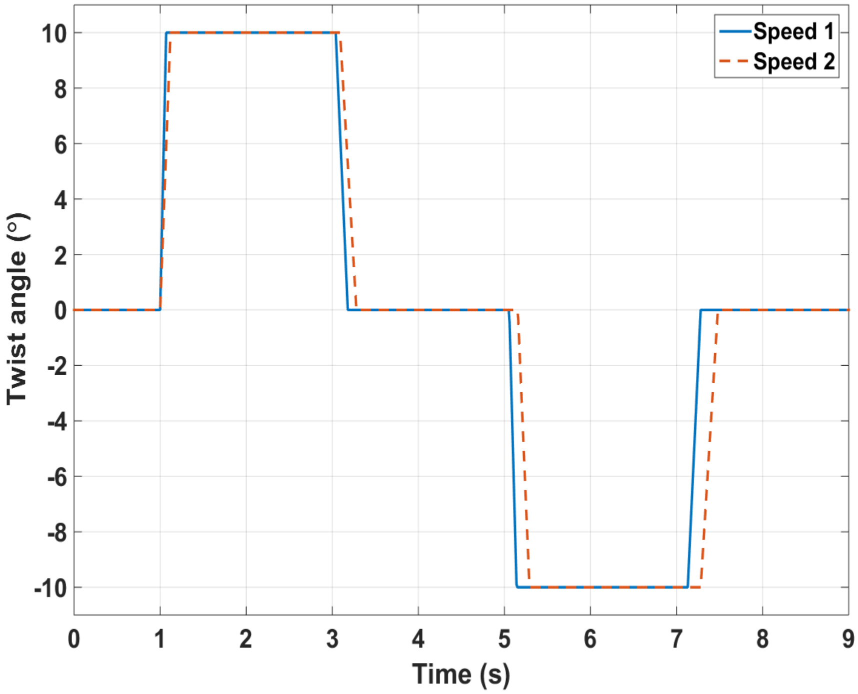

Figure 2.5: Input trajectory: two different stepper motor speeds to reach a specific angle

2.3.2 Model Validation

The identified parameters are then used in the simulation of the sensor responses under torsional stimuli of different magnitudes (10°, 15°, 20°) and loading/unloading rates. In particular, two loading/unloading speeds, $360^\circ/\mathrm{s}$ and $180^\circ/\mathrm{s}$, are adopted; Fig. 2.5 illustrates the profiles of the two speeds.

Fig. 2.6 (a)-(f) show the comparison between the measured sensor outputs and the model-predicted sensor outputs under different stimuli. Overall, all figures show good agreement between the measurement and model prediction. Given that three of the key model parameters are identified using only part of the data under a particular torsional stimulus, the reasonable match across all cases provides strong support for the validity of the model. Specifically, the model is able to capture the magnitude, transients, and polarity of the sensor response. For example, the polarity of

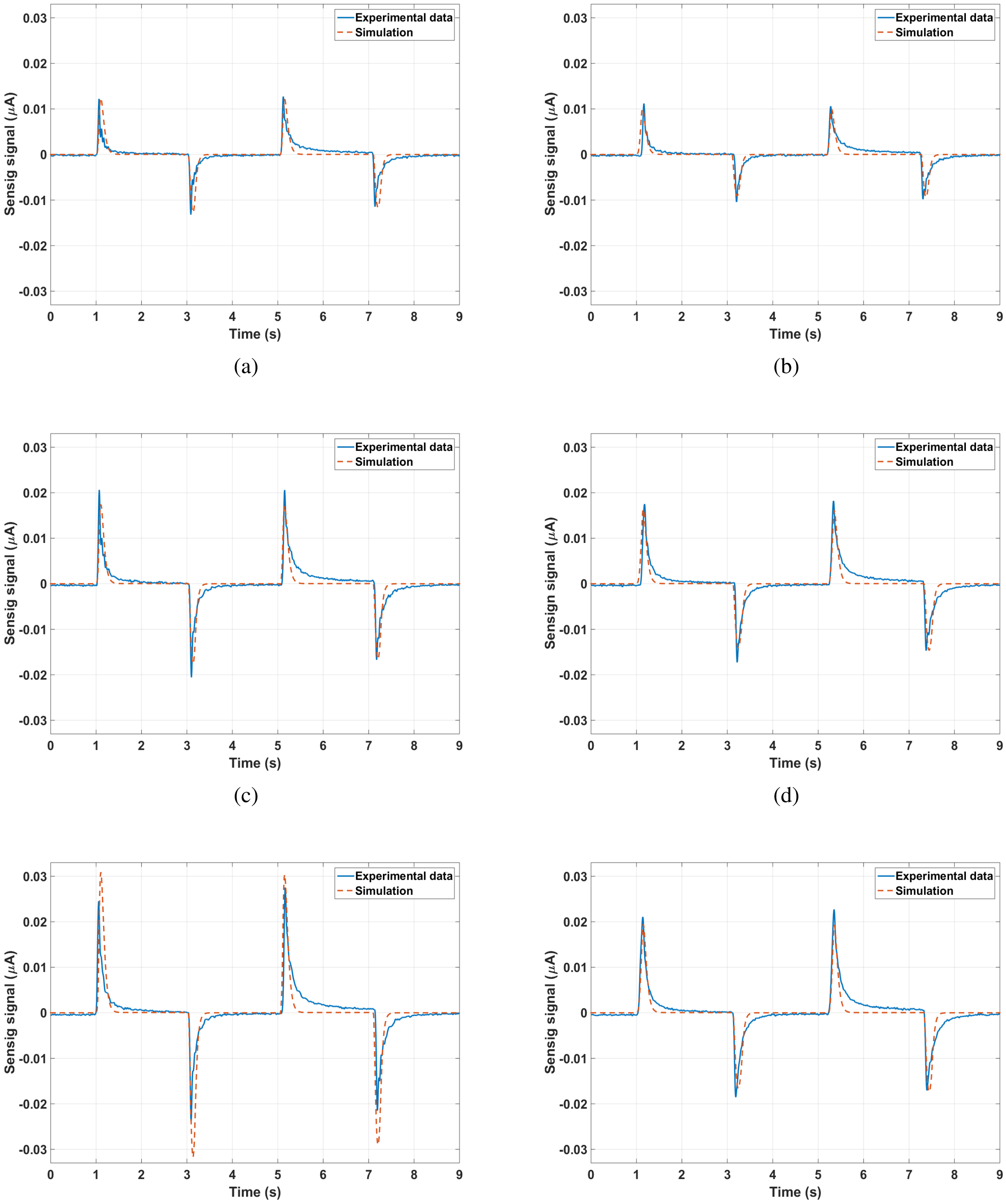

(a) (b) (c) (d) (e) (f)

Figure 2.6: Comparison between the experimental measurement and model prediction of the sensor response under different torsional stimuli: (a) Torsion magnitude 10°, speed 360°/s; (b) Torsion magnitude 10°, speed 180°/s; (c) Torsion magnitude 15°, speed 360°/s; (d) Torsion magnitude 15°, speed 180°/s; (e) Torsion magnitude 20°, speed 360°/s; (f) Torsion magnitude 20°, speed 180°/s.

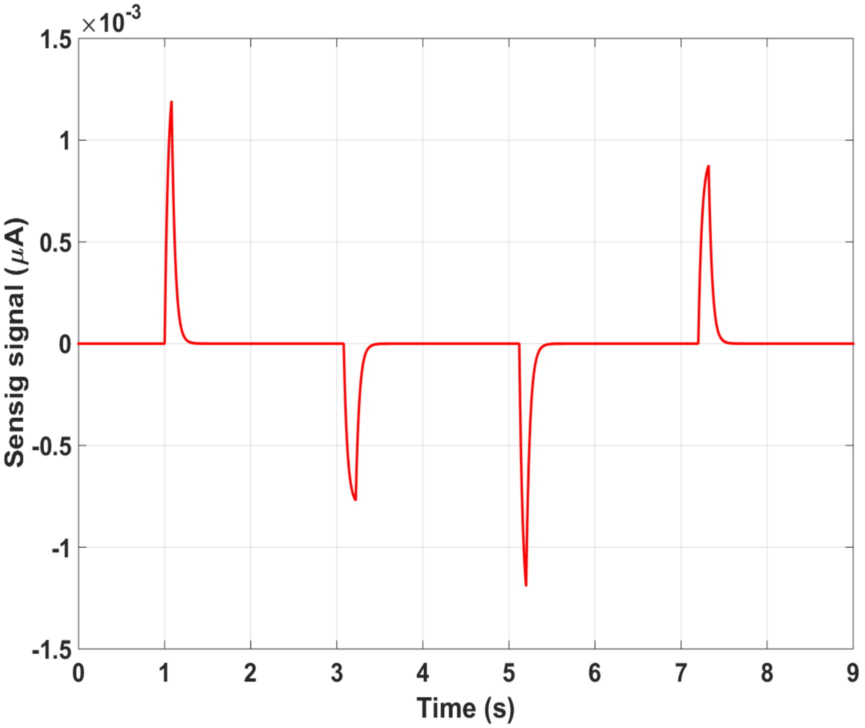

Figure 2.7: The simulated sensing response when the model in [2] is adopted for the stimulus of magnitude of 10° and rate of 360°/s.

the sensing signal is determined only by the loading or unloading trend of the stimulus, instead of the orientation of the torsional stimulus. The model also predicts correctly that the sensor response converges to zero at the steady state (for a constant torsion input). For the same loading rate, the results show that the sensing output magnitude increases with the stimulus magnitude (for example, see Fig. 2.6 (a), (c), and (e)). For the same stimulus magnitude, a higher loading/unloading rate results in higher sensing response (for example, see Fig. 2.6 (a) and (b)).

Despite the general good agreement, there are some modest discrepancies between the experimental data and the simulation results, which we attribute mainly to the imperfection in the fabrication of the tubular IPMC sensor and in the experimental setup. This can be seen, for example, in the experimental curve in Fig. 2.6 (c). The two positive signal spikes, ideally, should be identical; however, the transient speed of the second spike is appreciably slower than the first one, which can be seen from the increased offset between the simulated curve and the experimental curve for the second peak. A similar observation can be made for the two negative signal spikes. The latter could be caused by the rotation asymmetry between clockwise and counterclockwise directions. If one focuses on the first half of each subfigure, the agreement between the experimental data and model prediction is much more consistent.

Finally, to demonstrate the unique utility of the proposed model, we simulate the sensor response using the model in [2] for a torsional stimulus of magnitude 10° and rate $360^\circ/\mathrm{s}$. Recall that the key difference between the proposed model and the model in [2] is that the latter relates the volumetric strain to the local anion concentration. From Fig. 2.7, it can be seen that the model in [2], which was shown to work well for a bending sensor, cannot capture the qualitative behavior of the tubular IPMC sensor under torsion. In particular, it fails to correctly capture the polarity of the sensing response as observed in experiments. It also predicts asymmetric positive and negative responses, which are not observed in experiments.

Chapter 3

A Bio-inspired Artificial Superficial Lateral Line System

Inspired by the superficial neuromasts and the hair cells in the lateral line system of fish, we numerically and analytically explore the impact of the size, shape, and the stiffness of a neuromast on its sensitivity in detecting flow stimuli.

3.1 Modeling of the Superficial Neuromast

3.1.1 Analytical Model

We first review the analytical model for the mechanical sensitivity of the cupula structure developed by MacHenry et al. [65]. In particular, the model relates the morphology of the superficial neuromasts to the neuromast sensitivity over a range of stimulus frequencies. The model treats the cupula structure as a long cylinder with a specific radius and length and calculates the forces created on the cupula due to the flow. With a setup close to Fig. 1.3, this model is a solution to a fourth-order governing equation describing the forces acting on the cupula. These solutions provide predictions of cupular deflections as a function of the cupula heights. Unlike the latter model where they treat the cupula two joined parts of different stiffness, in this work, we treat the cupula-like structure as a homogeneous part. The inertial force is calculated as the product of acceleration

(-$\nu(z)\omega^2$) and the mass ($\rho\pi a^2 dz$) of a beam element

$$F_m = -\nu(z)\omega^2\rho_m\pi a^2 dz, \tag{3.1}$$

where ω is the angular frequency of oscillation (ω=2πf, where f is the stimulus frequency), F_m is the inertial force, ν is the cupular deflection, and ρ_m is the density of the cupular matrix. The boundary layer is created due to the flow acceleration and the flow velocity of the boundary layer is given by:

$$U(z) = U_\infty(1 - \exp(\frac{-z(1+i)}{\delta})), \tag{3.2}$$

where U_∞ is the stream flow velocity, and δ is the boundary layer thickness. The boundary layer thickness can be calculated by the following expression:

$$\delta = \sqrt{\frac{2\mu}{\rho_m\omega}}, \tag{3.3}$$

where μ is the dynamic viscosity of water and ρ_m is the density of water.

The deflection of the beam can be calculated as:

$$\nu(z) = -\frac{ib_w U_\infty}{\omega b_m}\left[1 - \frac{i\omega b_m\delta^4}{4EI + i\omega b_m\delta^4}\exp(\frac{-(1+i)z}{\delta})\right] + \sum_{j=0}^{3}(C_j\exp(jz\sqrt[4]{\frac{i\omega b_m}{EI}})), \tag{3.4}$$

where

b_m is the force coefficient for cupular material, and b_m can be calculated as:

b_m=-4$\pi\mu k$-iπ(ρ_m+ρ_w)$a^2\omega$ + $\frac{i\pi^2 k\mu}{L}$,

b_w is the for coefficient of the fluid, and b_w can be calculated as:

b_w=-4$\pi\mu k$-2i$\pi\rho_w a^2\omega$ + $\frac{i\pi^2 k\mu}{L}$,

k is the viscous drag coefficient,, and k can be calculated as: (k=-$\frac{L}{L^2+(0.25\pi)^2}$),

L is the hydrodynamic force coefficient,, and L can be calculated as:

L=γ+ln($\frac{a}{\sqrt{2}\delta}$), where γ is Euler's constant ($\gamma\approx$ 0.5772)

ρ_w is the density of water,

I is the second moment of area(I=$\frac{\pi}{4}a^4$),

E is Young's modulus, and a is the radius of the cupula.

The sensitivity of the neuromast is calculated as the following ratio:

$$S = \frac{v(h_h)}{U_\infty}, \tag{3.5}$$

where h_h is the height of interest that we choose to calculate the sensitivity.

3.2 Finite Element Model

3.2.1 Simulation Setup

In this section, we follow the steps in Section 4.2.1 for the simulation setup. The fluid-structure interaction (FSI) module of COMSOL Multiphysics is used to compute the cupula and the IPMC sensor displacement under a dipole stimulus. In this section, we assume that the cupula-inspired IPMC sensor is fixed in a finite water tank filled with water. The dipole source is placed within the tank to generate the periodic flow. To understand the scaling behavior of the canal neuromasts, two different dimensions are simulated, one at the μm scale and the other at the cm scale. The μm scale case is closer to the biological scale and is thus relevant to understanding the biological

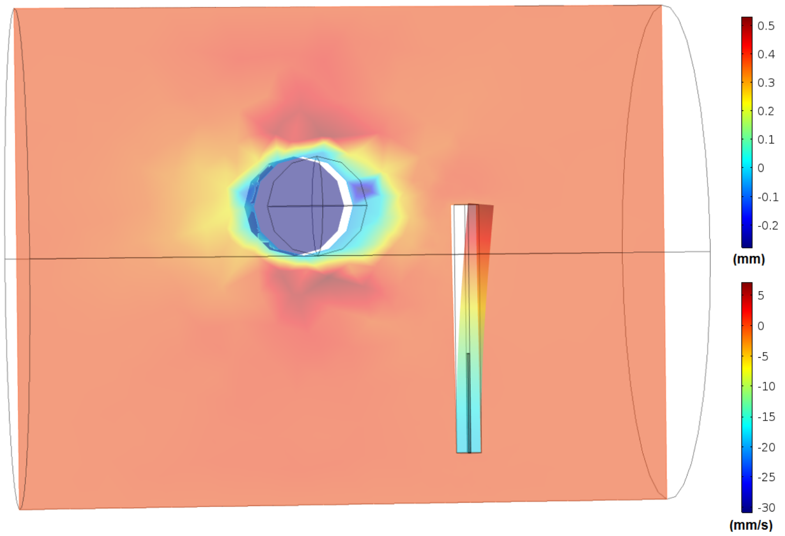

Figure 3.1: The finite-element modeling of a superficial neuromast in the presence of a dipole stimulus, where the cupula in the cylindrical shape. The top color bar represents deflection of the IPMC sensor beam while the lower color bar represents the flow velocity around the cupula.

neuromasts and offering meaningful comparison with the analytical modeling results. On the other hand, the cm scale reflects the dimensions of many engineered lateral line devices and is relevant to practical design of such systems.

The range of dipole frequency use for the μm scale case is 2 to 300 Hz, and that for the cm scale case is 2 to 24 Hz. These ranges are chosen so that the cupula in each case would produce sufficient movement and thus sensing signals. The amplitude of the vibration A is set to be much less than the radius of the sphere [66]. In particular, A is set to be 0.1 μm for the μm scale cases, and 2 mm for the cm scale cases in this work. Fig. 3.1 and Fig. 3.2 illustrate the simulated configuration for the superficial lateral line system, where the cupula on the right represents the cupula (with an IPMC sensor beam embedded) and the sphere on the left represents the dipole source. Appropriate boundary and initial conditions were used in the simulation. In particular, the water around the cupula is set to be at rest at time 0. The cupula is fully supported from the

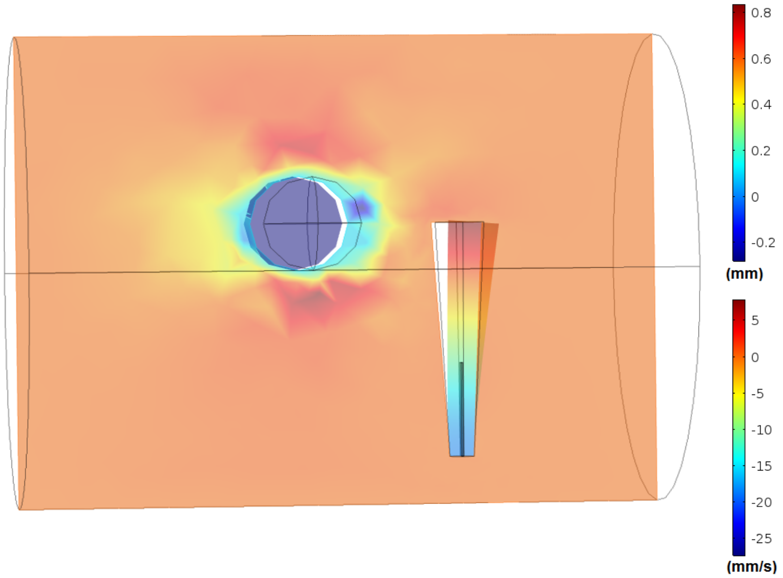

Figure 3.2: The finite-element modeling of a superficial neuromast in the presence of a dipole stimulus, where the cupula in the cone shape. The top color bar represents deflection of the IPMC sensor beam while the lower color bar represents the flow velocity around the cupula.

bottom, and so is the IPMC beam, which implies that their displacements at the bottom are zero. The cupula tip is located at the same center line of the dipole. Fig. 3.1 and Fig. 3.2 represent the flow field (mm/s) as well as the displacement of the structure during fluid movement (mm). These plots represent a slice from the three dimensional canal model. The simulation results in both the fluid flow profile and the displacement and deformation of the cupula (including the IPMC beam). Two different geometries of cupula structures are used for the cm scale, one is a cylindrical shape as in (Fig. 3.1) and the second one is a cone shape as in (Fig. 3.2). Two different aspect ratios are used in the cylindrical case, the first one with a radius of 0.25 cm and length 5 cm, the second one with a radius of 0.25cm and a length of 2.5 cm. The cone cupula also has two different aspect ratios, each base and top radius of 0.25 cm and 0.5 cm, respectively and the with two different lengths (5 cm and 2.5 cm). The distance between the cupula and the dipole source is 2 cm. Similar setups are used for the μm scale simulation, except all dimensions are scaled down by 1000 times

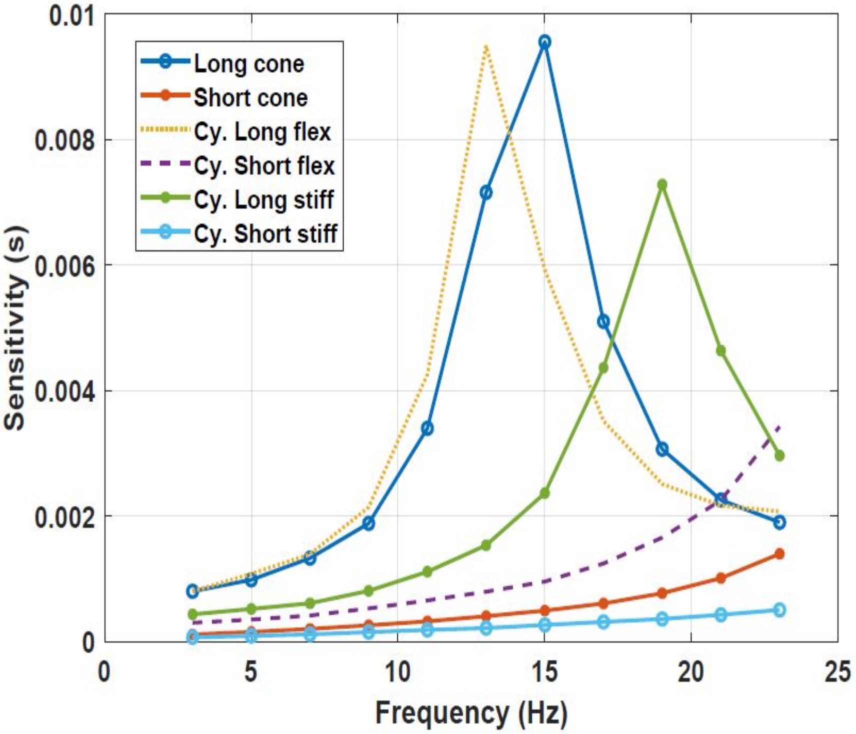

Figure 3.3: Displacement magnitude of the cupula structure with four different shapes as a function of the dipole frequency, where two Young's moduli were used 10 KPa (flex) and 0.2 MPa (stiff).

smaller and we do not consider cone shapes. The simulated water tank is a long cylinder closed at both ends and flat at the bottom with an open boundary from the top. Young's modulus directly influences the sensitivity of the structure, so several different values of Young's modulus are used for the cupula structure in the investigation.

3.3 Comparison between Numerical and Analytical Results

As we discussed in 4.2.2, the periodic fluid movement within the water tank produces a periodic movement of the cupula structure at the same frequency at the steady state. Using fast Fourier transform (FFT), we can extract the amplitudes of the movement corresponding to different frequencies, as illustrated in Fig. 3.3.

Fig. 3.3 shows the amplitude of the cupula displacement as a function of the dipole stimulus frequency, where four different sizes of cupula (as explained in Section 3.2.1) and two values of Young's modulus 10 KPa (flexible) and 0.2 MPa (stiff) are used. In the range of 2 to 24 Hz, it can be seen that the displacement magnitude of the cupula increases first with the frequency of the dipole until it reaches a maximum at a specific frequency then drops for the longer cupula (length = 5 cm). For the cupula with length of 2.5 cm, the amplitude keeps increasing during that range. These peak frequencies are considered to be related to the resonant frequencies of the cupula structure in the fluid.

Fig. 3.4 shows the comparison of the simulation results for the two cupula structures at the cm scale, where the Young's moduli are set to be 0.2 MPa and 10 KPa for both cupula structures. From the figure, the longer cupula structure has a lower peak frequency, as expected. Also, from the figure, the softer cupula structure has lower peak frequency. These results are consistent with one's expectations, as the resonant frequency of a structure increases with its stiffness and decreases with its mass (size).

We next present the results on the μm scale cases. As we discussed in Section 4.2.2, the transition from the cm scale to the μm scale is vital because it will reveal the behavior of the cupula in biological scales and make connections with the practical engineered lateral lines with in the cm scale. A cupula structure with radius of 0.25 μm and length of 5 μm is simulated in a water tank with length of 5 μm. Three different values of Young's modulus, 80 Pa, 250 Pa, and 500 Pa, are used. Fig. 3.5 shows the sensitivity amplitudes of the cupula structures, where one can observe that the there is no peak frequency in the cupula response; instead, the cupula shows the behavior of a low-pass filter. These results again demonstrate the important roles that dimensions and stiffness play in the sensor's sensitivity and appropriate operating frequency range. Overall the

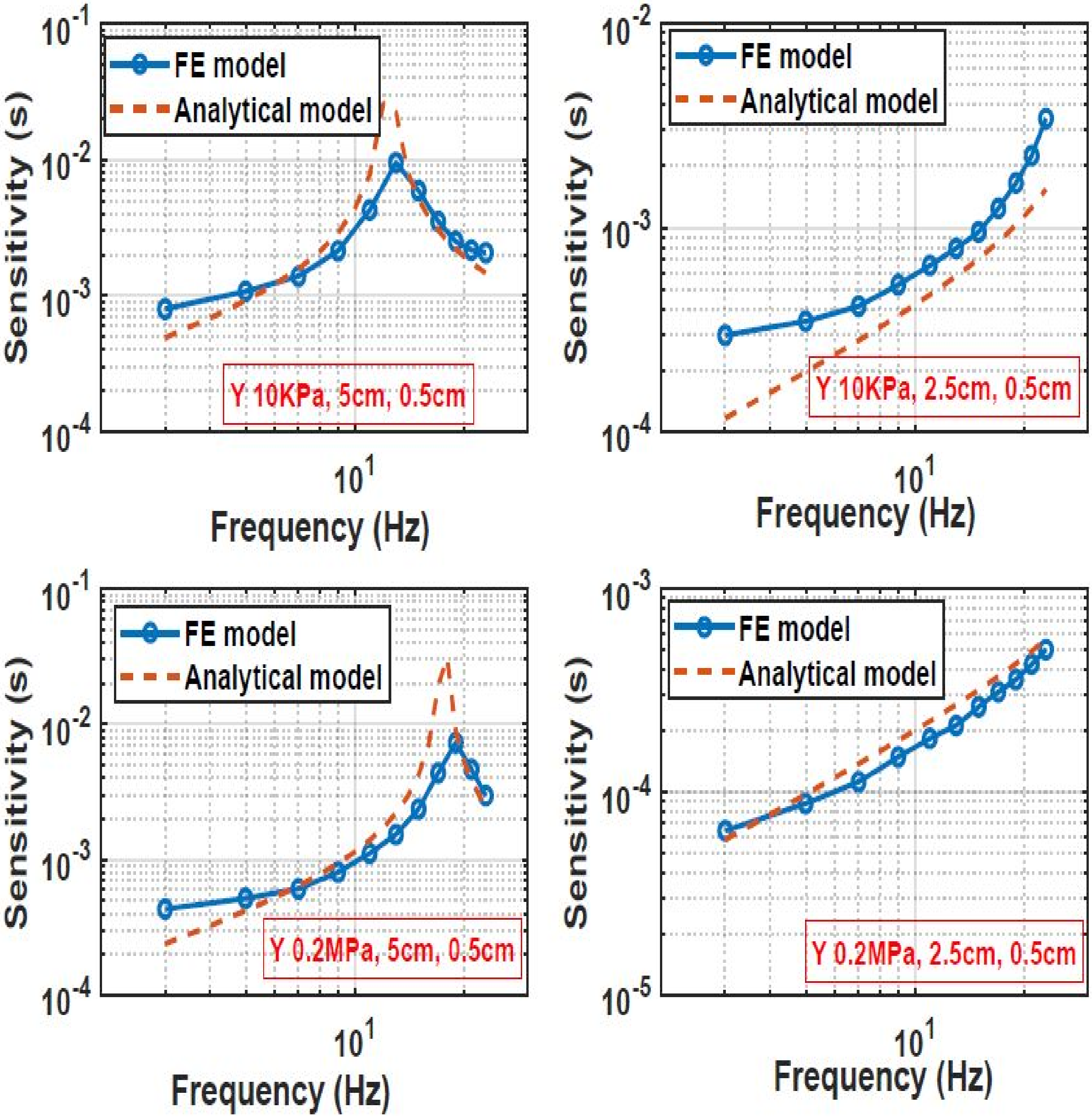

Figure 3.4: Comparison between the FE model and the analytical model cm-scale cupula structures.

frequency behavior of the modeled cupula shows good agreement with the behavior of biological cupula in [65].

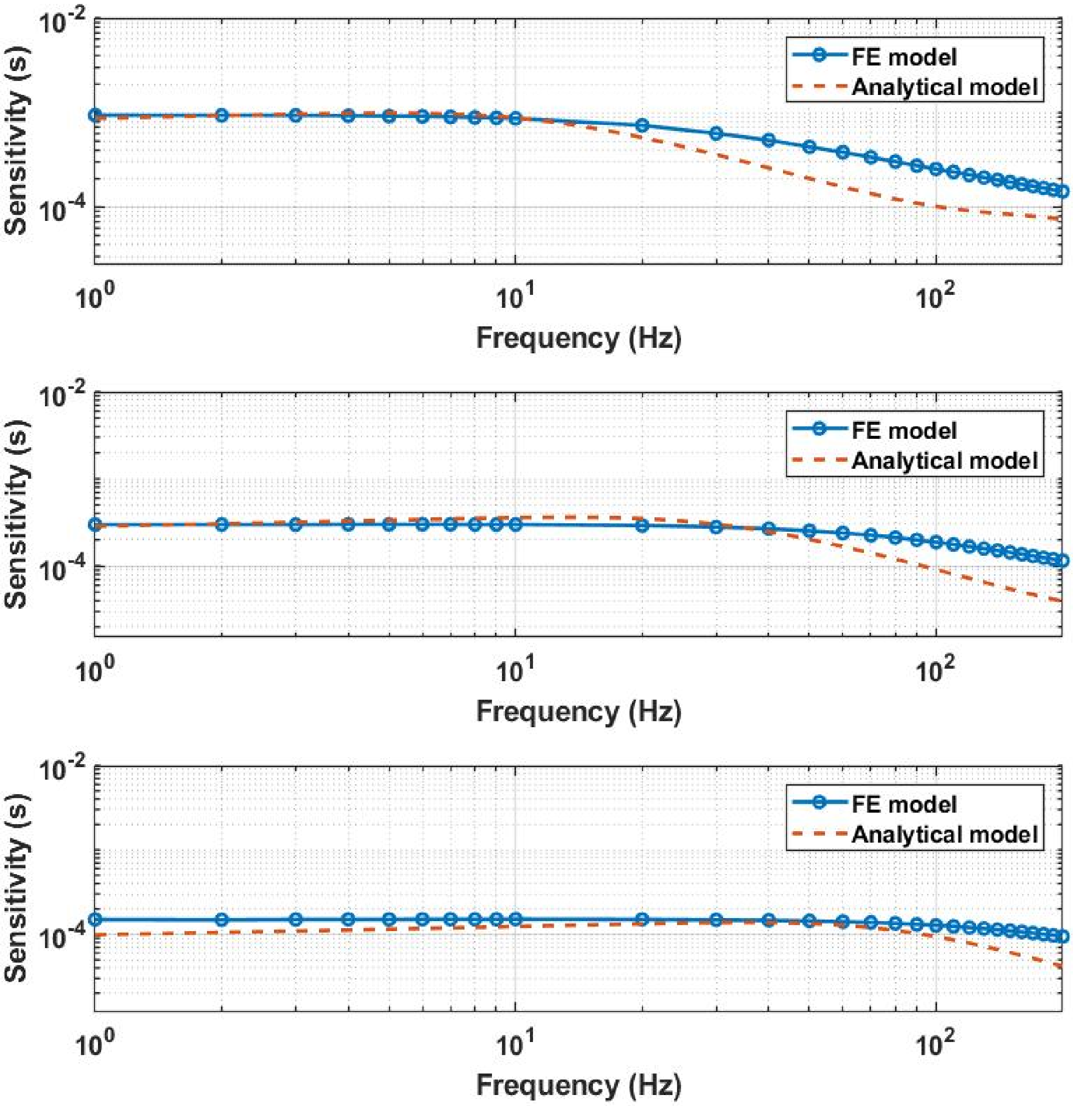

Figure 3.5: Comparison between the FE model and the analytical model μm-scale cupula structures.

Chapter 4

A Bio-inspired Artificial Canal-type Lateral Line System

In this chapter, we investigate the modeling, fabrication and experimental validation of the artificial canal-type lateral line system. To emulate the biological counterpart, the canal is filled with a viscous fluid. The IPMC sensor physics is coupled to the Fluid-Structure Interaction (FSI) module for the cupula, allowing the computation of the sensor output in the presence of a dipole flow. The fabrication process of the IPMC flow sensor and cupula-like structure are described in detail. Experimental testing in a dipole flow is conducted to explore the sensor performance. Simulation is conducted to examine the effects of cupula size and stiffness on its displacement under a dipole stimulus. In particular, the computation results from the finite-element model are compared with those predicted by an analytical model to explore the valid regimes of the analytical model. Such comparisons yield useful insight as to when to use the analytical model for quick exploration of the design space, and when to resort to the finite element model for higher-fidelity predictions.

4.1 Modeling of the Canal-type Neuromast

4.1.1 Physics-based Modeling of the Canal Neuromast Under Oscillatory Flow

4.1.1.1 Fluid Structural Interaction (FSI)

The response of a canal neuromast, biological or engineered, is due to the deflection of the cupula structure in the presence of a flow stimulus. To capture the cupula displacement response, a three-dimensional fluid-structural interaction (FSI) module from COMSOL Multiphysics is considered. In particular, the model incorporates various material properties and dimensions, including the canal geometry, cupula shape and size, cupula stiffness, IPMC sensor beam geometry and size, and fluid density and viscosity. The FSI model uses the incompressible Navier-Stokes equation to describe the fluid flow and the Hooke's law to capture the linear elastic material behavior. As detailed in the next subsection, Poison-Nernst-Plank (PNP) equations are used to model the IPMC sensor response under a mechanical stimulus, which is generated by the flow-induced capula movement.

4.1.1.2 Modeling of the IPMC Sensor Under Bending Excitation

The modeling of an IPMC sensor under bending excitation starts from the Nernst-Plank equation (*NP*) that governs the transport of cations within the IPMC sensor. The electrical potential generated inside the IPMC is governed by the Poisson's equation (*P*). Collectively, these equations form the PNP system, which, along with suitable coupling with the mechanical stimulus to the charge density, provides a physical model for the IPMC sensor. The flux vector J of cations consists of contributions from diffusion, electromigration, and convection:

$$J = \underbrace{-D\nabla C^{+}}_{Diffusion} - \underbrace{zD\frac{1}{RT}FC^{+}\nabla\phi}_{Electromigration} - \underbrace{D\frac{1}{RT}C^{+}\Delta V\nabla P}_{Convection}, \tag{4.1}$$

where C^{+} is the cation concentration, z is the charge number of the cation, D is the diffusion coefficient, R is the gas constant, T is the absolute temperature, F denotes Faraday's constant, ϕ is the electric potential, ΔV is the molar volume, which represents how much the polymer volume swells after taking water, and P is the solvent pressure gradient. As treated in [40], the solvent pressure gradient is considered to be balanced by the gradient of the polymer pressure, $\bigtriangledown p$,

$$\bigtriangledown P = -\bigtriangledown p, \tag{4.2}$$

where $\bigtriangledown P$ is the average normal stress of the polymer, resulting from solid mechanics calculation subject to the external load.

From the continuity equation

$$\frac{\partial C^{+}}{\partial t} = -\bigtriangledown \cdot J, \tag{4.3}$$

where "$\bigtriangledown\cdot$" denotes the divergence, one gets the NP equation:

$$\frac{\partial C^{+}}{\partial t} + \nabla\cdot(-D\nabla C^{+} - z\frac{D}{RT}FC^{+}\nabla\phi - \frac{D}{RT}C^{+}\Delta V\nabla P) = 0. \tag{4.4}$$

The electric potential inside the polymer is related to the charge density ρ

$$\nabla^{2}\phi = -\frac{\rho}{\kappa_e}, \tag{4.5}$$

where "$\bigtriangledown^2$" denotes the Laplace operator, and κ_e is the effective dielectric constant of the polymer. The charge density is related to the ionic concentrations as follows:

$$\rho = F(C^+ - C^-) \tag{4.6}$$

where C^- is the local anion concentration, which is considered to be related to the local shape change under the applied bending excitation, as discussed next.

The anion concentration C^- can be related to the local deformation induced by the mechanical stimulus. This was first done in [40], where the authors relate C^- to the local volume change approximated by the divergence of local displacement $\bigtriangledown \cdot u$,

$$C^- = C_0(1 - \bigtriangledown \cdot u), \tag{4.7}$$

where C_0 represents the nominal anion concentration in the absence of deformation, $u = (u_x, u_y, u_z)^T$ represents the displacement along x, y, and z directions, respectively, and $\bigtriangledown \cdot u$ is the sum of the normal strains [89]:

$$\bigtriangledown \cdot u = \varepsilon_{xx} + \varepsilon_{yy} + \varepsilon_{zz}. \tag{4.8}$$

We solved equations (1)-(8) are simultaneously in COMSOL Multiphysics 5.2a finite element software to implement the PNP model and the deformation effects. Four module packages are used to simulate the sensor model: fluid-structural interaction (FSI), transport of diluted species, general-form PDE to generate the electrical potential within the nafion, and electrical current physics. The solid mechanics part in the FSI module is used to describe the linear elastic materials under periodic flow excitation. The PNP model, which is used to describe the electrical potential and the cation concentration inside the Nafion during the deformation, is realized through the transport of diluted species physics and the general-form PDE physics. The implementation of the IPMC model under consideration is achieved with two separate computations. The deformation of the IPMC sensor is calculated first, followed by the execution of the PNP model, which uses the deformation data from the first study computation as input. A short-circuit current is collected by imposing the electrodes with zero potential and integrating the collected current density throughout the electrode surface.

4.1.2 Analytical Modeling of Cupula Displacement

We review the analytical model for the mechanical sensitivity of the cupula structure under a dipole stimulus which was presented by Van Netten [66]. A dipole source is a vibrating sphere in the fluid, and it has been used extensively in the investigation of biological and artificial lateral lines [90] [37]. With a setup close to Fig. 1.4, the analytical model is a solution to the Navier-Stokes equation for an incompressible oscillatory flow, for a small amplitude of vibration A for the uniform flow field. Let the fluid displacement be, x = $A\sin(\omega t)$, where $A \ll a$ with a being the cupula radius, and ω is the angular frequency. The general form of the governing equation is as follows

$$\rho\frac{\partial v}{\partial t} + \nabla p - \mu\nabla^2 v = 0, \tag{4.9}$$

$$\nabla \cdot v = 0, \tag{4.10}$$

where ρ is the fluid density, p is the pressure, v is the fluid velocity, and μ is the dynamic viscosity of the fluid. The fluid force on the cupula is obtained by integrating the pressure and the shear stress in the direction of the movement of the sphere, which is in the horizontal direction. The fluid force, which is essential to the deformation of the cupula, is given by

$$F_{fluid} = -6\pi a\mu A\omega[(\frac{a}{\delta}+1)\cos(\omega t) - \frac{a}{\delta}(\frac{2a}{9\delta}+1)\sin(\omega t)] \tag{4.11}$$

where δ is the boundary layer thickness, $\omega = 2\pi f$, where f is the stimulus frequency.

To calculate the displacement of the cupula, the latter is modeled as a rigid hemisphere sliding over the sensory epithelium via an elastic coupling with a sliding stiffness S. Let $D(t) = D_0\exp(i\omega t)$ denote the displacement of the fluid inside the canal, and $X(t) = X_0\exp(i\omega t)$ be the resulting cupula displacement. It is shown in [66] that X_0 is given by

$$X_0 = \frac{i(\frac{f}{f_t}) + \frac{1}{2}\sqrt{2}(i-1)(\frac{f}{f_t})^{\frac{3}{2}} - \frac{1}{2}(\frac{f}{f_t})^2}{P_c + i(\frac{f}{f_t}) + \frac{1}{2}\sqrt{2}(i-1)(\frac{f}{f_t})^{\frac{3}{2}} - \frac{1}{3}(\frac{f}{f_t})^2} D_0, \tag{4.12}$$

where f is the stimulus frequency, $f_t = \frac{\mu}{2\pi\rho a^2}$, and $P_c = \frac{Sa\rho}{6\pi\mu^2}$.

Through the comparison with the finite-element model, we will explore the validity and limitations of this analytical model, which will offer insight into the choice of models for lateral line design and analysis.

4.2 Finite Element Model

4.2.1 Simulation Setup

The fluid-structure interaction (FSI) module of COMSOL 5.2 Multiphysics is used to compute the cupula displacement under a dipole stimulus. The canal is assumed to be filled with a fluid that has a viscosity five times of that of water, which is close to the viscosity of fluid within fish canals.

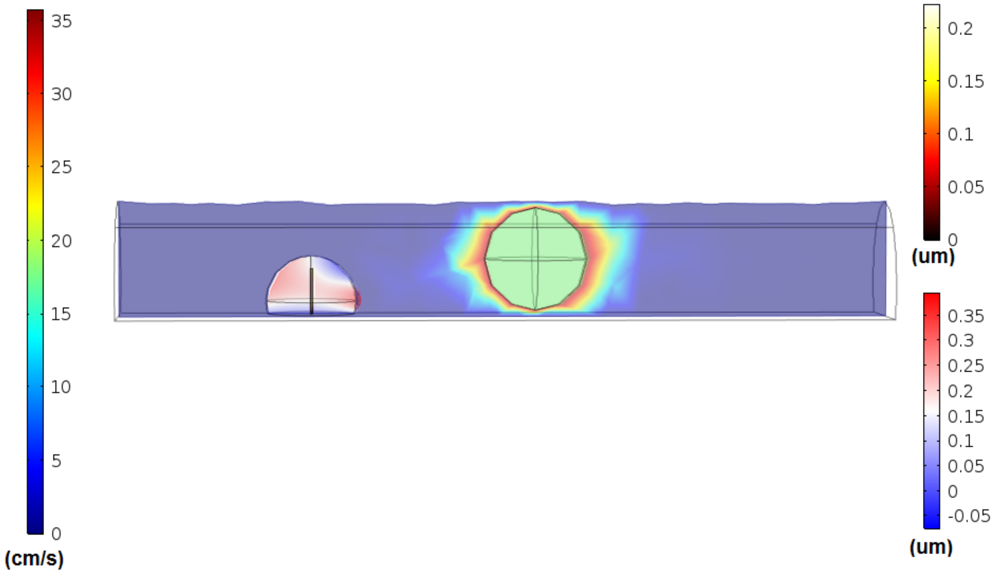

Figure 4.1: Finite-element modeling of a canal neuromast in the presence of a dipole stimulus. The left color bar represents the flow velocity within the canal. The upper right color bar represents deflection of the IPMC sensor beam while the lower right color bar represents the deflection of the cupula-like structure.

Emulating the setup in [66], a dipole source is placed within the canal to generate the periodic flow. To understand the scaling behavior of the canal neuromasts, two different dimensions are simulated, one at the mm scale and the other at the cm scale. The mm scale case is closer to the biological scale and the scale considered in analytical modeling, and is thus relevant to understanding the biological neuromasts and offering meaningful comparison with the analytical modeling results. On the other hand, the cm scale reflects the dimensions of many engineered lateral line devices and is relevant to practical design of such systems.

The range of dipole frequency used for the mm scale case is 60 to 1000 Hz, and that for the cm scale case is 6 to 30 Hz. These ranges are chosen so that the cupula in each case would produce sufficient movement and thus sensing signals. The amplitude of the vibration A is set to be much less than the radius of the sphere [66]. In particular, A is set to be 3 μm for the mm scale cases, and 30 μm for the cm scale cases in this work. Fig. 4.1 illustrates the simulated configuration for the canal-type lateral line system, where the hemisphere on the left represents the cupula (with an IPMC sensor beam embedded) and the sphere on the right represents the dipole source. Appropriate boundary and initial conditions are used in the simulation. In particular, the viscous fluid filling the canal was set to be at rest at time 0. The cupula is fully supported from the bottom, and so is the IPMC beam, which implies that their displacements at the bottom are zero. The cupula is located at the same center line of the dipole. Fig. 4.1 represents the flow field (mm/s) as well as the displacement of the structure during fluid movement. The plot is a slice from the three dimensional canal model. The simulation resulted in both the fluid flow profile and the displacement and deformation of the cupula (including the IPMC beam). Two different sizes of cupula structures are used for the mm scale, one with a radius of 0.35mm and the other with a radius of 0.7 mm. The shape of the cupula consists of a hemisphere sitting on a short cylinder. As a result, the heights of the cupula structures at mm scale are 0.4 mm and 0.8 mm, respectively. The distance between the cupula and the dipole source is 2 mm. Similar setups were used for the cm scale simulation, except all dimensions are 10 times of those in the mm scale case. The simulated canal is a long cylinder closed at both ends and flat at the bottom. For the mm scale simulation, the canal has a radius of 2 mm and length of 15 mm. Because the shape of the canal plays an important role in the flow profile [59], we choose the canal in this way to ensure that the periodic flow generated by the sphere moves easily to deflect the cupula-like structure, and to fit the cupula which has a flat bottom. Young's modulus directly influences the sensitivity of the structure, so several different values of Young's modulus are used for the cupula structure in the investigation.

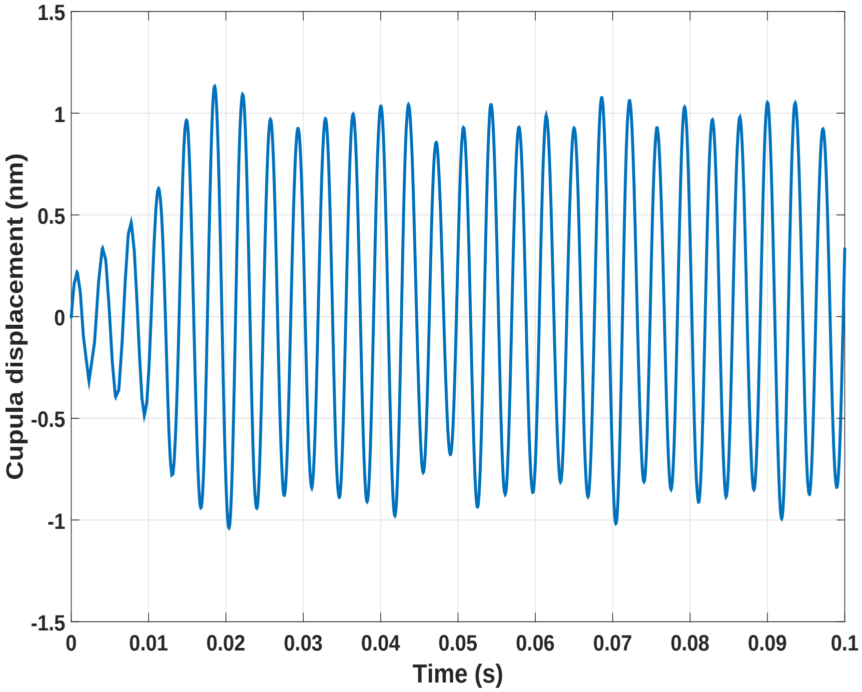

Figure 4.2: An example of cupula displacement trajectory for a 280 Hz dipole stimulus, where the radius of the cupula was 0.7 mm and the Young's modulus was 2000 Pa.

4.2.2 Simulation Results: Cupula Displacement

The periodic fluid movement inside the canal produces a periodic movement of the cupula structure at the same frequency at the steady state. Fig. 4.2 shows an example of the cupula displacement response in the presence of a dipole source that vibrates at 280Hz, where the cupula with radius 0.7 mm is used. From the figure, the displacement (still on track to the steady state) is almost periodic. Using fast Fourier transform (FFT), we can extract the amplitudes of the movement corresponding to different frequencies, as illustrated in Fig. 4.3.

Fig. 4.4 shows the amplitude of the cupula displacement as a function of the dipole stimulus frequency, where the cupula radius is 0.7 mm and its Young's modulus is 300 Pa. It can be seen that the displacement increases first with the frequency of the dipole until it reaches a maximum at

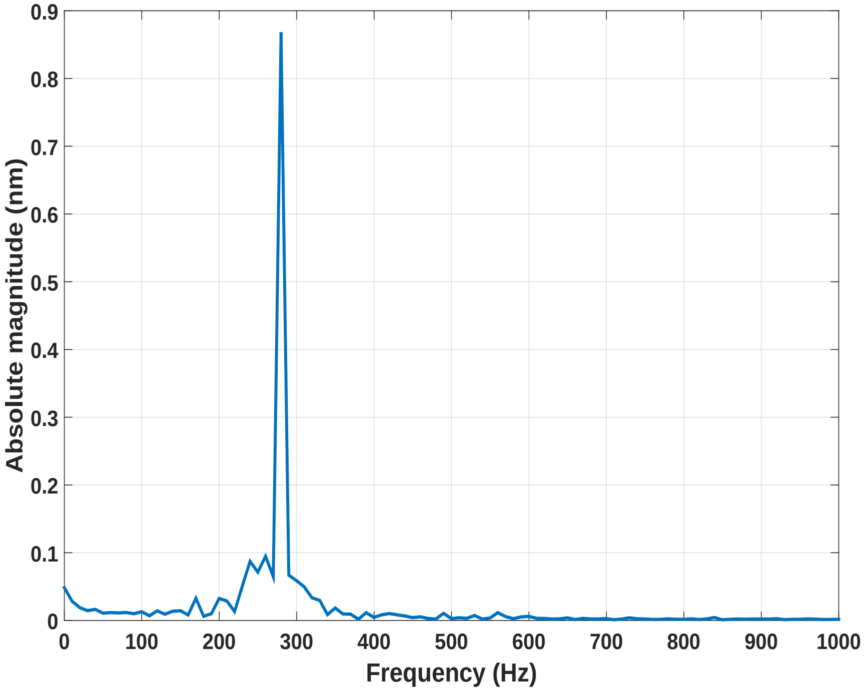

Figure 4.3: Exacted amplitude of cupula movement, where the radius of the cupula was 0.7 mm and the Young's modulus was 2000 Pa.

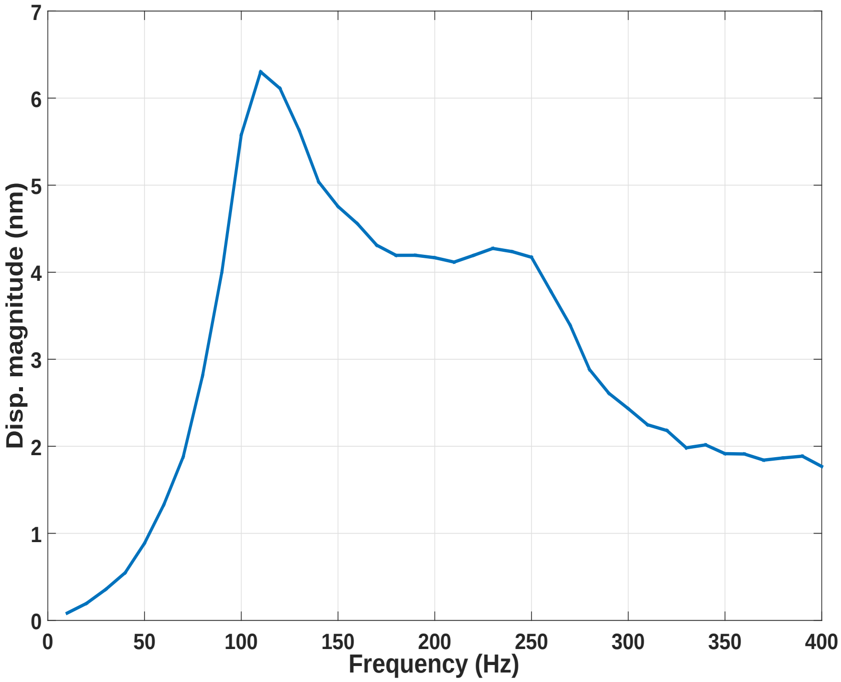

Figure 4.4: Displacement magnitude of the cupula structure with radius 0.7 mm as a function of the dipole frequency, where the Young's modulus was 300 Pa.

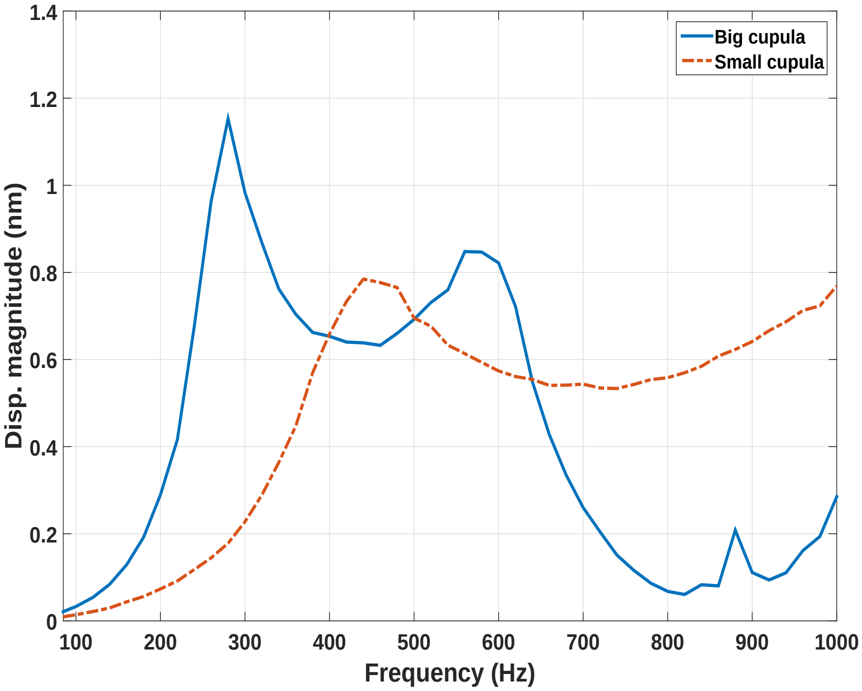

Figure 4.5: The comparison with radius 0.7 mm as a function of the dipole frequency, where the Young's modulus was 2000 Pa for both.

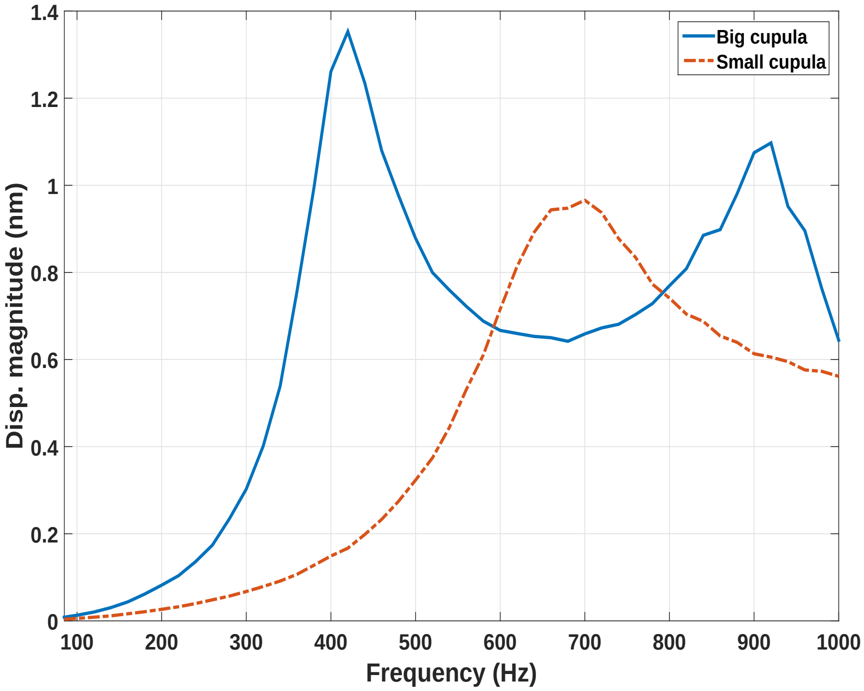

Figure 4.6: The comparison of the displacement responses between the two mm scale cupula structures, where the Young's modulus was set to be 5000 Pa for both.

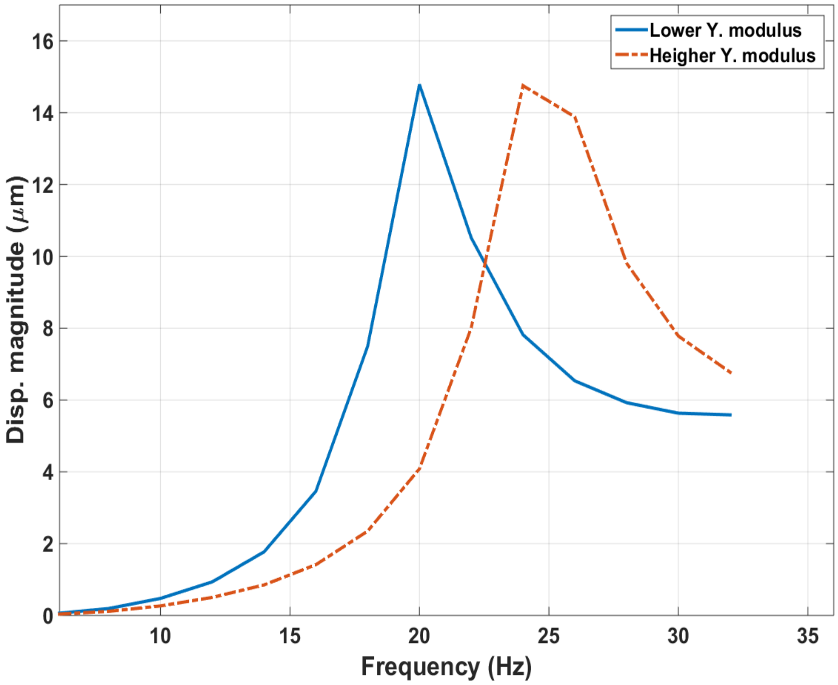

Figure 4.7: Comparison of the displacement responses of cupula structures (radius of 0.7 cm) with different Young's moduli (300 Pa and 600 Pa).

about 120 Hz. The amplitude then drops with frequency until it reaches another peak (lower than the first one) at about 230 Hz. These peak frequencies are considered to be related to the resonant frequencies of the cupula structure in the fluid. Overall the frequency behavior of the modeled cupula shows good agreement with the behavior of biological cupula in [67].

Fig. 4.5 shows the comparison of the simulation results for the two cupula structures at the mm scale, where the Young's modulus is set to be 2000 Pa for both cupula structures. From the figure, the larger cupula structure has a lower peak frequency, as expected. Fig. 4.6 shows the frequency responses of the two cupula structures but with a higher Young's modulus (5000 Pa). It can be seen that overall the peak frequencies for both structures have increased comparing to the case with lower Young's modulus (2000 Pa). These results are consistent with one's expectations, as the resonant frequency of a structure increases with its stiffness and decreases with its mass (size).

We next present the results on the cm scale cases. The transition from the mm scale to the cm scale is crucial because of its relevance to practical engineered lateral lines. A cupula structure with radius of 0.7 cm is simulated in a canal with length of 15 cm and radius of 2 cm. Two different values of Young's modulus, 300 Pa and 600 Pa, are used. Fig. 4.7 shows the displacement amplitudes of the cupula structures, where one can observe that the peak frequencies are much lower than those for the mm scale capula structures, and that the softer cupula has a lower peak frequency. These results again demonstrate the important roles of dimensions and stiffness play in the sensor's sensitivity and operating frequency range.

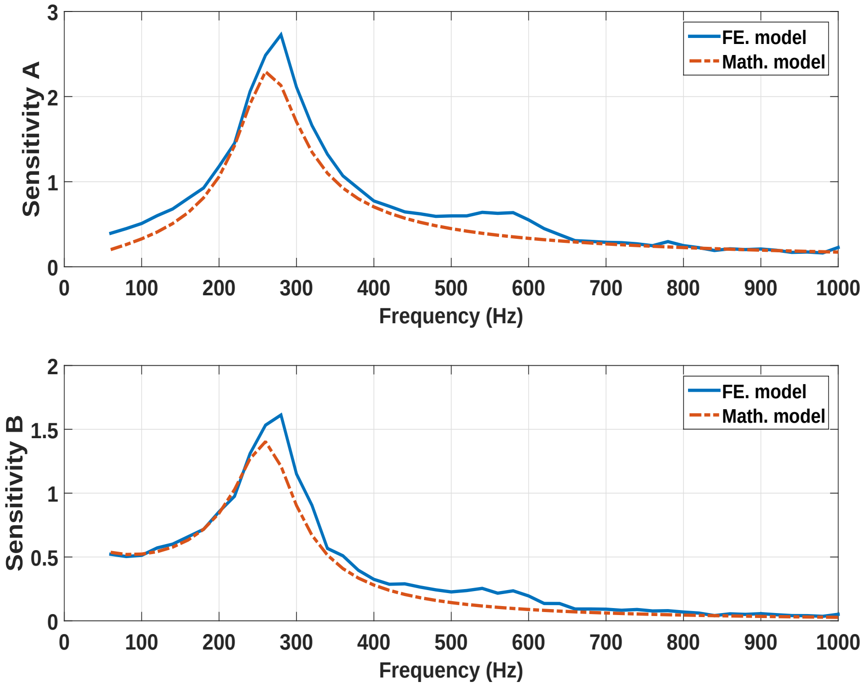

Figure 4.8: Comparison between the FE model and the analytical model for capula radius of 0.7 mm and Young's modulus of 2000 Pa. The sliding stiffness in the analytical model = 2.6 N/m.

4.2.3 Comparison between Numerical and Analytical Results

As stated before, one purpose of this work is to use the numerical model to validate the analytical model in [66]. The analytical model has a few parameters that need to be identified. Some parameters are readily known from the simulation setting, examples of which include the fluid viscosity and the canal diameter. The sliding stiffness of the cupula, however, needs to be calculated. To do this, we use the finite element model to apply a range of constant loads to the cupula and then calculate the corresponding displacement. The slope of the obtained displacement-load curve is taken as the required sliding stiffness in each case of cupula size and stiffness.

To present the results, we have normalized the cupula displacement in the finite element model (FE) and the analytical model by the fluid velocity to get the sensitivity A (in the unit of ms),

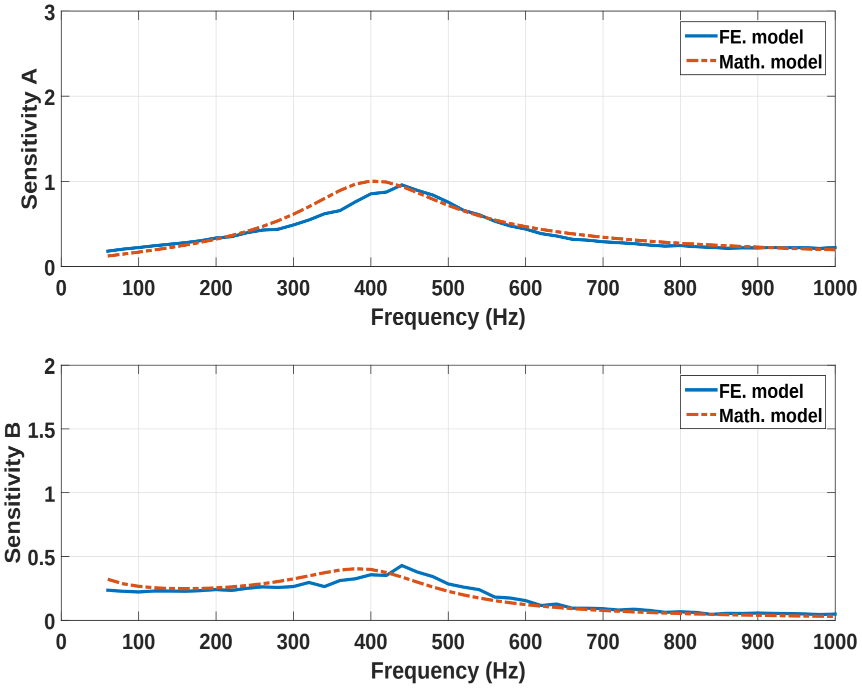

Figure 4.9: Comparison between the FE model and the analytical model for capula radius of 0.35 mm and Young's modulus of 2000 Pa. The sliding stiffness in the analytical model = 1.2 N/m.

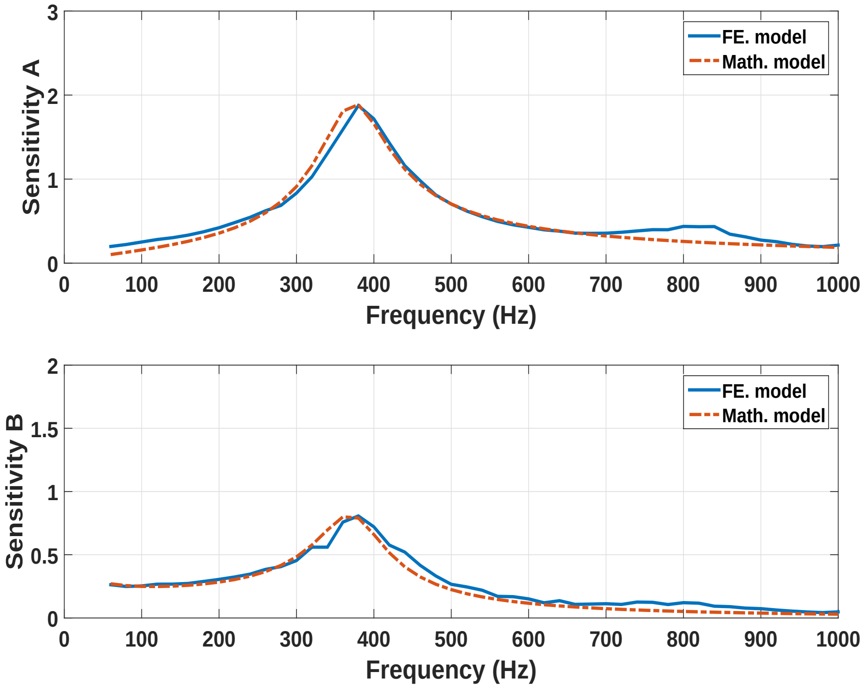

Figure 4.10: Comparison between the FE model and the analytical model for capula radius of 0.7 mm and Young’s modulus of 5000 Pa. The sliding stiffness in the analytical model = 5.4 N/m.

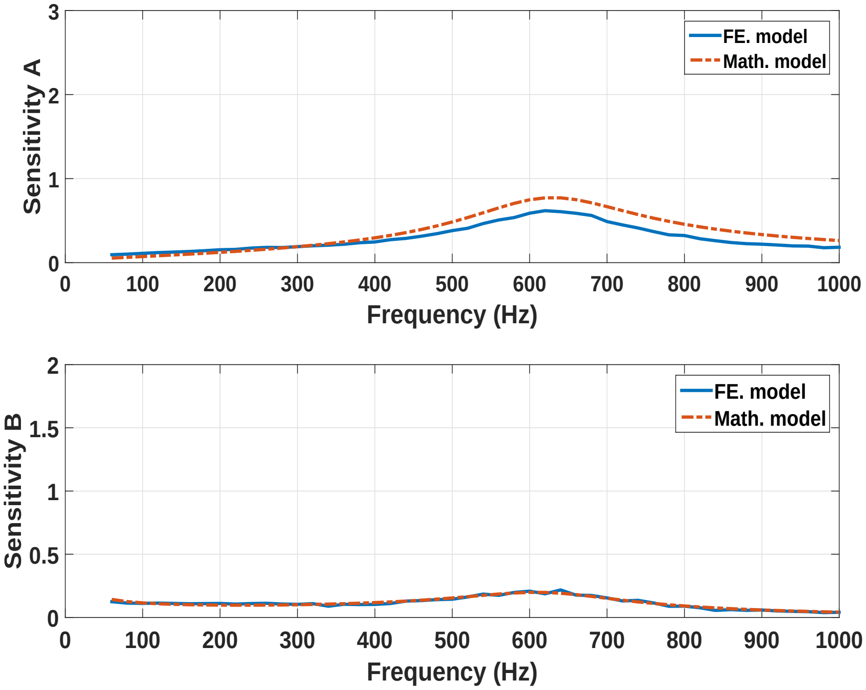

Figure 4.11: Comparison between the FE model and the analytical model for capula radius of 0.35 mm and Young's modulus of 5000 Pa. The sliding stiffness in the analytical model = 1.9 N/m.

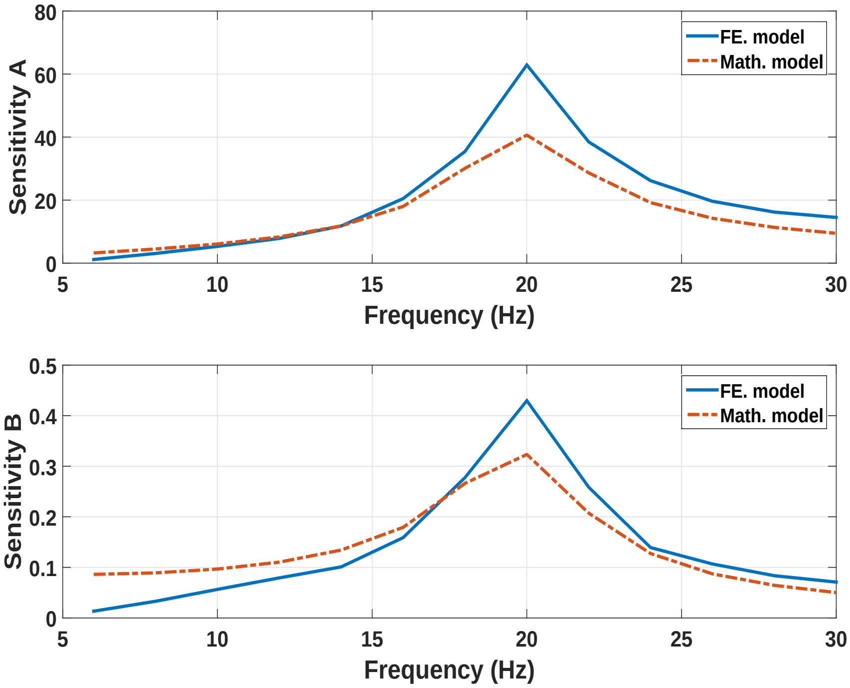

Figure 4.12: Comparison between the FE model and the analytical model for capula radius of 0.7 cm and Young's modulus of 300 Pa. The sliding stiffness in the analytical model = 1.52 N/m.

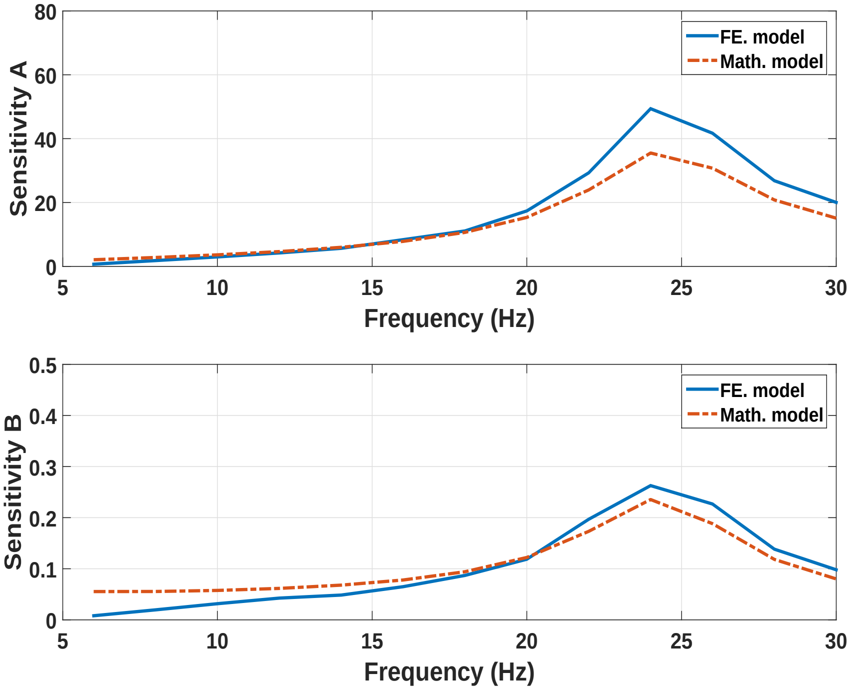

Figure 4.13: Comparison between the FE model and the analytical model for capula radius of 0.7 cm and Young's modulus of 600 Pa. The sliding stiffness in the analytical model = 3.6 N/m.

and by fluid acceleration to obtain the sensitivity B (in the unit of $\mathrm{nm} \cdot \mathrm{s}^2 (\mathrm{mm})^{-1}$), to examine the match between the FE results and the analytical model in the millimeter and centimeter dimensions scales. Figs. 4.8 - 4.11 show the comparisons for the mm scale cases, while Figs. 4.12 and 4.13 show the results for the cm scale cases. In all these comparisons, for the numerical model, the fluid displacement amplitude is obtained by averaging the dipole-generated flow field close to the cupula. The detailed information on each comparison (cupula size and Young's modulus) can be found in the figure captions. Overall it can be seen that the FE model has good agreement with the analytical model for the mm scale cases, both in terms of the value of the peak frequency and in terms of specific values of sensitivity. The slight discrepancies between the simulated and analytical results can be attributed to some ideal assumptions made in deriving the analytical model, such as the uniform flow field (while the dipole-generated flow is not spatially uniform). On the other hand, in the comparisons for the cm scale cases, even though the peak frequencies still match well, the discrepancies in sensitivity become much bigger, which points to the limitation of the analytical model when the cupula is scaled up.

4.2.4 IPMC Flow Sensor Output

The IPMC sensor is embedded inside the cupula, and thus the deformation of the cupula imposes a mechanical stimulus on the IPMC, which in turn produces an electrical signal. The simulation of beam IPMC flow sensor model under bending load excitation, as described in Section 4.1, is implemented with COMSOL Multiphysics 5.2 finite element software packages. As we stated in Section 4.1.1.2, four physics packages are used to implement the sensor model: fluid structural-interaction, transport of diluted species, general-form PDE to generate the electrical potential within the nafion, and electrical current physics. The FSI module is used to describe the linear

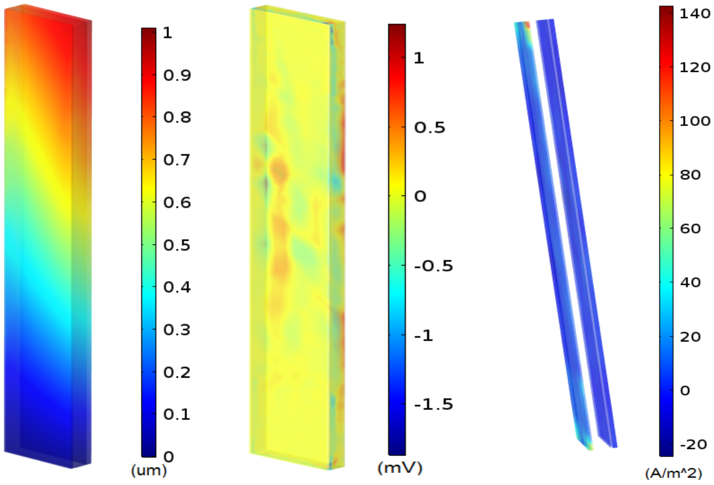

(a) (b) (c)

Figure 4.14: Simulation results on the IPMC sensor beam embedded in the cupula: (a) Sensor beam displacement; (b) Electrical potential distribution within the Nafion polymer; (c) Electrical charge density distribution in the vicinity of the IPMC electrodes.

elastic material under oscillatory flow. The PNP model, which is used to describe the electrical potential and the cation concentration inside the Nafion during the deformation, is realized through the transport of diluted species physics and the general-form PDE physics. The implementation of the IPMC model under oscillatory stimuli is achieved with two separate computations. The deformation of the IPMC sensor is calculated first, followed by the execution of the PNP model, which uses the deformation data from the first study computation as input. A short-circuit current, which is the sensor output, is collected by imposing the electrodes with zero potential and integrating the collected current density throughout the electrode surface. Fig. 4.14 shows a snapshot of displacement, electric potential, and charge distribution within the IPMC when the cupula is subjected to a dipole stimulus of 18 Hz. Here the cupula has a radius of 0.7 cm with Young's modulus of 600 Pa, and the IPMC beam is 7 mm long, 1.2 mm wide, and 0.15 mm thick.

4.3 Fabrication of Artificial Canal Neuromast

The fabrication of the cupula neuromasts is done by poring an Ecoflex00-30 (A), Ecoflex-30 (B), and a silicone oil into a 3D-printed mold. The custom-design is created using SolidWorks software. The prototype is shaped as a smooth hemisphere to mimic a cupula-like structure (Fig. 1.2 (c)). The prototype is formed with a cap which is used to protect the mixture and to create a place to insert the IPMC flow sensor. Fig. 4.15 (a) shows the SolidWorks design of the canal-type cupula-like structure. The diameter of the cupula is 0.7 cm and the height is 0.8 cm. Once the design is finalized in SolidWorks, the mold parts are printed with a 3D printer (Objet Connex350, Stratasys Ltd.), as shown in Fig. 4.15 (b). An ultrasonic cleaning process is conducted to make sure that the mold is free of any impurities caused by the printing process.

The liquid Ecoflex A and B are initially mixed with the Silicon oil in the ratio of 3:1:2 and injected into the mold. After that, the mold is placed over a hot plate under 70°C for 15 minutes in order to achieve a flexible structure. The IPMC fabrication process follows the traditional impregnation-reduction ion-exchange process [7,45,91]. Following the IPMC fabrication, an additional step of encapsulation is conducted with a parylene coating of 20 μm, as can be seen in Fig. 4.15 (c), followed by a water drive-in process under 70°C for three days [92]. Finally, the IPMC sensor is inserted into the cupula structure (in particular, the slot) through the slit at the bottom of the cupula-like structure. Fig. 4.15 (d) shows the fabricated cupula-type with the IPMC sensor embedded in the center of the structure. In this paper, one type of cupula-like structure is studied with fixed dimensions and stiffness. Both of which can be modified for the future work by changing the mold design to implement different cupula-type dimensions, and by adjusting the ratio of the raw materials and/or changing the baking temperature respectively to have a variety values of Young's Modulus.

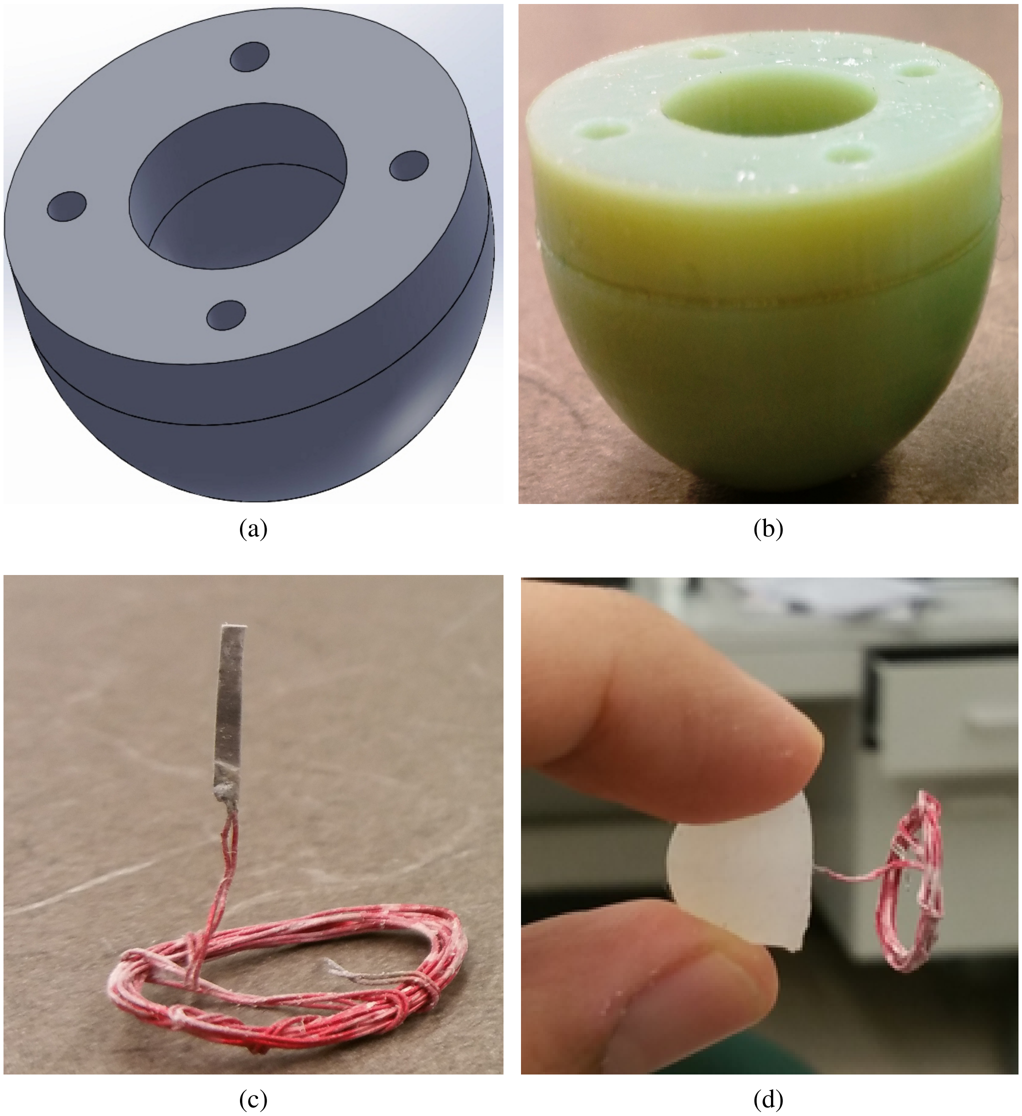
(a)
(b)
(c)
(d)

Figure 4.15: Fabrication of cupula-like structure: (a) design schematic of the cupula-like structure; (b) 3D-printed mold parts; (c) fabricated IPMC flow sensor (1 cm long, 1 mm wide); (d) cupula-like structure-inspired IPMC flow sensor.

4.4 Characterizations of Artificial Canal Neuromast in a Dipole Flow

A periodic flow, generated by a vibrating sphere (a dipole source), is one of the most common methods to stimulate a lateral line system or its engineering counterpart. In this work we have conducted experiments to examine the proposed canal-type lateral line under a dipole flow stimulus in a still water tank.

4.4.1 Experimental Setup

Experiments are conducted by using a small plastic tube measuring 15cm in length and 2cm in radius, as shown in Fig. 4.16 to emulate the canal lateral line in the fishes. A mini-shaker (Type 4810, Brüel & Kjær) was mounted on an aluminum frame above the tube, generating vibration stimulus (back and forth) on the horizontal plane in the range of 2 to 20 Hz at a fixed amplitude of the electrical input to the mini-shaker. The dipole source used is a metallic sphere with diameter of 19.4 mm and excited by the mini-shaker. The sphere is placed deep enough below the oil surface. The cupula-inspired IPMC sensor is attached to a thin 3D-printed stick and extended to the same depth as the dipole source, as shown in Fig. 4.16. The cupula-inspired IPMC sensor is placed first with a distance of 2cm from the dipole source center. A laser displacement sensor (OADM 20I6441/S14F, Baumer Electric) is mounted above the tube to measure the vibration displacement of the mini-shaker as the input of the sensor. The mounting frame for the laser sensor is isolated from the frame where the mini-shaker is fixed. An amplification circuit [86] is used to measure the short-circuit current generated by the IPMC sensor. Control signal generation, sensing data acquisition, and processing are all performed through a dSPACE system.

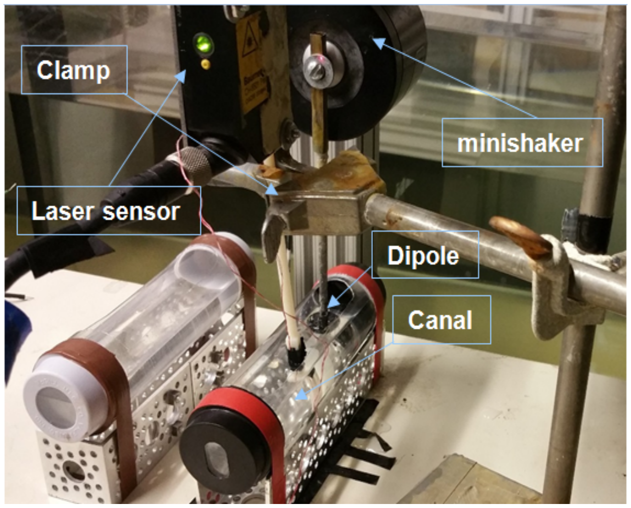

(a)

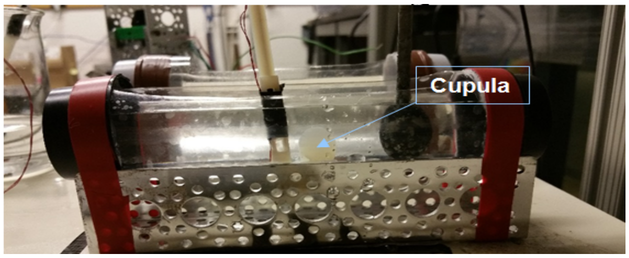

(b)

Figure 4.16: Experimental setup: (a) the canal assembly, mini shaker to apply a vibrating motion, laser sensor to measure the mini-shaker displacement; (b) Details of the canal assembly.

4.4.2 Results and Discussion

Experiments are conducted where the IPMC tip bending direction is parallel to the dipole source vibration direction. The canal is filled with silicone oil to emulate the biologic counterpart. The frequency of the dipole source was set to vibrate with a range of frequencies from 2 to 20 Hz. These experiments included two different locations for the the cupula-like structure. First, the dipole is set to vibrate at 2 cm from the cupula-like structure. For the second location, the dipole is set to vibrate at 3cm from the cupula-like structure. The dipole vibration produces periodic flow within the canal and the flow movement in turn stimulates the IPMC-embedded canal neuromast, resulting in an IPMC sensing output at the same frequency as the dipole source. We use fast Fourier transform (FFT) to extract the magnitude of the IPMC sensing signal, which is the short circuit current, and the dipole displacement corresponding to the dipole frequencies. Fig. 4.18, shows the comparison of the IPMC sensing signals at different frequencies for the two dipole locations. From the figure, it can be seen that the IPMC sensing output increases with the frequency of the dipole within the range of frequencies from 2 to 16 Hz. We observe that the IPMC sensing signal at frequencies above 18 Hz has lower magnitude. We attribute that to the dipole displacement, where we set the amplitude of the mini-shaker input voltage to be fixed but not the vibration amplitude.

4.5 Parameter Identification and Model Validation

4.5.1 Parameter Identification

Parameters for the model proposed in Section 4.1 are determined and used in model validation. The sensor dimensions (including the length and the thickness) and the thickness of the platinum electrode layers, are obtained directly through measurement. In particular, the thickness of the platinum layers is computed using the measured thickness of the polymer membrane before fabrication and that of the fabricated IPMC beam. For the IPMC sensor used in experiments, the dimensions are: length 10 mm and thickness 0.068 mm. The physical constants in the model include the temperature (T), which is measured directly using a thermometer, density (ρ), which is obtained through measuring the sensor weight and volume, the Faraday constant (F), and the gas constant (R). The value of anion concentration C_0 and the Young's modulus of the IPMC flow sensor are taken from [93]. The Young modulus of the cupula-like structure is obtained experimentally as follows. We subject the cupula to a displacement and measure the load and the deformation. A high-precision load cell device (Transducer Techniques, GSO 10g) is used to measure the applied load and a laser displacement sensor (OADM 20I6441/S14F, Baumer Electric) is used to measure the resulting displacement. Fig. 4.17 shows the measured stress-strain relationship to obtain the Young's modulus of the cupula. The electrical conductivity of the electrode (σ) is determined with the measured sensor surface resistance and the dimensions of the electrode. Table 4.1 lists the aforementioned parameters and constants.

The remaining parameters include the diffusion coefficient D and dielectric constant ε, both of which are obtained through an artificial neural network-based data fitting process [69]. The Matlab toolbox ($nnstart$) is used to prepare a neural network with two inputs, which represent the parameters to be tuned, and one output, which represents the model fitting error. The network contains one hidden layer with 10 nodes. The number of hidden layers and nodes are chosen according to [87]. Specifically, we use the collected IPMC output magnitude when the dipole at 1 cm from the cupula as shown in Fig. 4.18, for the purpose of parameter identification, and these same parameters are used in the other scenario (different dipole location) for model validation. The finite element simulation is used to obtain the predicted sensing signal magnitude for the prescribed dipole stimulus,

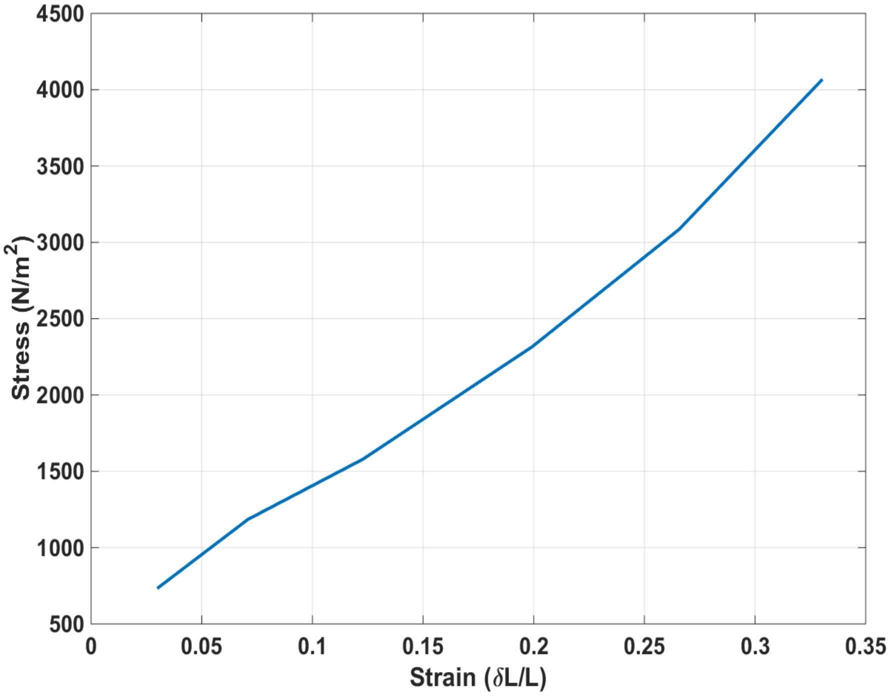

Figure 4.17: Measured stress-strain relationship curve for identifying the Young modulus of the artificial canal neuromast.

for any given set of parameters.

As stated in [69], we follow a tutorial provided by Matlab Inc. [88] to implement the neural network model, which offers a step-by-step instruction on how to use the command ($nnstart$). The average error between the predicted and measured sensing signals is treated as the output of the neural network for the corresponding input values (i.e., the parameters used in the simulation). A total of 25 sets of parameters, chosen within feasible ranges of these parameters, are used in conducting the simulation. Twenty sets of the obtained input-output data are used to train the neural network, while the remaining sets are used to test the obtained neural network model. The established neural network model is then used to to serve as a fitness function to the optimization toolbox (*optimtool*) to find the optimum input vector that minimizes the output, which produces the optimal parameters (D, ε) for the data fitting. The obtained values for these parameters are also listed in Table 4.1. Fig. 4.18 shows the comparison between measured signal and the model prediction based on the identified parameters. It can be seen that overall the model captures well the magnitude of the sensing signal under the given stimulus.

4.5.2 Model Validation

The identified parameters are then used in the simulation of the sensor sensing signal under a dipole flow with different location of the dipole (3 cm away from the cupula). In particular, the same set of frequencies are used to run the simulation by using the identified parameters.

Fig. 4.18 is also show the the comparison between the measured sensing signals and the model-predicted sensing signals for the new distance. Overall, the figure shows a good agreement between the measurement and model prediction. Given that two of the key model parameters are identified using only part of the data under a dipole stimulus, the reasonable match across all the data points

Table 4.1: Model Parameters of Canal-type Neuromasts.

F (C mol^{-1})	R (J mol^{-1}K^{-1})	T (K)	z
96487	8.3143	290	1
D (m^2 s^{-1})	C_0 (mol m^{-3})	ε (F m^{-1})	σ (S m^{-1})
1.8×10^{-12}	1085	2×10^{-3}	2200
ρ IPMC (kg m^{-3})	ρ Cupula (kg m^{-3})	E IPMC (*Pa*)	E Cupula (*Pa*)
8571.4	2431.5357	5.116×10^8	9633

provides strong support for the validity of the model. Specifically, the model is able to capture the magnitude of the sensor sensing signals.

Despite the general good agreement, there are some modest discrepancies between the experimental data and the simulation results, which we attribute mainly to imperfection in fabrication of the IPMC flow sensor and in the experimental setup.

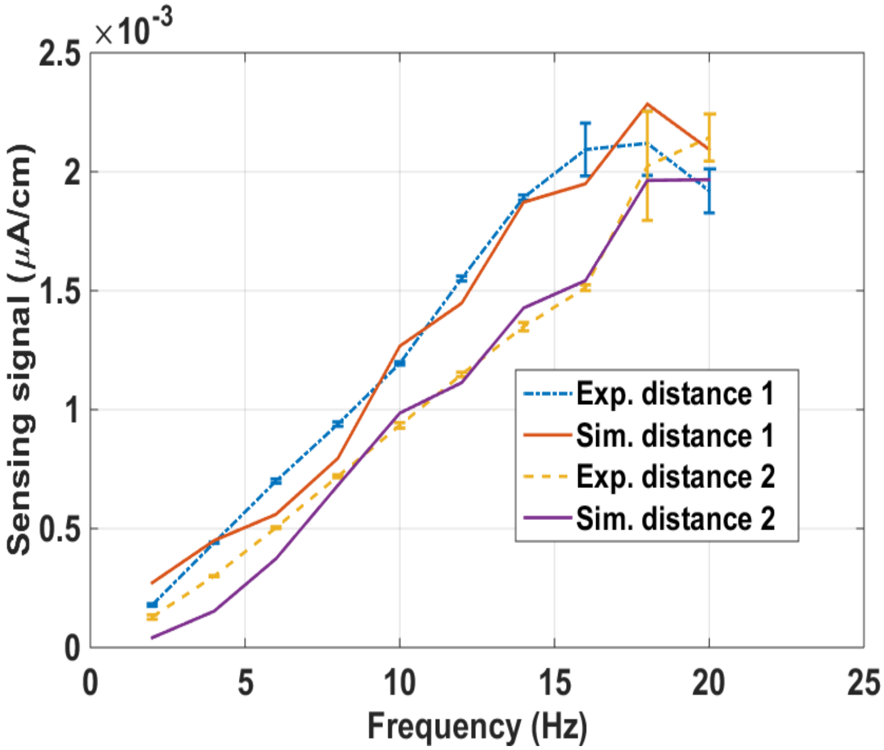

Figure 4.18: Comparison between the experimental and the simulation sensing signal for two distances.

Chapter 5

A Pressure Gradient Sensor Inspired by the Canal Neuromasts of Fish

In this chapter, we present, to our best knowledge, the first pressure difference sensor inspired by the canal neuromasts of fish. Such a sensor could be used by underwater robots and vehicles for object detection, angle of attack measurement, and source localization. Unlike most of the aforementioned artificial lateral line systems on pressure sensing or object localization, where an array of sensors were used, the proposed sensor utilizes one sensing element embedded in a cupula-like structure, which is immersed in a canal (a "semicircular" channel) filled with a viscous fluid. The employed sensing element, which is an IPMC sensor, serves as an artificial hair cell sensor that produces an electrical output in response to the motion of the cupula. As an illustration, the pressure difference sensor is integrated within a fish-like body, and the two ends of the semicircular channel are "pores" like the ears of a fish. Unlike a fish canal that has open ends to the surface of the body, the two pores of the proposed sensor are covered with a thin latex membrane, to prevent the canal fluid from mixing with the ambient fluid.

5.1 System Development

The fish-like structure was produced with a multi-material 3D printer (Objet Connex 350, Stratasys) using a hard material (VeroWhite), and it consisted of two parts, as shown in Fig. 5.1. The front part had a semicircular canal (inner diameter 3 cm), to house the cupula (see Fig. 5.2 (b)), and the two pores (diameter 2 cm) at both ends of the canal would be covered by two membranes. The membrane was made of natural latex rubber (thickness 0.1 mm). The cupula structure was 3D-printed with the same multi-material printer (Objet Connex 350, Stratasys), using the soft material. The cupula structure, as shown in Fig. 5.2 (b), was printed as one piece and comprised of two parts: a cylinder (length 1.5 cm, radius 0.3 cm) is on top of another cylinder (length 0.5 cm, radius 0.13 cm) with a slot (length 1.7 cm, cross-section of 0.2 mm by 0.2 cm) passing through the two cylinders for housing the IPMC sensor. The IPMC fabrication process followed the traditional impregnation-reduction ion-exchange process [7, 44]. Following the IPMC fabrication, an additional step of encapsulation was conducted with a parylene coating of 20 μm, followed by a water drive-in process under 70°C for three days [92]. Finally, the IPMC sensor was inserted into the cupula structure (in particular, the slot) through the slit at the bottom of the smaller cylinder.

5.2 Experimental Characterization

5.2.1 Experimental Setup

The rhythmic movement of the body appendages or the fins can be emulated by a vibrating sphere known as a dipole source. A dipole is often can be used as a stimulus in the study of a lateral line system or its engineering counterpart. In this paper, we have conducted experiments to examine the proposed sensor under an AC flow stimulus generated by a dipole source in a still water tank.

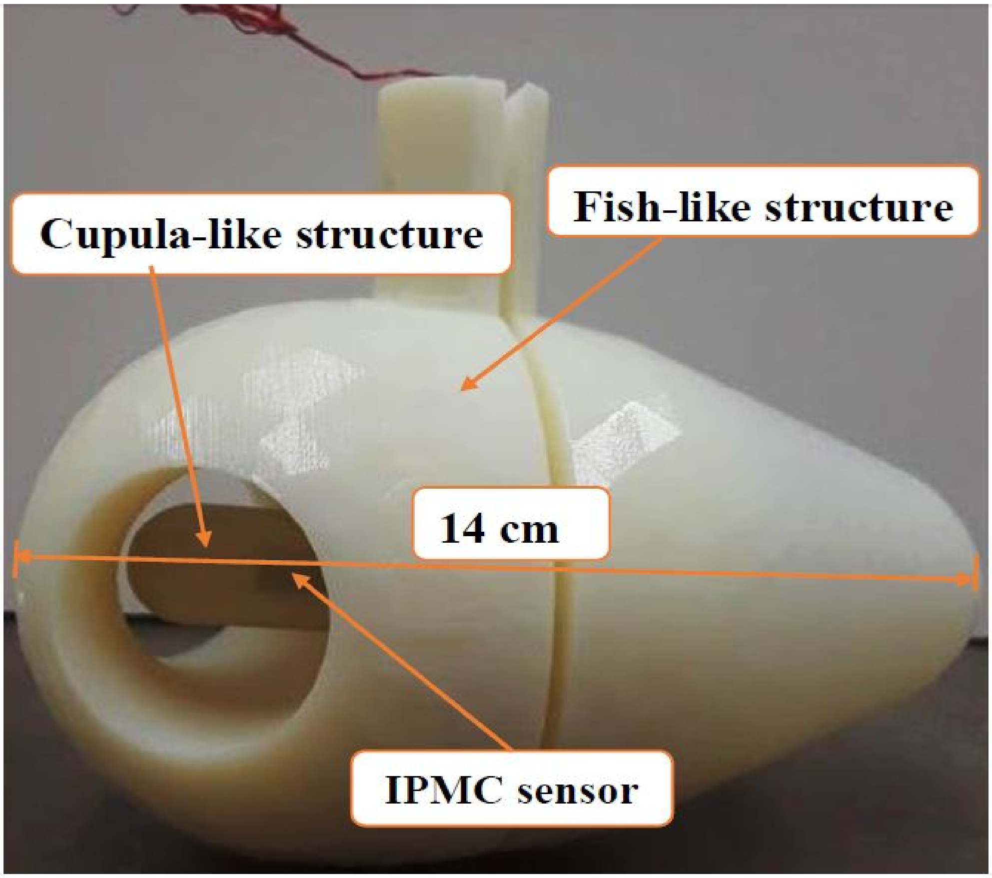

Figure 5.1: 3D-printed fish-like structure with two pores to be covered with natural latex rubber membranes.

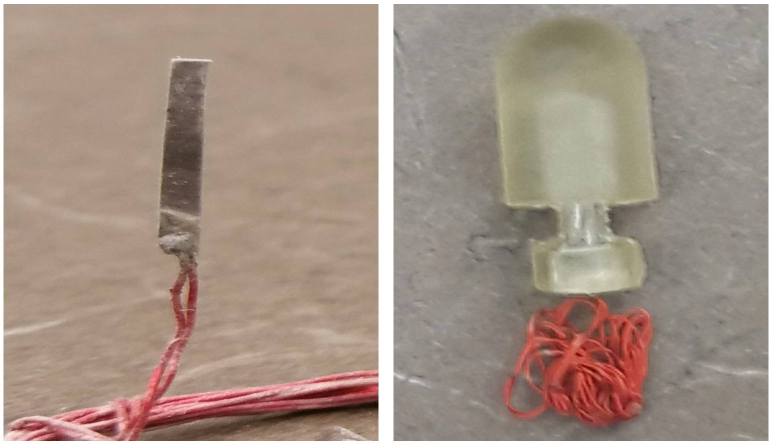
(a) (b)

Figure 5.2: Fabrication of the proposed sensor: (a) fabricated IPMC flow sensor (1.5 cm long, 2 mm wide); (b) 3D-printed cupula-structure with the IPMC sensor inserted.

Fig. 1.5 shows a schematic diagram of the proposed sensor and the experimental setup, while Fig. 5.3 shows a picture of the major elements that have been used in the experimental setup. Experiments were conducted in a water tank measuring $6 \times 2 \times 2$ ft^3. A mini-shaker (Type 4810, Brüel & Kjær) was mounted on an aluminum frame above the tank, generating vibration (back and forth) on the horizontal plane in a range of 2 to 30 Hz at a fixed amplitude of electrical input to the mini-shaker. The dipole source used was a metallic sphere with a diameter of 25 mm and excited by the mini-shaker. The fish-like structure was fixed to a metal rod via a 3D-printed connector. The 3D-printed connector securely held the fish-like body and the metal rod to ensure no slip when a rotational movement was applied. The top end of the metal rod was fixed on a metal connector, which was rigidly attached to a stepper motor (STM23S-2AE, Applied Motion) used to generate a rotation of the fish-like structure. The stepper motor was controlled via a microcontroller (Arduino-uno). The dipole source and the fish-like structure were completely submerged underwater at a depth of about 20 cm. The separation between the dipole source and the fish-like structure was about 10 mm when the fish-like structure was perfectly oriented towards the dipole. A laser displacement sensor (OADM 20I6441/S14F, Baumer Electric) was mounted above the water to measure the vibration displacement of the mini-shaker, which was used later in the data processing (see Fig. 5.5). The mounting frame for the laser sensor was completely isolated from the frame where the mini-shaker was fixed. The IPMC output was amplified with a two-tier amplification circuit [86] before the acquisition and processing by a lab PC equipped with a dSPACE system(dSPACE, DS 1104).

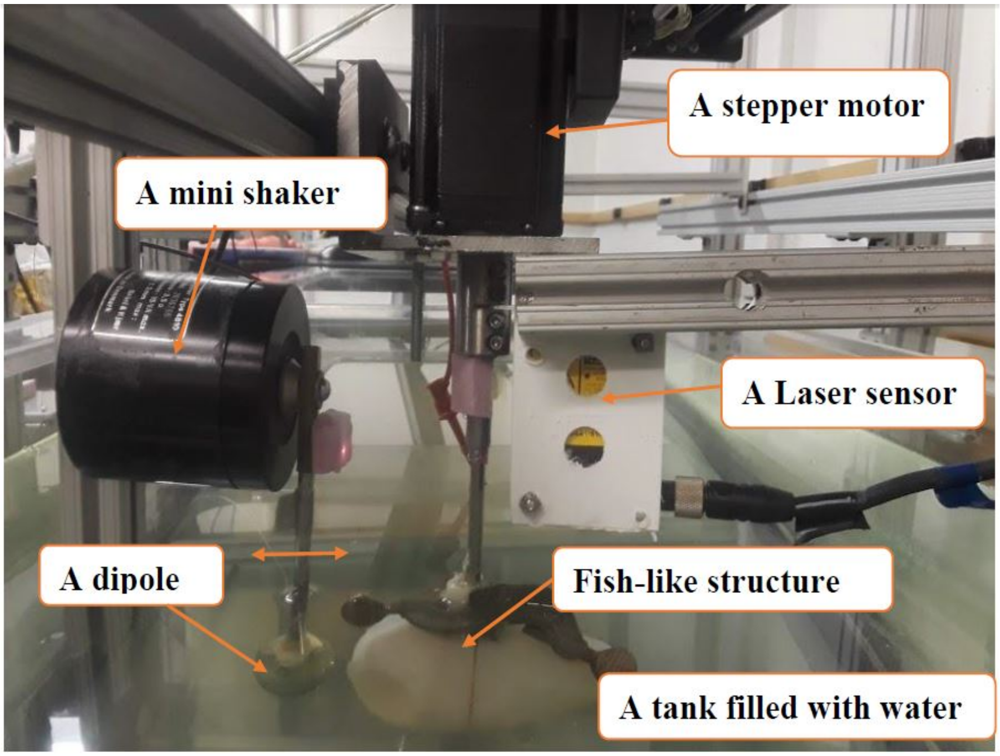

Figure 5.3: Picture of the experimental setup.

5.2.2 Experimental Results and Discussion

Experiments were first conducted for the case where the dipole source was placed at a fixed point while the fish-like structure was rotated at different angles relative to the dipole source, as illustrated in Fig. 1.5. The sensor was filled with silicone oil which provides better performance than water as suggested by our earlier work [94]. The frequency of the dipole source was set at 10 Hz. Conceivably, the pressure difference between the two pores would be dependent on the relative dipole location; in particular, the difference is expected to be largest when the dipole is facing one of the membranes and smallest when the dipole is at the midpoint between the pores. Through the pressure difference, the periodic movement of the dipole flow induces the flow movement within the canal and thus the motion of the IPMC-embedded cupula structure, resulting in an IPMC current output at the same frequency as the dipole.

We used fast Fourier transform (FFT) to extract the amplitude of the IPMC sensor output corresponding to different angles, shown in Fig. 5.4. Experiments were conducted 5 times at each angle, and the mean and standard deviation of these measurements are plotted in Fig. 5.4. From the figure, it is clear that as either pore approached the dipole source, the sensor output increased. When the dipole was at the midpoint (angle 0°) between the two pores, the IPMC sensor generated the lowest signal, indicating that the pore membranes were vibrating in phase. These results support that the sensor is able to capture the pressure difference between the two pores. The slight asymmetry between the left and right halves of the figure is attributed to the positioning errors for the dipole in the experiments.

To further characterize the dynamic behavior of the sensor in detecting the pressure differences, we next conducted experiments where the body was placed at several different angles relative to the dipole source while the dipole vibrated at a range of frequencies. Three angles were chosen to obtain the a frequency response (0°, 30°, and 45°) with a range from 2 to 30 Hz. Each experiment was repeated 5 times to compute the average and the standard deviation.

Fig. 5.6 shows the comparison of the sensitivity of the pressure sensor at different frequencies for the three angles. The sensitivity was taken by normalizing the magnitude of IPMC sensor output over the flow acceleration as characterized by the dipole acceleration (Fig. 5.5). From the figure, it can be seen that the sensitivity of the sensor decreased with the frequency of the dipole within the entire range of frequencies tested. The sensitivity of the sensor in the case of 45° was higher than the case of 30°, which was higher than that in the case of 0°. These results further support that this sensor is able to capture the pressure difference at different angular positions.

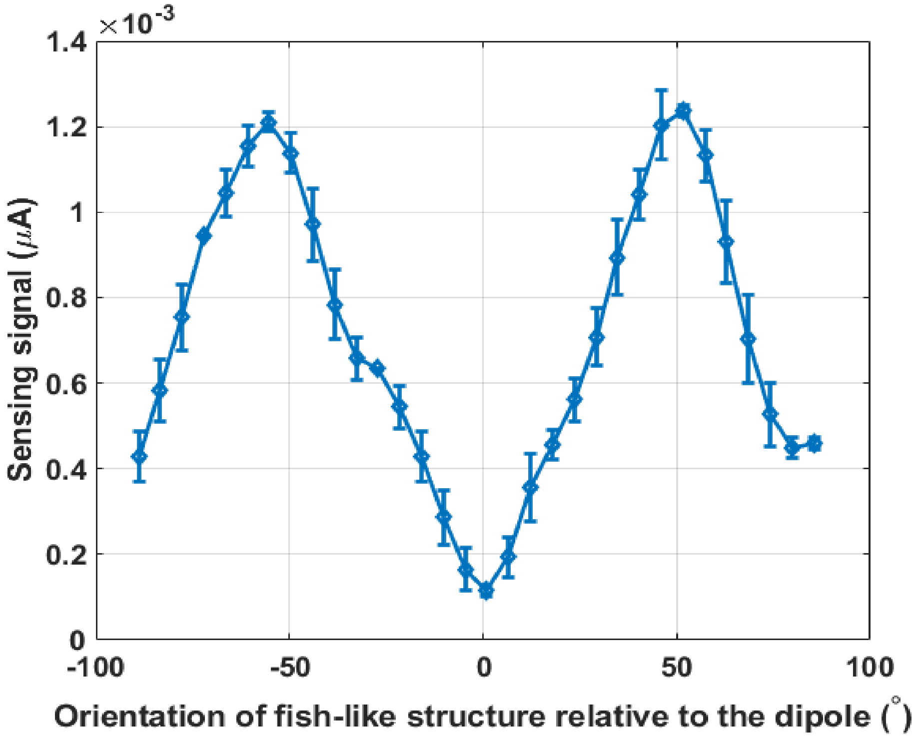

Figure 5.4: Experimental measurements of the sensor output where the fish-like structure is at different angles relative to a dipole source.

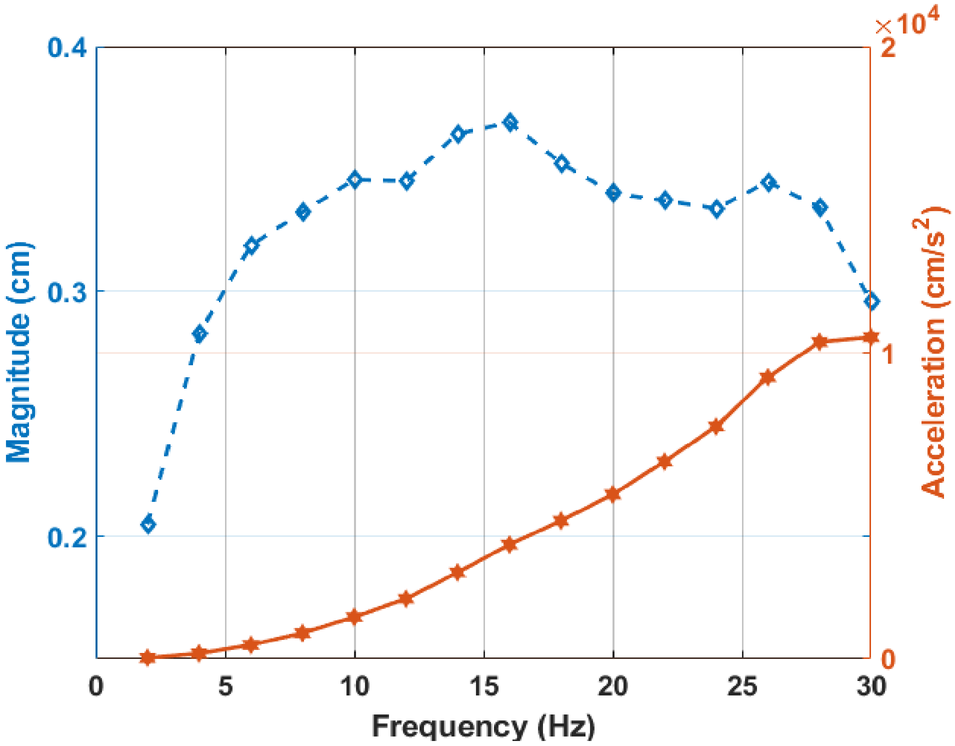

Figure 5.5: The dipole displacement and the acceleration in the frequency range 2 to 30 Hz.

5.3 Finite Element Model and Simulation

5.3.1 Finite Element Modeling

The response of a canal neuromast, biological or engineered, is due to the cupula deflection in response to a flow field, which is in turn due to a pressure difference between the canal pores. Finite element modeling is essential to the understanding of the sensor behavior and ultimately serving as a tool for design optimization. The modeling of the proposed pressure difference sensor under an oscillatory flow was implemented using COMSOL Multiphysics finite element software packages. The geometry and dimensions of the simulated fish-like structure, the cupula-like structure, and hair cell (IPMC sensor) were exactly the same as to those of the experimental prototype.

The modeling was done in two steps. In the first step a three-dimensional fluid-structure inter-

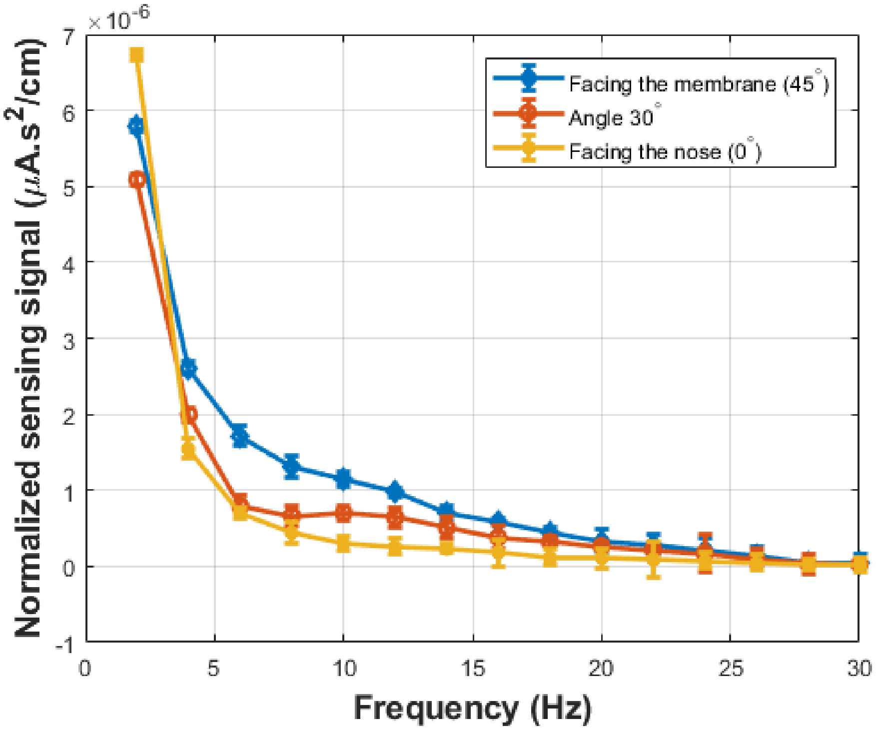

Figure 5.6: Comparison of the sensor frequency response at different angles relative to the dipole source.

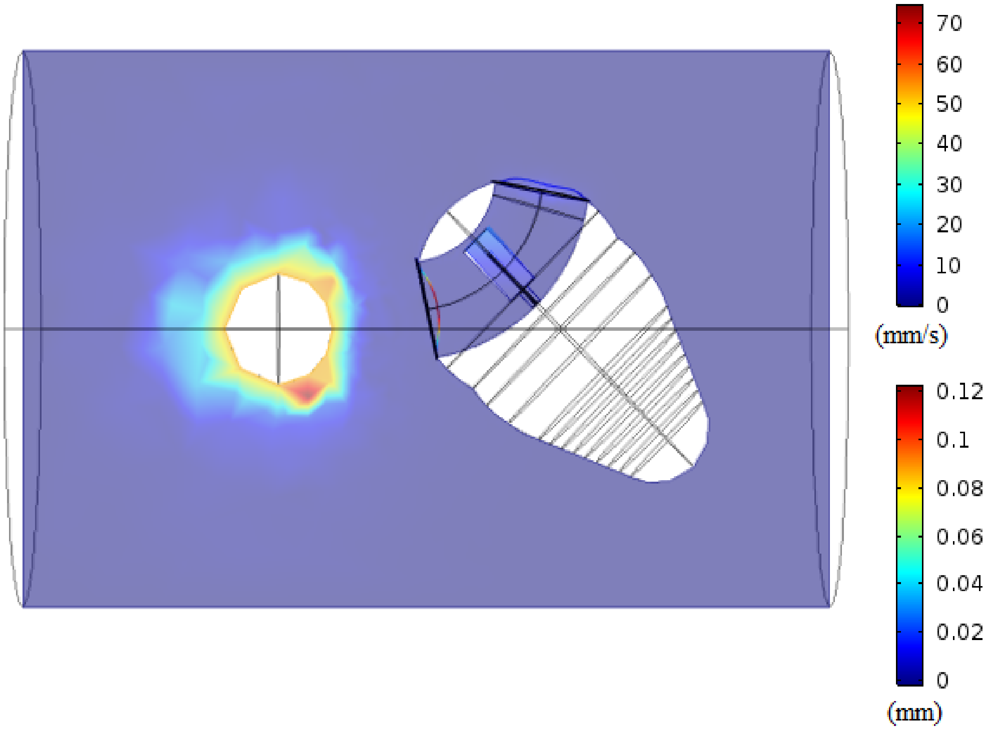

Figure 5.7: The finite-element modeling of a fish-like pressure difference sensor in the presence of a dipole source. The upper color bar represents the flow velocity within and around the sensor while the lower color bar represents the deflection of the membrane and the cupula-inspired IPMC flow sensor.

action (FSI) module was used to understand the cupula structure and membrane deflection under a dipole stimulus. The second step was to model the IPMC sensor physics and predict its output under bending.

5.3.1.1 Fluid-structure interaction (FSI)

In the first step of the simulation, FSI physics package was used to model the fluid-structure interaction between the sensor, dipole, and the surrounding water. The canal of the fish-like structure was filled with a fluid that had five times the viscosity of water, which was close to the viscosity of the biological counterpart. A dipole source was placed outside the canal to create a pressure difference across the pores (see Fig. 5.7). Similar to the experimental setting as shown in Fig. 5.3, in the simulation setup the fish-like structure could be oriented at different angles relative to the dipole source as seen in Fig. 5.9.

The dipole frequency was set to be 10 Hz and the amplitude of the dipole vibration was set to be 2.5 mm. Fig. 5.7 shows a snapshot of the simulated configuration, where the sphere represents the dipole source. The cylinder in the front part of the fish-like structure represents the cupula containing the IPMC sensor. Flexible membranes were attached to the pores. Appropriate initial and boundary conditions were used in the simulation. The water outside the fish-like structure and the canal-filling fluid were set to be at rest at the initial time. The membranes were fully attached to the boundaries of the canal pores. The cupula structure was fixed from the bottom, which implies that the displacement at the cupula base was zero. The snapshot in Fig. 5.7 shows both the flow field and the displacement of the cupula and membranes. Note that the plot was a slice from the three-dimensional model.

5.3.1.2 IPMC

The modeling of IPMC sensor under oscillatory flow was also achieved by using COMSOL Multiphysics finite element software packages. Four physics packages were used to implement the sensor model, fluid-structure interaction (FSI), transport of diluted species, general-form PDE to generate the electrical potential within the ion-exchange membrane (Nafion), and electrical current physics. The FSI module was used to describe the flow field and the linear elastic material under bending excitation due to the oscillatory flow inside the canal. The Poisson-Nernst-Plank equation (PNP), which describes the cation concentration and electrical potential dynamics was realized through the transport of diluted species physics and the general-form PDE physics modules. The implementation of the IPMC model under bending stimuli was achieved with two separate computations. The deformation of the IPMC sensor due to the dipole flow was calculated first (see 5.3.1.1), followed by the execution of the PNP model, which used the deformation data from the first computation as input. A short-circuit current was collected by imposing the electrodes with zero potential and integrating the collected current density throughout the electrode surface.

5.3.2 Parameter Identification

The parameters used in simulation were obtained based on the experimental setup. The dimensions of the IPMC sensor and the cupula-like structure, including the length, the diameter, the thickness, and the thickness of the platinum electrode layers, were obtained directly through measurement. In particular, the thickness of the platinum layers was computed using the measured thickness of

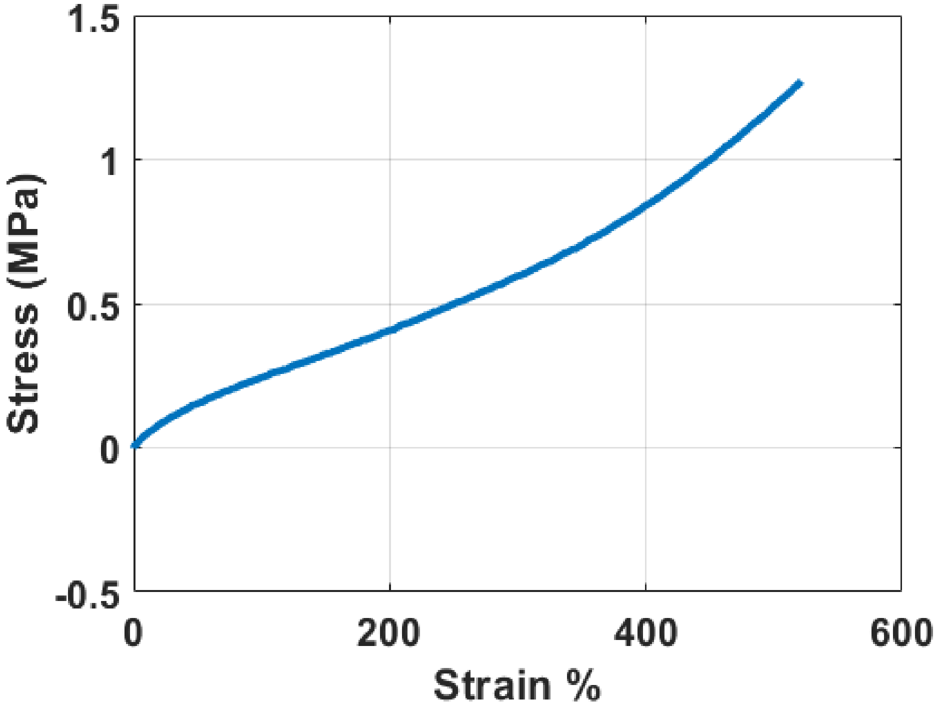

Figure 5.8: Experimentally obtained stress-strain curve of the cupula structure for estimating Young's modulus.

the polymer membrane before fabrication and that of the fabricated IPMC beam. The physical constants in the IPMC model include the temperature (T), which was measured directly using a thermometer, density (ρ), which was obtained through measuring the sensor weight and volume, the Faraday constant (F), and the gas constant (R). The value of anion concentration C_0 and the Young's modulus of the IPMC flow sensor were taken from [93]. The Young's modulus of the cupula-like structure was obtained based on experimental data on the stress/strain relationship collected through a tensile test (see Fig. 5.8). The electrical conductivity of the electrode (σ) was determined with the measured sensor surface resistance and the dimensions of the electrode. Table 2.1 lists the aforementioned parameters and constants.

The remaining parameters include the diffusion coefficient D and dielectric constant ε, both of which were obtained through an artificial neural network-based data fitting process [**?**]. The Matlab toolbox (*nnstart*) was used to prepare a neural network with two inputs, which represented the parameters to be tuned, and one output, which represented the model fitting error. The network contains one hidden layer with 10 nodes. The number of hidden layers and nodes were chosen according to [87]. Specifically, we used the collected IPMC output magnitude in the case of single frequency (10 Hz) and when the fish-like structure was orientated at different angles relative to the single dipole (data in Fig. 5.4), for the purpose of parameter identification. The finite element simulation was used to obtain the predicted sensing signal magnitude for the prescribed dipole stimulus, for any given set of parameters. The average error between the simulation and measured sensing signals was treated as the output of the neural network for the corresponding input values (i.e., the parameters used in the simulation). A total of 30 sets of parameters, chosen within feasible ranges of these parameters, were used in conducting the simulation. Twenty four sets of the obtained input-output data were used to train the neural network, while the remaining sets were used to test the obtained neural network model. The obtained values for these parameters are also listed in Table 5.1.

5.3.3 Simulation Results

The identified parameters were then used in the simulation of the sensor response. Simulations was first conducted for the case where the fish-like structure was oriented at different angles relative to the dipole source, the snapshots of which are shown in Fig. 5.9. Each sub-figure in Fig. 5.9 also shows the deflections of the pore membranes and the cupula-like structure, where the top color bar represents the membranes deflection (mm) and the lower color bar represents the cupula displacement (mm). In Fig. 5.9 selected six different angles (0°, 30°, 45°, 60°, 75°, 90°) out of 19

Table 5.1: Model Parameters of the Pressure Difference Sensor.

F (C mol^{-1})	R (J mol^{-1}K^{-1})	T (K)	z
96487	8.3143	290	1
D (m^2 s^{-1})	C_0 (mol m^{-3})	ε (F m^{-1})	σ (S m^{-1})
1×10^{-14}	1050	31×10^{-3}	2200
ρ IPMC (kg m^{-3})	ρ Cupula (kg m^{-3})	E IPMC (Pa)	E Cupula (Pa)
8571.4	1000	5.116×10^8	0.162×10^6

different angles (0 to 90 with step of 5°) used in the simulation study. As seen from the figure, when the dipole source is located at the midpoint between the two pores (0°), both membranes are fluctuating symmetrically, suggesting minimal pressure difference between the pores and minimal flow of the viscous fluid in the canal, which in turn leads to minimal displacement of the cupula.

Fig. 5.10 further shows the tip displacement amplitude of the cupula structure and the membrane displacement,as a function of the orientation of the fish-like structure with respect to the dipole source. It can be noted that magnitudes of both displacements show strong dependency on the orientation of the fish-like body relative to the dipole, with the maximum values occurring around 45^c and a trend consistent with the experimentally observed sensor output (shown in Fig. 5.4).

Fig. 5.11 shows the comparison between the measured sensing signal magnitude and the simulation sensing signal amplitude, under (10 Hz) dipole stimulation. Overall, the figure shows a good agreement between the measurement and simulation. Given that two of the key model parameters were identified using only part of the data under a dipole stimulus, the reasonable match across all the data points provides strong support for the validity of the model. Despite the general good agreement, there are some modest discrepancies between the experimental data and the simulation results, which we attribute mainly to the imperfection in fabrication of the membrane and the IPMC flow sensor, and in the experimental setup.

5.4 Orientation Control of Fish-like Body with Sensor Feedback

5.4.1 Sliding Discrete Fourier Transform (SDFT) Algorithm

In this section the utility of the proposed sensor is illustrated with feedback control of the orientation of the fish-like body using measurement from the pressure difference sensor. Discrete Fourier transform (DFT) can be used to extract the signal magnitudes of the sensor output at different frequencies. However, when the fish-like body rotates, the magnitude of the sensor output evolves with time. The sliding discrete Fourier transform (SDFT) algorithm [74, 75] performs joint time-frequency analysis and is a suitable method for computing a specific spectral bin based on a sliding window of *n*-time samples.

For a window of N samples, $\{x[n-N-1], \ldots\ldots, x[n]\}$, we can evaluate the kth spectral bin using DFT: for $0 \leq k \leq N-1$

$$X_k[n] = \sum_{m=0}^{N-1} x[n-m+1+k] e^{-j2\pi km/N} \tag{5.1}$$

Since we are interested in a single frequency f_0 for a dipole stimulus, it suffices to consider a single frequency bin $k = [\frac{f_0 N}{F_s}]$, where [.] denoted rounding to the nearest integer and F_s is the

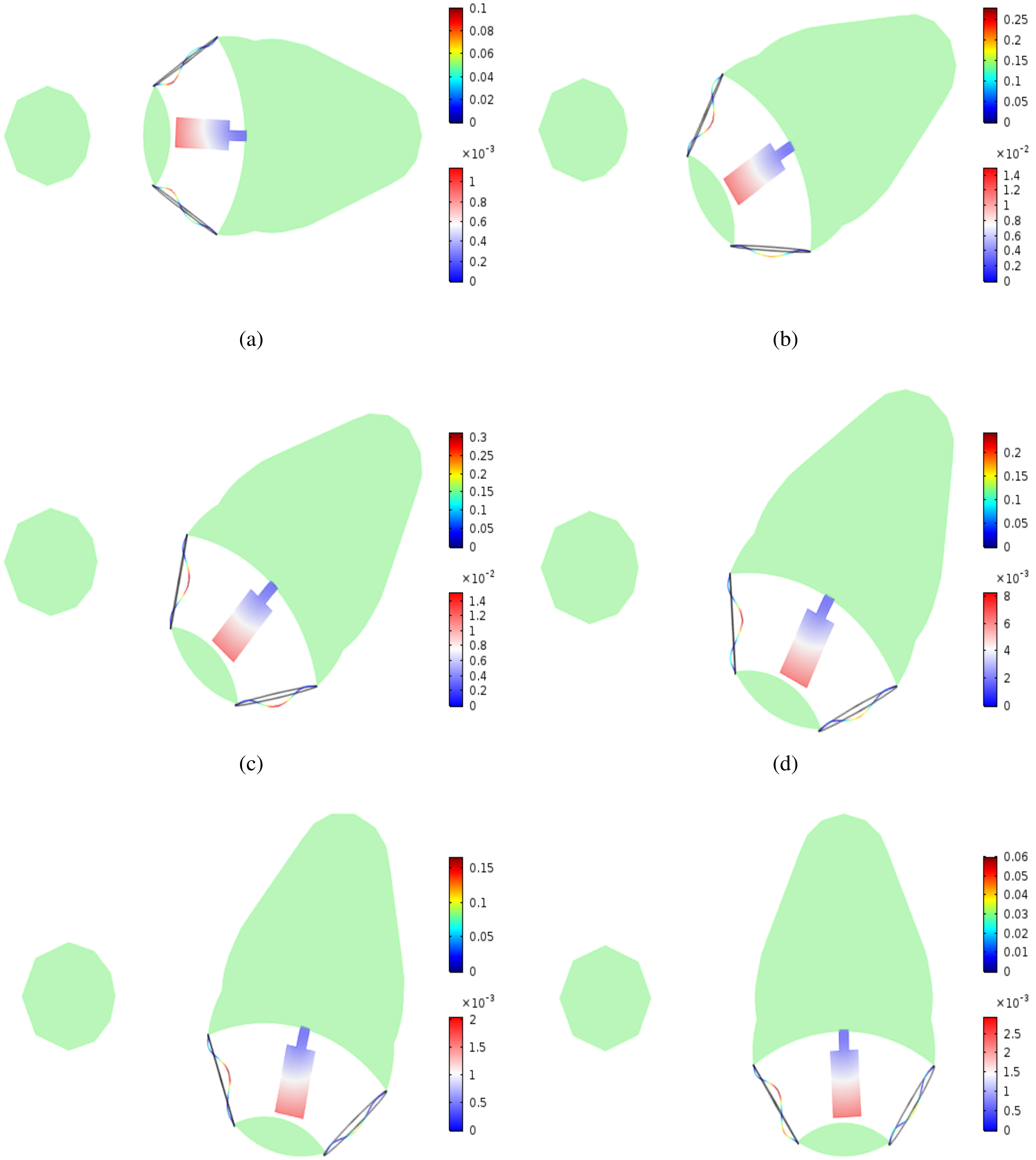

(a) (b)

(c) (d)

(e) (f)

Figure 5.9: Snapshots of simulation showing the membrane and the cupula displacement (units in mm) when the fish-like structure is oriented with different angles relative to the dipole stimulus, where the upper color bar represents the membrane displacement and the bottom color bar represents the cupula displacement: (a) 0°; (b) 30°; (c) 45° (d) 60°; (e) 75° (f) 90°.

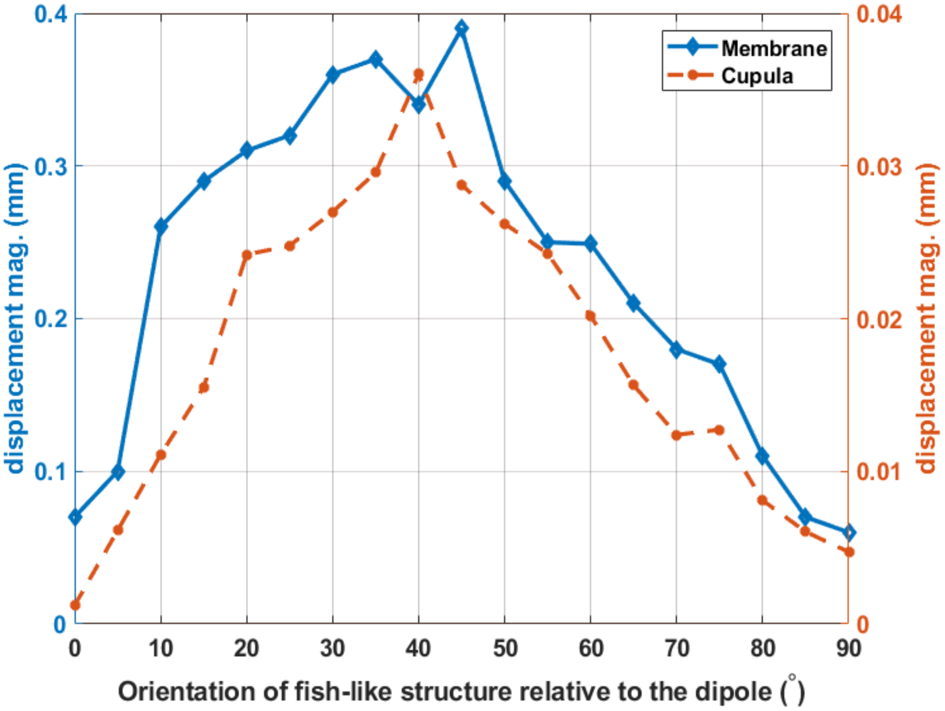

Figure 5.10: Computed magnitudes for the displacement of the membrane and for the tip displacement of the cupula, respectively.

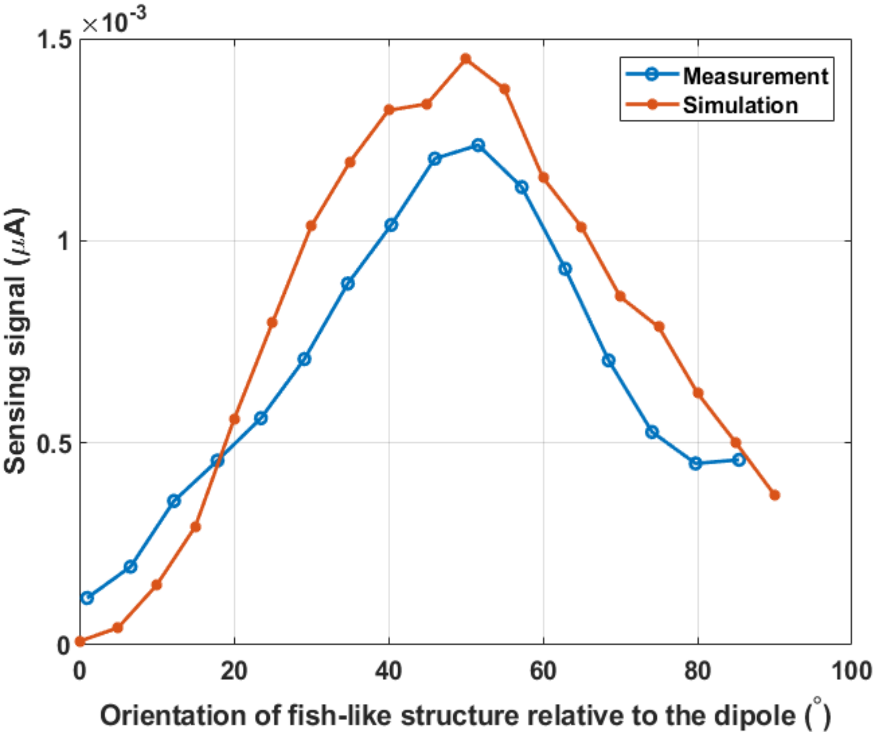

Figure 5.11: Comparison between the experimental and the simulation sensing signal.

sampling frequency to obtain the sensor signals. The SDFT algorithm, can be used to efficiently evaluate X_k recursively as the time index n advances:

$$X_k[n] = e^{-j\omega_0} X_k[n-1] + x[n] - x[n-N] \tag{5.2}$$

where $\omega_0 = \frac{2\pi km}{N}$. The resulting sequence from (5.2) is complex, for which the algorithm needs to compute the magnitude. The algorithm monitors $\mid X_k[.] \mid$, which defines the power density at f_0.

5.4.2 Feedback Controller

The proposed algorithm aims to orient the fish-like structure towards the dipole source (see Fig 5.9 (a)), starting from an arbitrary initial orientation. In particular, it uses the magnitude of the IPMC sensing signal to guide the rotation of the fish-like body. In the experiments the fish-like body was initialized at an arbitrary orientation within the range $[-45^\circ, 45^\circ]$, and the goal was to drive it towards 0°, namely, orienting towards the dipole, based on the measurement of the pressure difference sensor. Since the sensor output is a convex function of the orientation angle with the global minimum located at 0° (see Fig. 5.4), a greedy search algorithm was adopted. In particular, at each time instant, the stepper motor will move one step (corresponding to 0.9°), but the rotation direction depends on whether the previous action has led to a decrease or increase of the sensor output. Specifically,

$$U_{n+1} = sign(X_k(n) - X_k(n-1))U_n \tag{5.3}$$

where U_{n+1} is the next control for the stepper motor, while U_n is the current control at time n. $X_k(n)$ is the current magnitude of the IPMC sensing signal, while $X_k(n-1)$ is the sensing signal magnitude at the previous time step.

Fig. 5.12 shows the evolution of the sensor output magnitude during one experimental run, when the fish-like body started at 45°. It can be seen that, with the feedback from the pressure difference sensor, the body was rotated to 0° in less than 0.5 second, where the sensor output dropped to the level lower than 0.1 nA.

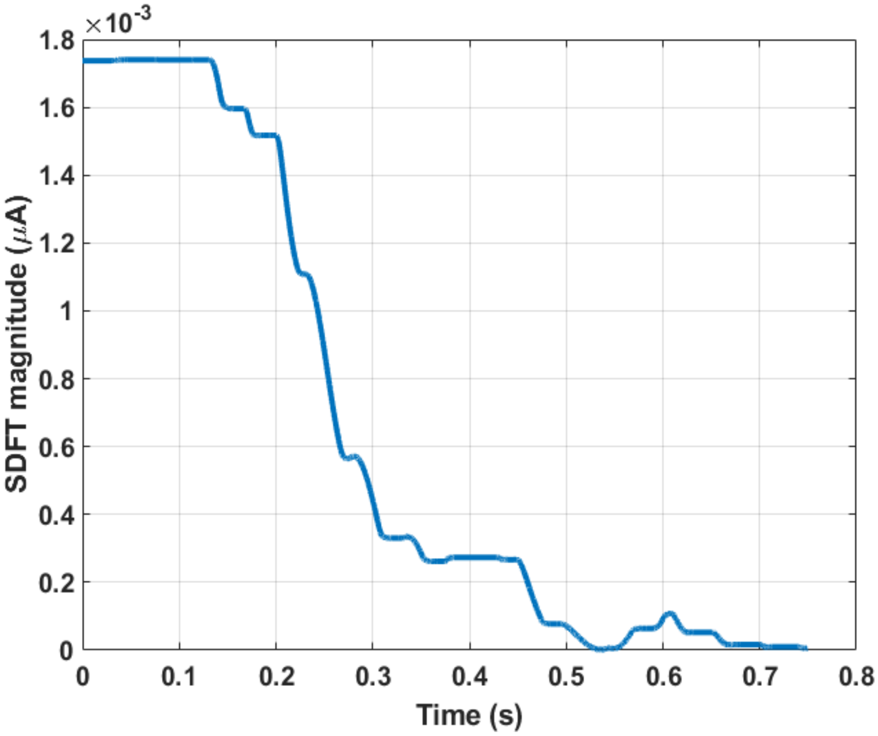

Figure 5.12: Magnitude trajectory of the IPMC sensor under the feedback control, activated at about $t = 1.3$ seconds.

Chapter 6

IPMC Flow Sensor Exploiting Self-Generated Vortices

In this chapter, we propose a novel IPMC-based flow sensing structure that exploits self-generated von Krmn vortices. A 3D-printed soft material sheath is fabricated to house the IPMC flow sensor. A key innovation of this work is the proposal of combining the direct mechanosensory property of the IPMC with the structural design of the sensor. Experimental testing in a laminar flow setting is conducted, and the collected data on mechanical vibration and IPMC sensor output are analyzed to reveal the dependence of both signal magnitudes and frequency contents on the flow speed. Specifically, it is found that the average magnitude of the IPMC current output could serve as a sensitive representation of the flow speed.

6.1 Sensor Fabrication

6.1.1 IPMC Flow Sensor Fabrication

The IPMC fabrication process follows the traditional impregnation-reduction ion-exchange process [7]. The Nafion film with a thickness of 254 microns (Nafion PFSA N 1110, DuPont) is first boiled in dilute hydrochloric acid (2 wt%) for 30 min to remove ions and impurities, and then boiled in deionized (DI) water for another 30 min to remove the acid and swell the film. After these pre-treatment steps, the Nafion film is immersed in a platinum complex solution ($[Pt(NH_3)_4]Cl_2$) for more than 4 h (usually overnight) to allow platinum ions to diffuse into the Nafion film completely through the ion-exchange process. After a rinse with DI water, the film is immersed in a water bath at 40 °C. After the temperature is raised up to 60 °C gradually, a sodium borohydride solution (5 wt% $NaBH_4$ aq) is added to the water bath as a reducing agent at a rate of 2 ml every 30 min. Once the platinum deposition is complete, those steps are repeated, from acid treatment to water-bath reduction, to deposit the platinum for the second time. The film is then cut into beam-shaped samples with the length of 20 mm and the width of 3 mm. Finally, an IPMC sensor is formed by soldering two electrical wire connectors to the IPMC platinum electrodes as shown in Fig. 6.1(a). To further ensure the sensing consistency of the IPMC sensor, an additional step of parylene encapsulation (20 μm) is conducted, followed by a water drive-in process under 70°C for three days [92].

6.1.2 Sensor Structure Fabrication

The rest of the sensor structure is 3D-printed with a multi-material printer (Objet Connex 350, Stratasys), using the soft TangoBlack material. The sensor structure, as illustrated in Fig. 6.1 (b), is printed as one piece and comprised of three parts, a cylindrical sheath (length 40 mm, outer diameter 3 mm), a solid sphere (diameter 10 mm) with a slot passing through the cylinder for housing the sensor for vortex-generation, and a solid shaft (length 30 mm, diameter 5 mm) for mounting. The IPMC sensor is inserted into the flow structure (in particular, the sheath) through the slit (length 1.5 mm, width 0.3 mm, and depth 20 mm) at the back of the sphere, as shown in Fig. 6.1 (c).

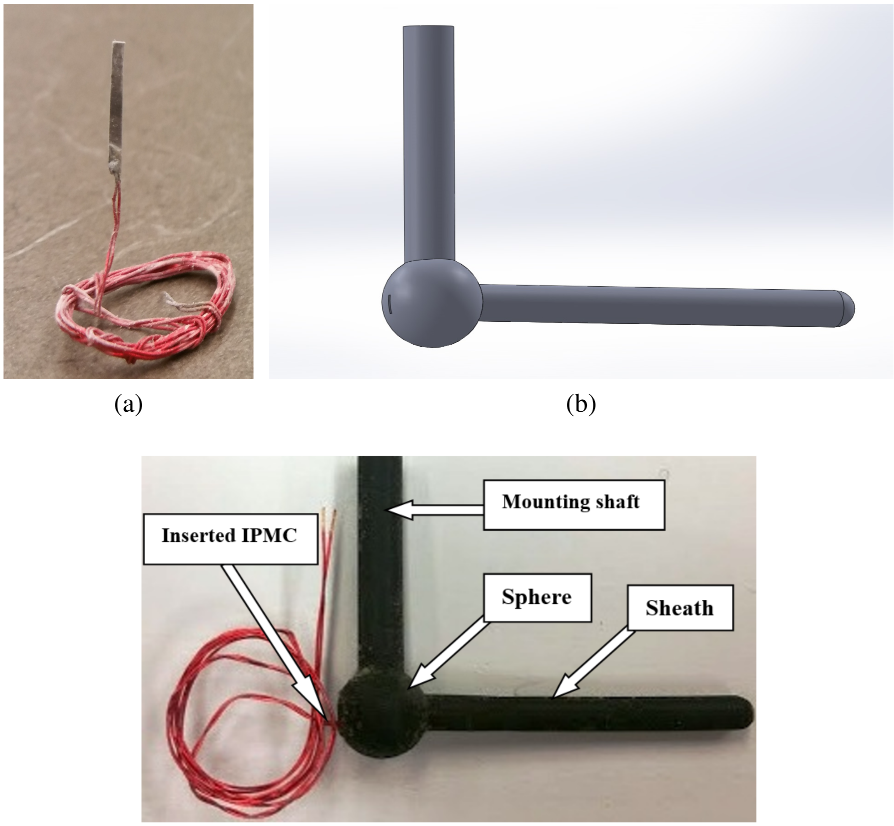

(a) (b)

(c)

Figure 6.1: Fabrication of the IPMC flow-sensing structure with self-generated vortices: (a) a parylene-encapsulated IPMC sensor; (b) design schematic of the flow-sensing structure; (c) 3D-printed structure with a sphere, a sheath, and a mounting shaft.

6.2 Experimental Results on Flow Sensing

6.2.1 Experimental Setup

A uniform flow field is generated in a swim tunnel (Loligo Systems) measuring $146 \times 68 \times 35\ \text{cm}^3$, with an enclosed test section of $65 \times 20 \times 20\ \text{cm}^3$. The flow velocity in the working section of this flow tank is controlled through adjusting the rotating speed of the motor, which is used to circulate the water in the tunnel. The sensor is mounted on the top, so that the sheath is placed 15 mm underwater and parallel to the stream flow direction. The sheath is oriented towards the downstream direction. Placing the sensor this way makes the sphere work as an obstacle in water, through which von Krmn vortices are created. These vortices in turn could induce vibrations of the cylindrical sheath, which in turn would stimulate the embedded IPMC beam. A laser displacement sensor (OADM 20I6441/S14F, Baumer Electric) is mounted outside the flow tank to measure the vibration displacement of the free end of the sheath in the horizontal plane (lateral displacement only). The mounting frame for the laser sensor is isolated from the flow tank to ensure that the displacement measurement be free from any motion disturbance caused by the tank motor. An amplification circuit and a dSPACE system are used to measure the short-circuit current generated by the IPMC sensor, and to collect and process the data, respectively.

6.2.2 Experimental Results and Discussion

Experiments are conducted for flow speeds ranging from 17.5 to 87 cm/s. Fig. 6.2 shows the measured sheath tip displacement and the corresponding IPMC sensor output (short-circuit current) when the flow speed is at 35 cm/s. From the figure, it is clear that both signals are oscillatory but not periodic. To gain additional insight into the frequency components of the signals, fast Fourier transform is conducted on the signals and Fig. 6.3 shows the the spectral content of each signal. It is interesting to note that the mechanical displacement displays a low-pass behavior while the IPMC current output displays a band-pass behavior, which is due to the additional transduction physics of IPMC.

Fig. 6.4 and Fig. 6.5 show the measured data, sheath tip displacement and IPMC current output, and their spectral contents, respectively, when the flow speed is at 70 cm/s. It can be seen that while the sensor responses at 70 cm/s are qualitatively similar to those at 35 cm/s (oscillatory and irregular), the magnitudes of both signals at the higher speed are higher, and the frequency components at 70 cm/s also shift higher. This is, to some extent, consistent with the expectation that the vortex-shedding frequency increases with the flow speed, although the collected signals encompassed a band of frequencies instead of a single frequency. To capture the sensor response quantitatively, we computed the average amplitude and average frequency of each signal, at different flow speeds, as shown in Fig. 6.6 and Fig. 6.7. Here the average amplitude is calculated by simply taking the mean of amplitudes at all frequencies, and the average frequency is calculated by amplitude-weighted mean of the frequencies. From these figures, it is evident that both average amplitude and average frequency are highly correlated with the flow speed. In particular, from the perspective of flow sensing, the average amplitude of the IPMC sensor output is able to provide a highly sensitive indication of the underlying flow speed.

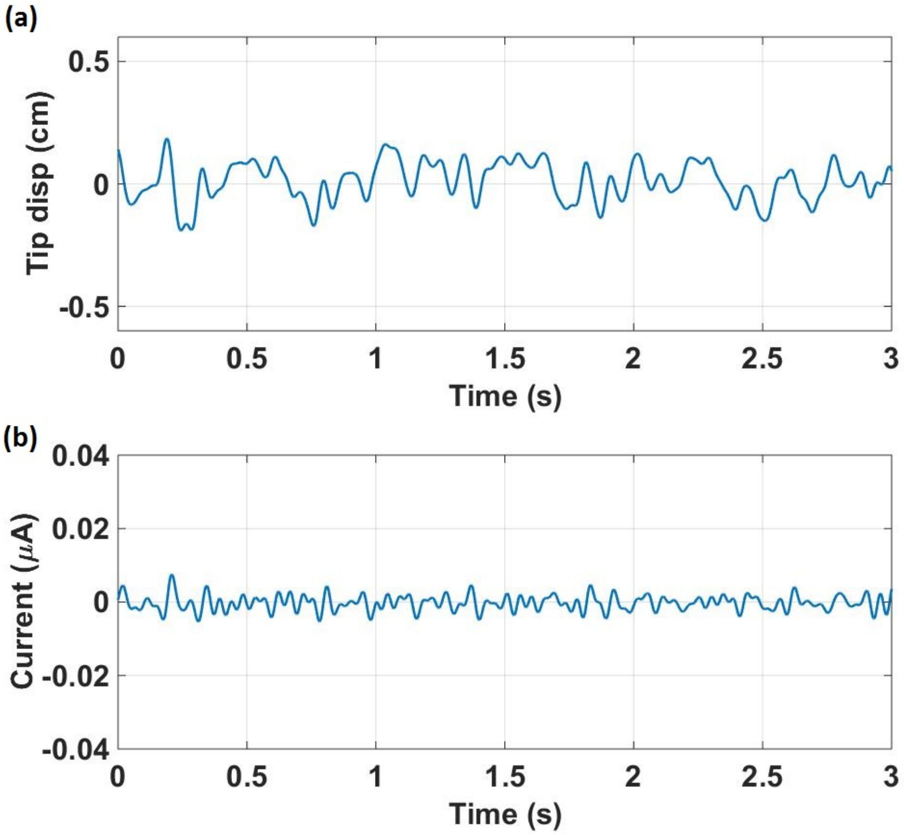

Figure 6.2: Experimental measurements of the sensor tip displacement and current output, in response to sheath laminar flow of 35 cm/s: (a) measured sheath tip displacement; (b) measured short-circuit current of the IPMC flow sensor.

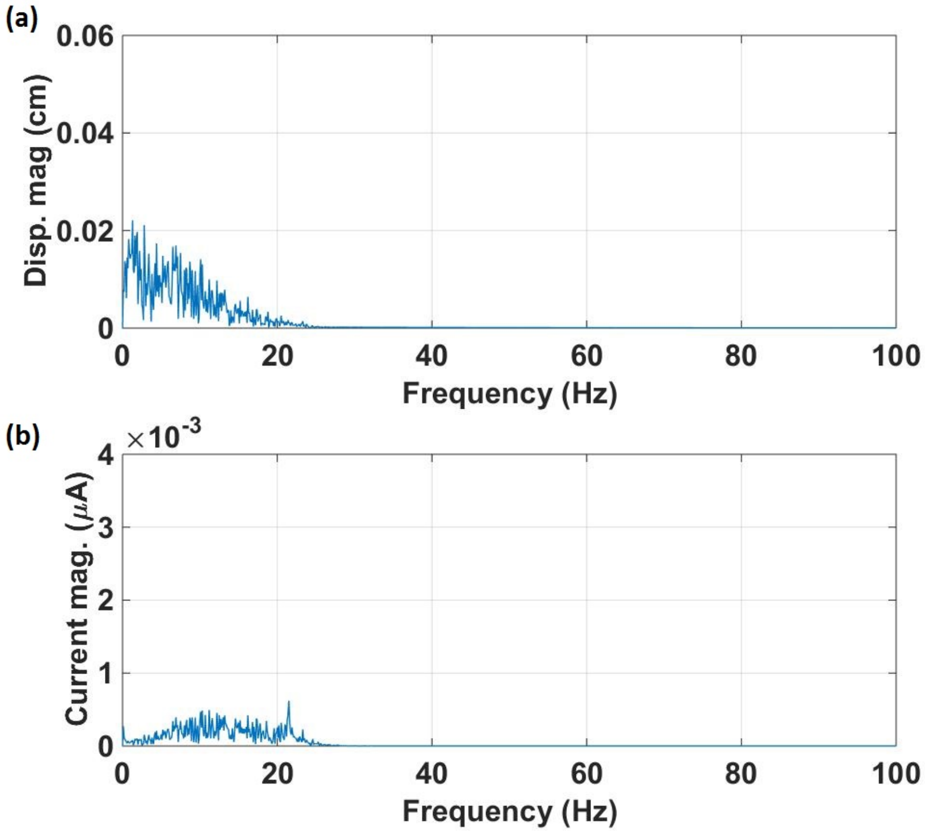

Figure 6.3: Experimental measurements of the sensor tip displacement and current output, in response to sheath laminar flow of 35 cm/s: (a) spectral content of the sheath tip displacement; (b) spectral content of the IPMC current output.

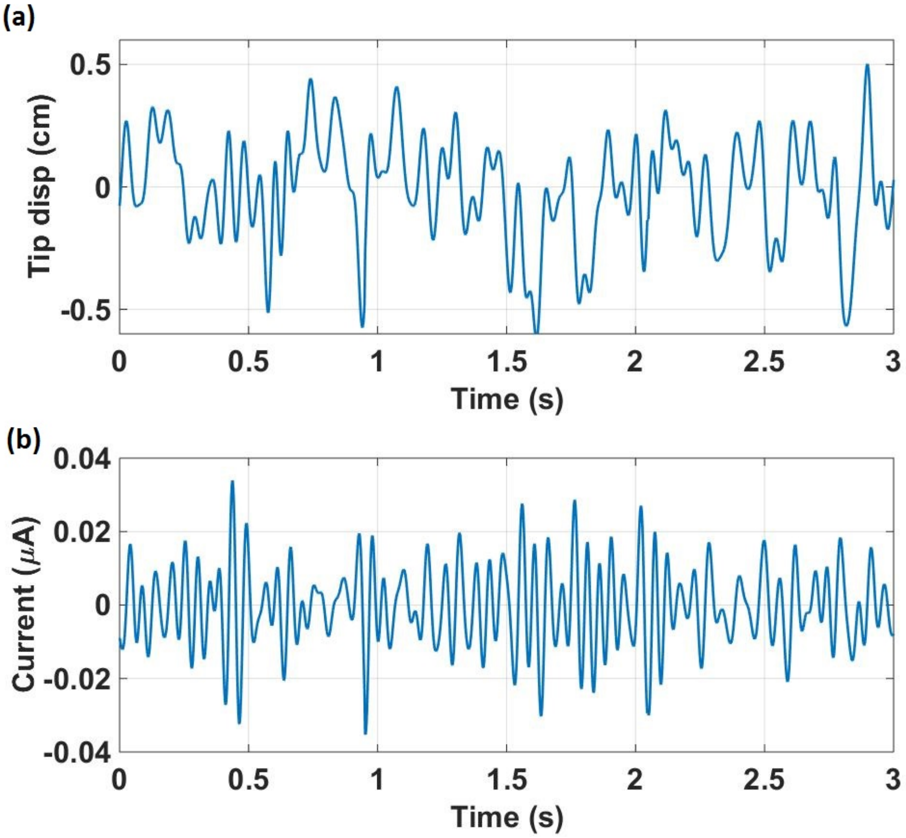

Figure 6.4: Experimental measurements of the sensor tip displacement and current output, in response to sheath laminar flow of 70 cm/s: (a) measured sheath tip displacement; (b) measured short-circuit current of the IPMC flow sensor.

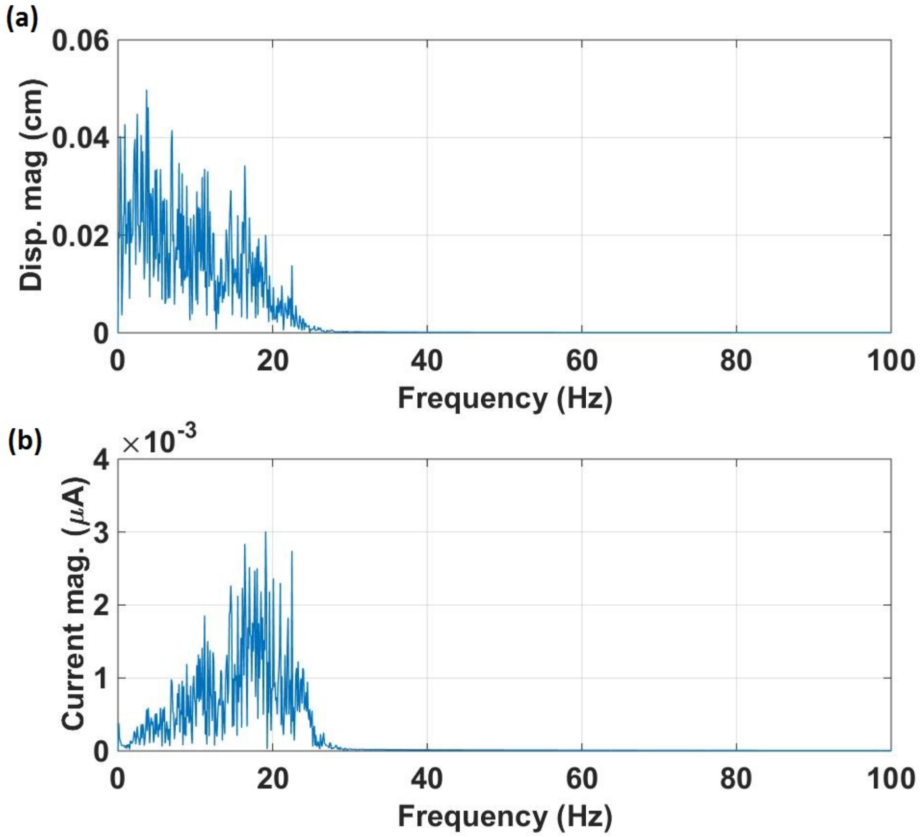

Figure 6.5: Experimental measurements of the sensor tip displacement and current output, in response to sheath laminar flow of 70 cm/s: (a) spectral content of the sheath tip displacement; (b) spectral content of the IPMC current output.

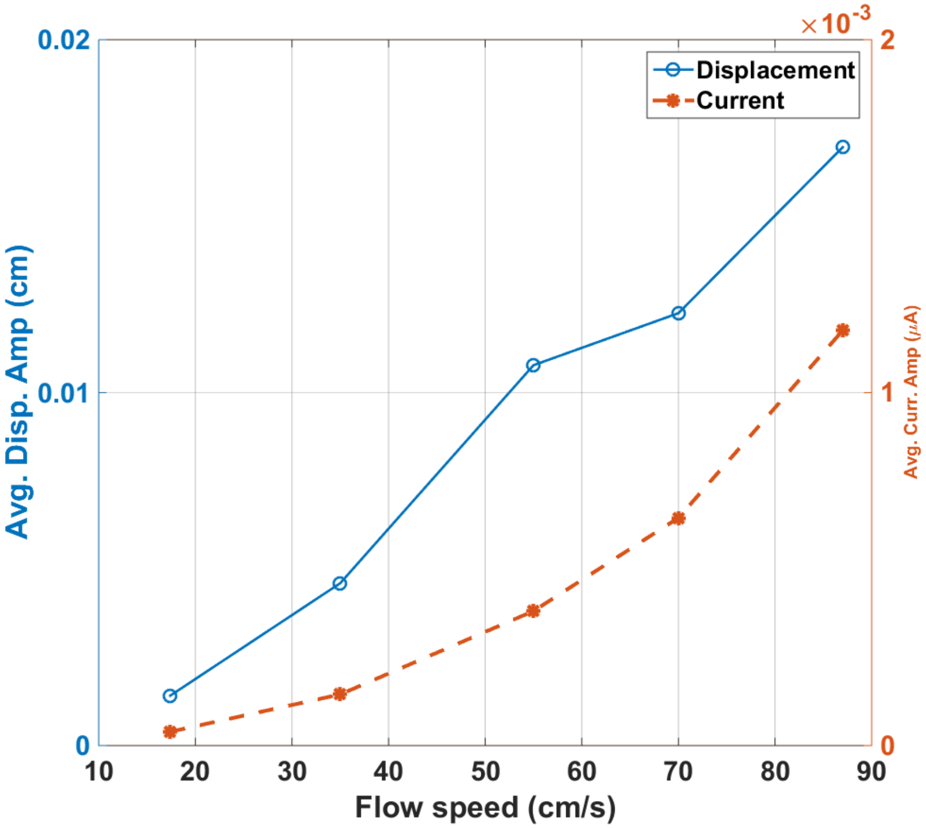

Figure 6.6: Average amplitude of the sheath displacement and the IPMC sensing signal.

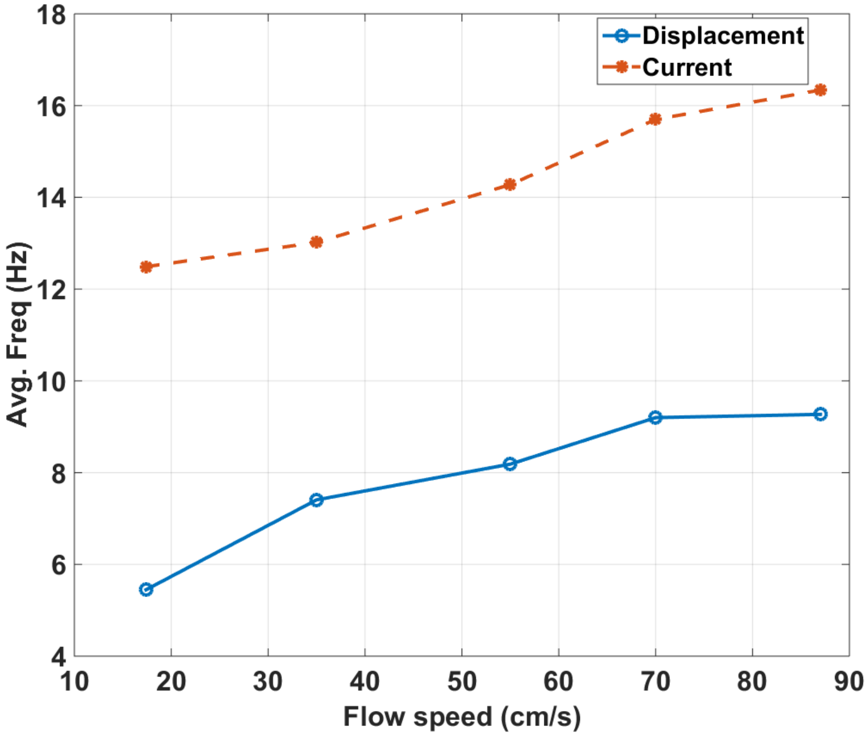

Figure 6.7: Average frequency of the sheath displacement and the IPMC sensing signal.

Chapter 7

Angular Acceleration Sensor Inspired by the Vestibular System

In this chapter, a novel angular acceleration sensor inspired by the vestibular system is investigated. Unlike the biological vestibular system, which has three semicircular canals, the proposed 3D-printed sensor is composed of one rigid circular canal, which is filled with a viscous fluid to emulate the biological equivalent. In this model, we reduce the three-dimensional sensing ability of the vestibular system to one-dimensional to gain more insight about the sensor performance. An IPMC flow sensor, embedded in a cupula and placed on the top wall of the canal, serves as an artificial hair cell sensor that produces an electrical output in response to the motion of the cupula.

Fig. 1.7 shows the schematic of the system under consideration, where one circular canal with one cupula is considered. Experiments are conducted with rotational stimuli at different accelerations. The IPMC short-circuit current output signals are collected as results of the the accelerations. It is found the sensor clearly responds to different angular acceleration at constant angular velocity. To further understand the behavior, time-dependent 3D-finite element simulation is conducted for an artificial vestibular canal under different rotational stimuli.

7.1 The Approach

7.1.1 Sensor fabrication

The artificial vestibular circular canal structure is produced with a 3D printer (Form2, Formlabs), using the clear hard Resin material. The vestibular canal structure, as illustrated in Fig. 7.1 (a), is a one-piece structure comprised of two parts: a circular canal (outer diameter 10 cm, inner diameter 3 cm), a circular canal (radius 1 cm), to house the cupula (see Fig. 7.1 (b)), and to be filled with a viscous fluid as shown in Fig. 7.1 (a). The cupula structure is 3D-printed with a multi-material printer (Objet Connex 350, Stratasys), using the soft TangoBlack material. The cupula structure, as illustrated in Fig. 7.1 (d), is printed as one piece and comprised of two parts: a cylinder (length 1 cm, radius 0.3 cm) is on top of another cylinder (length 0.3 cm, radius 0.13 cm) with a slot (length 1.3 cm, cross-section of 0.2 mm by 0.15 cm) passing through the two cylinders for housing the IPMC sensor. The IPMC fabrication process follows the traditional impregnation-reduction ion-exchange process [7, 44]. Following the IPMC fabrication, an additional step of encapsulation is conducted with a parylene coating of 20 μm, followed by a water drive-in process under 70°C for three days [92]. Finally, the IPMC sensor is inserted into the cupula structure (in particular, the slot) through the slit at the bottom of the smaller cylinder.

7.1.2 Experimental Setup

To characterize the proposed device under rotational excitation, we impose a pure angular acceleration excitation to the vestibular system device. Fig. 7.2 shows the components of the setup, including the rotational assembly that imposes a rotational stimulus on the device, the amplification circuit that amplifies and filters the sensing output, and the data acquisition system (dSPASE

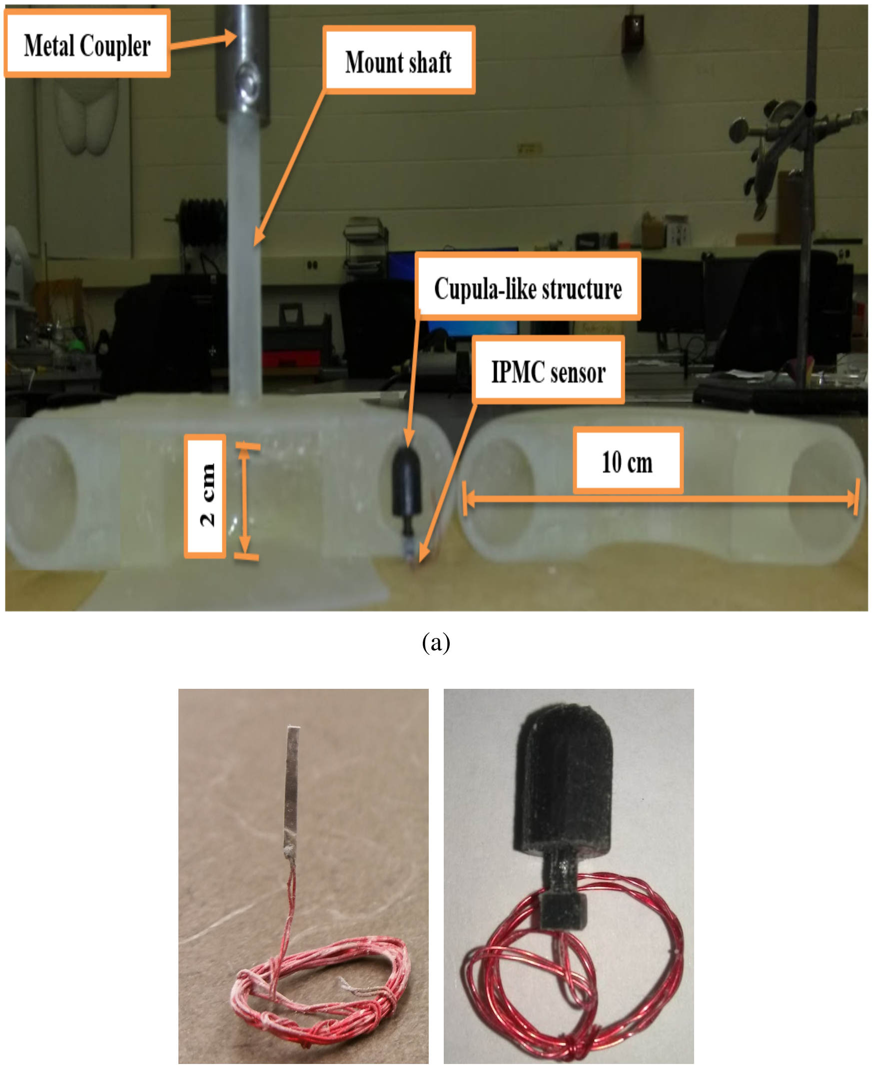

(a)

(b)

(c)

Figure 7.1: Fabrication of the proposed sensor: (a) 3D-printed vestibular system circular canal device; (c) fabricated IPMC flow sensor (1 cm long, 1 mm wide); (d) 3D-printed cupula-structure with the IPMC sensor inserted.

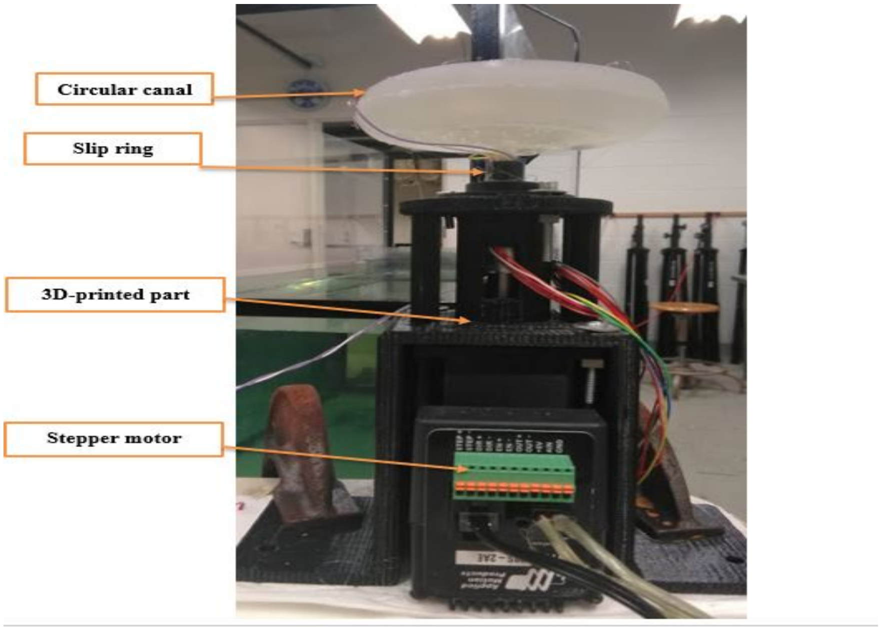

(a)

Figure 7.2: Experimental setup involving a details of the rotational assembly.

RTI 1104). The sensor device is coupled to a stepper motor (Applied motion- STM23S) through a metal coupler. The stepper motor is used to generate a programmed rotation of the sensor device. The stepper motor has a built-in shaft-encoder to better control the stepper motor trajectory.

7.1.3 Sensor Characterization

The responses of the angular acceleration sensor are characterized with a sequence of angular velocity stimuli with different angular accelerations. In particular, the angular velocity of the stepper motor first ramps up from 0 rad/s to a constant angular velocity ω to generate a constant angular acceleration a of the device, stays constant for 10 s, and then decelerates to 0 rad/s with deceleration of magnitude a. Fig. 7.3 shows an example of the stepper motor trajectory, where the constant angular velocity is 31 rad/s and the angular acceleration/deceleration is 62 rad/s^2. We note that the chosen sequence of the motor movement allows one to examine a number of sensor behaviors, in-

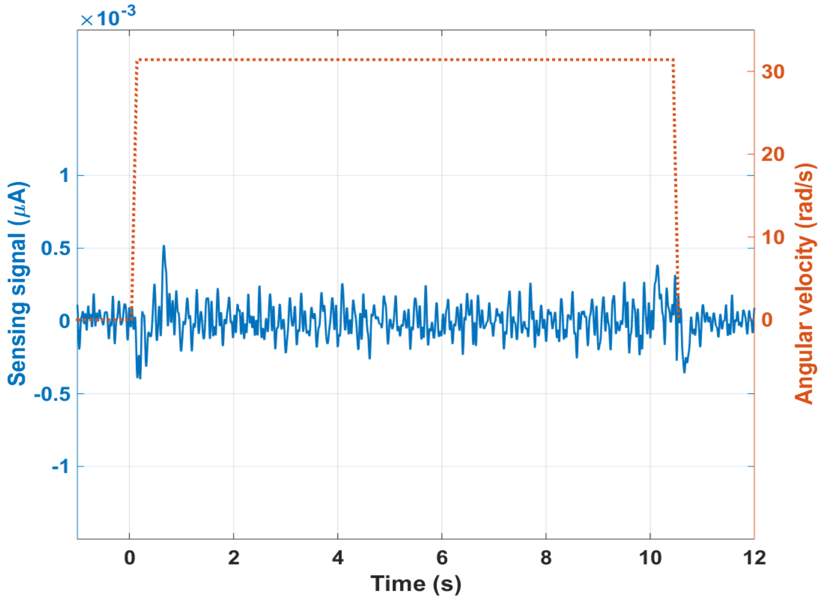

(a)

Figure 7.3: The applied sequence of the stepper motor inputs in acceleration/deceleration and the corresponding sensing signal from the IPMC. Here the constant angular velocity is 31 rad/s and the acceleration/deceleration is 62 rad/s^2.

cluding the transient and the steady state behavior (acceleration/deceleration and constant angular velocity), the IPMC sensor polarity during the acceleration/deceleration of the stimulus, and the sensing signal when the device is in the steady state.

Fig. 7.3 shows the short-circuit current output from the IPMC sensor under the corresponding input. From fig. 7.3, one can see that, during the acceleration, the sensor output produces two spikes: the fist spike happens when the acceleration starts and the second spike takes place when the motor reaches the constant angular velocity. The sensor has similar behavior during the deceleration but with opposite sensing polarity. Furthermore, when the motor is rotating with a steady-state angular velocity, the sensor produces oscillatory signals, which can be attributed to the shaking of the motor or the device during the rotational movement.

To further characterize the sensor behavior in detecting the angular acceleration, we have conducted additional experiments with a set of angular acceleration/deceleration values, which are 62 $\mathrm{rad/s^2}$, 125 $\mathrm{rad/s^2}$, 188 $\mathrm{rad/s^2}$, 251 $\mathrm{rad/s^2}$, and 314 $\mathrm{rad/s^2}$. These experiments included three scenarios. In the first scenario, the device is filled with silicone oil and its viscosity is about 5 times the viscosity of water. In the second scenario, the device is filled with water. In the third scenario, the device is free from liquid.

Fig. 7.4 and Fig. 7.5 show the sensing signal responses from the sensor under the corresponding motor trajectories. From the two figures, when the device is filled with silicon oil, no matter what is the value of the angular acceleration, it can be seen that the magnitude of the generated sensing signal increased with the angular acceleration. Compared with the case with silicone oil, the case with water shows significantly lower sensor output. This is because the viscosity of the fluid impacts the drag on the sensor. The device without liquid shows no sensing signals. Comparing the sensing results with different fluids filled, one can see that the sensitivity with silicone oil filled is over twice of that with water.

Fig. 7.6 shows the experimental results under sinusoidal rotational stimulus. At each stimulus frequency, a response of the IPMC sensor is collected. Fast Fourier transform is used to extract the amplitudes of the IPMC sensor output at each testing. From the figure, one can tell that the IPMC sensor output increase with the angular acceleration.

7.1.4 Finite Element Simulation

7.1.4.1 Fluid Structural Interaction (FSI)

The response of a superficial neuromast, biological or engineered, is due to the movement or deflection of the cupula-like structure in the presence of a flow stimulus. To capture these deflections,

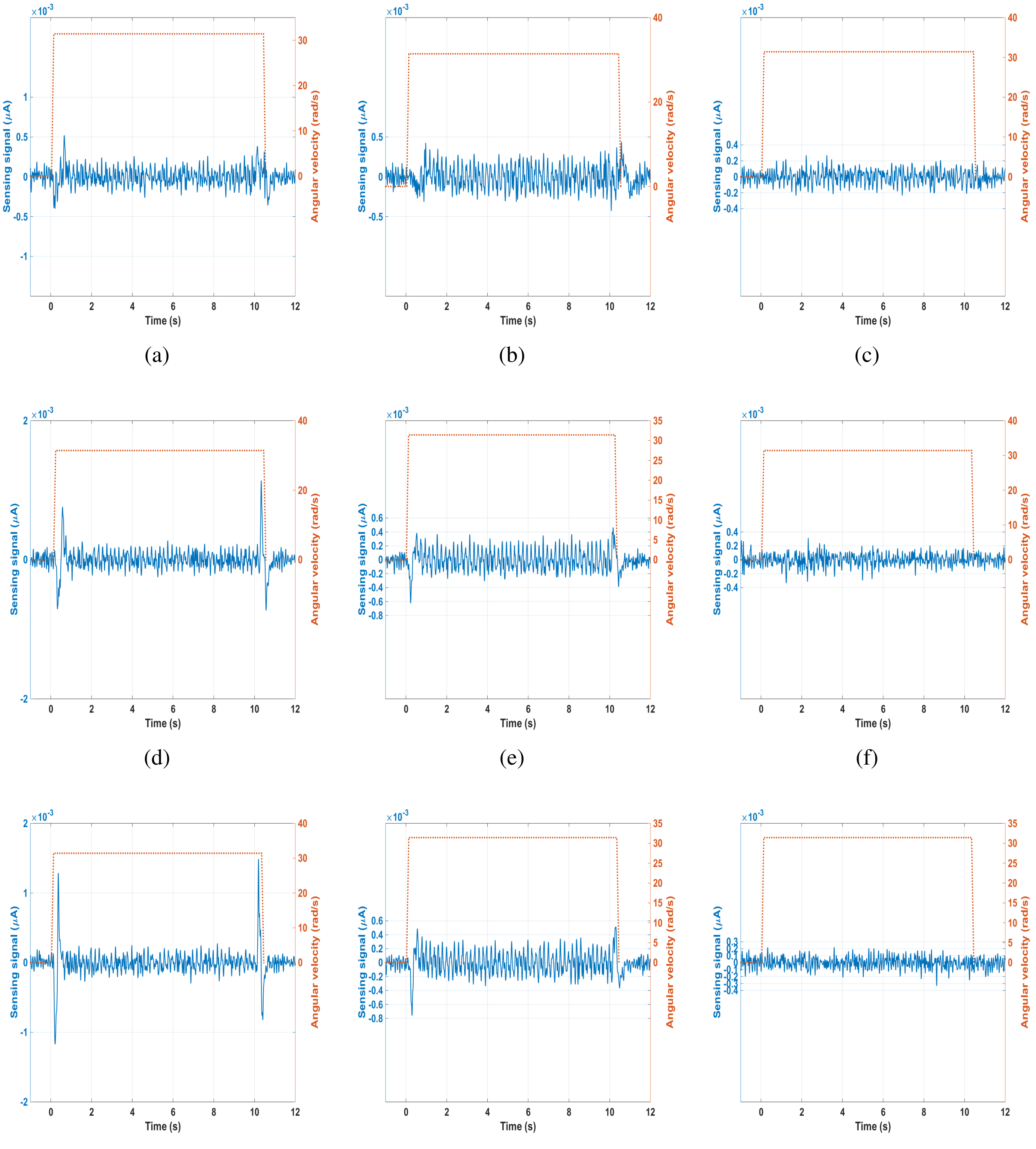

(a) (b) (c)

(d) (e) (f)

(g) (h) (i)

Figure 7.4: Experimental measurements of the sensor response under different acceleration stimuli and one angular velocity which is 31 rad/s: (a) Angular acceleration 62 rad/s^2 with viscous fluid; (b) Angular acceleration is 62 rad/s^2 with water; (c) Angular acceleration is 62 rad/s^2 with air; (d) Angular acceleration 125 rad/s^2 with viscous fluid; (e) Angular acceleration is 125 rad/s^2 with water; (f) Angular acceleration is 125 rad/s^2 with air;(g) Angular acceleration 188 rad/s^2 with viscous fluid; (h) Angular acceleration is 188 rad/s^2 with water; (i) Angular acceleration is 188 rad/s^2 with air.

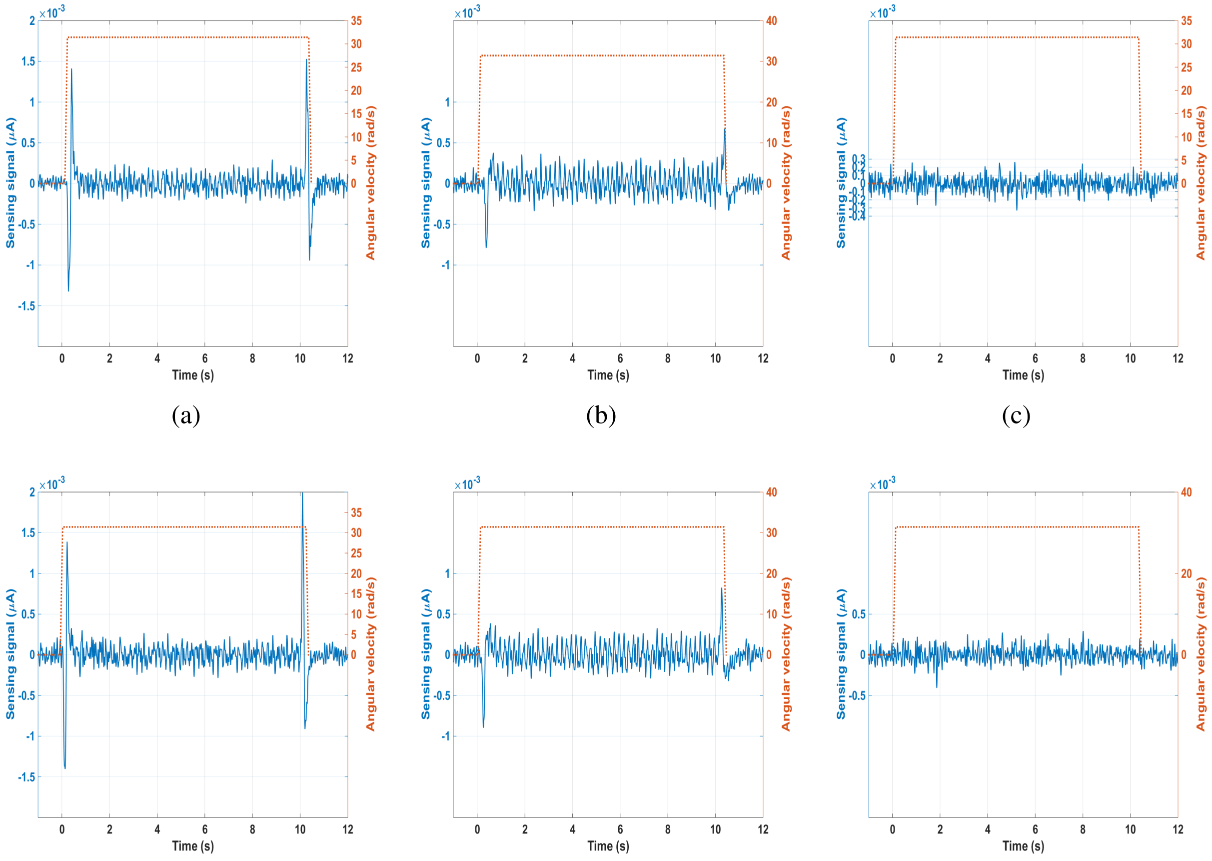

(a) (b) (c)

(d) (e) (f)

Figure 7.5: Experimental measurements of the sensor response under different acceleration stimuli and one angular velocity which is 31 rad/s: (a) Angular acceleration 251 rad/s^2 with viscous fluid; (b) Angular acceleration is 251 rad/s^2 with water; (c) Angular acceleration is 251 rad/s^2 with air; (d) Angular acceleration 314 rad/s^2 with viscous fluid; (e) Angular acceleration is 314 rad/s^2 with water; (f) Angular acceleration is 314 rad/s^2 with air.

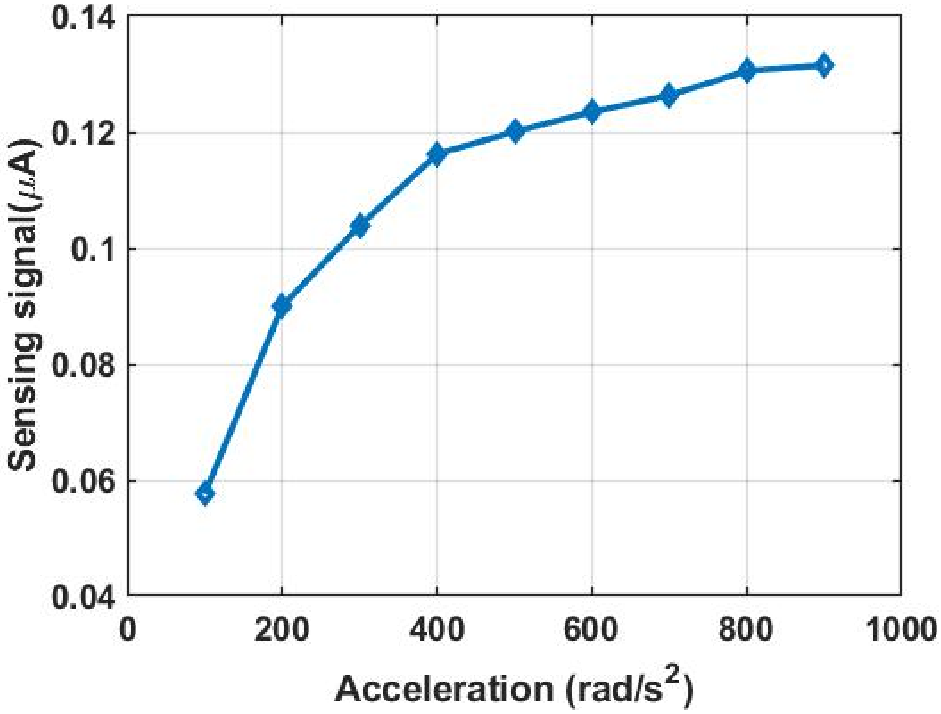

Figure 7.6: Frequency response of the IPMC sensor output under sinusoidal stimuli with different angular accelerations.

a 3D-fluid-structural interaction (FSI) module from COMSOL Multiphysics is considered. In particular, the model incorporates various material properties and dimensions, including the cupula geometry, cupula shape and size, cupula stiffness, IPMC sensor beam geometry and size. The FSI model uses the incompressible Navier-Stokes equation to describe the fluid flow and the Hooke's law to capture the linear elastic material behavior. As detailed in the next subsection, Poison-Nernst-Plank (PNP) equations are used to model the IPMC sensor response under a mechanical stimulus, which is generated by the flow-induced capula movement.

7.1.5 Modeling and Simulation Setup

In this section, the modeling of the angular acceleration sensor is modeled. The simulation setup of this sensor is done through COMSOL Multiphysics. A three-dimensional fluid-structure interaction (FSI) module from COMSOL Multiphysics is used to conduct simulation and help understand the the viscous fluid movement and the cupula structure displacement when the proposed sensor is subject to a rotational movement stimulus. The geometry and dimensions of the simulated angular acceleration device are close to those of the experimental prototype. The device has an outer radius of 5 cm, an inner radius of 3 cm, and a circular canal of 1 cm in radius. The cupula structure is comprised of two cylinders, one sitting on the other. The first one has a radius of 0.3 cm and height of 1 cm and the second one has a radius of 0.13 cm and height of 0.5 cm.

Fig. 7.7 shows the simulated configuration for the angular acceleration device, where the circular canal represents the circular canal that is filled with viscous fluid. The flexible cupula is attached from the top of the circular canal and integrated with an IPMC sensor structure. The fluid filling the canal is set to be at rest at the initial time. The device is imposed with an angular velocity with different angular acceleration rates. The angular velocity trajectories are close to those in the

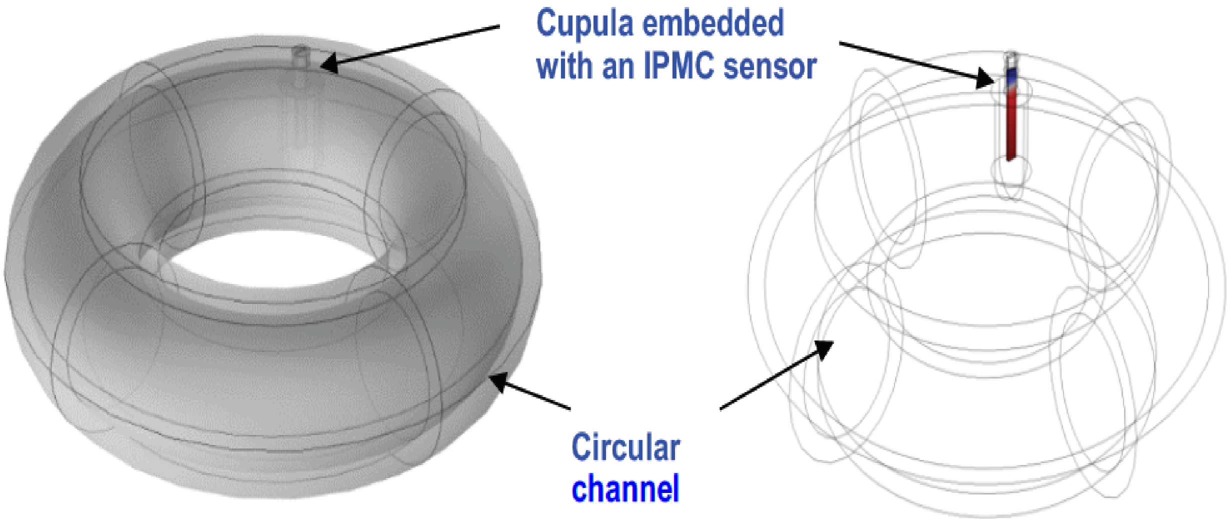

Figure 7.7: The schematic of the proposed sensor, showing a circular canal consisting of an IPMC sensor embedded in cupula-like structure.

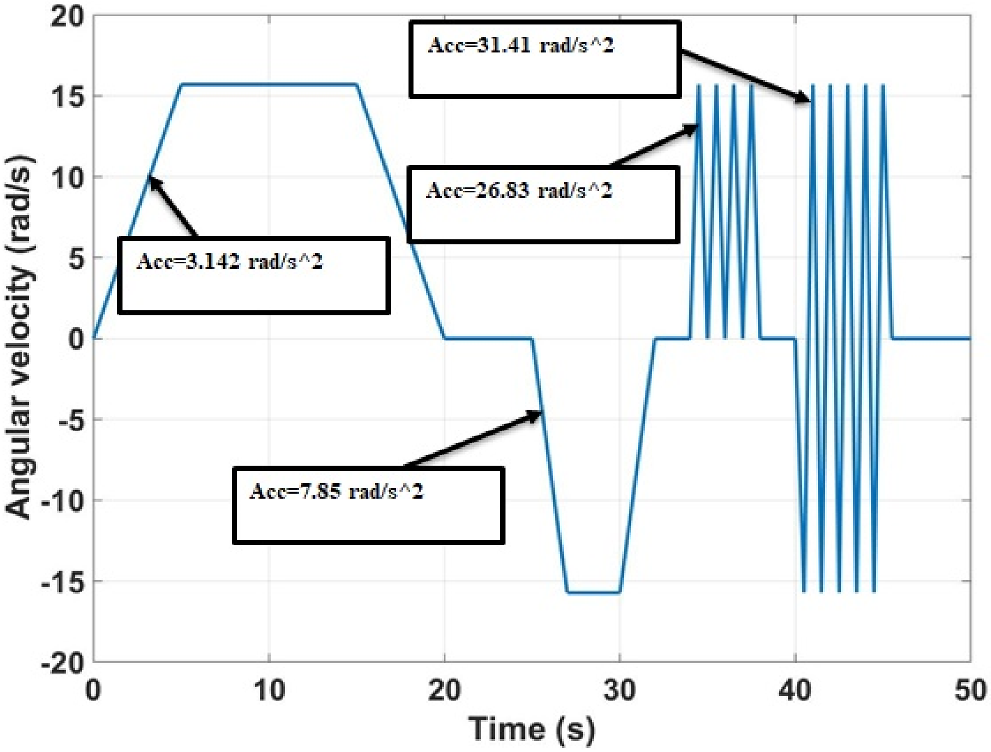

Figure 7.8: The schematic of the proposed sensor, showing a circular canal consisting of an IPMC sensor embedded in cupula-like structure.

experiments. Fig. 7.8 presents a the trajectory of the angular velocity with different rates of angular accelerations.

7.1.6 Simulation Results

The angular movement of the circular canal creates an angular movement of the fluid inside the canal, which in turn provides a stimulus to the cupula structure. Fig. 7.9 shows the IPMC tip displacement responses when the canal is subjected to one angular velocity and different rates of accelerations. From the figure, it can be seen that the IPMC has a clear displacement when there is a change in the angular velocity which means that there is a constant angular acceleration. The cupula-inspired IPMC sensor does not show a displacement when the angular acceleration is zero. From that, the fluid-filled the canal acts as a rigid body in the constant angular velocity, leading

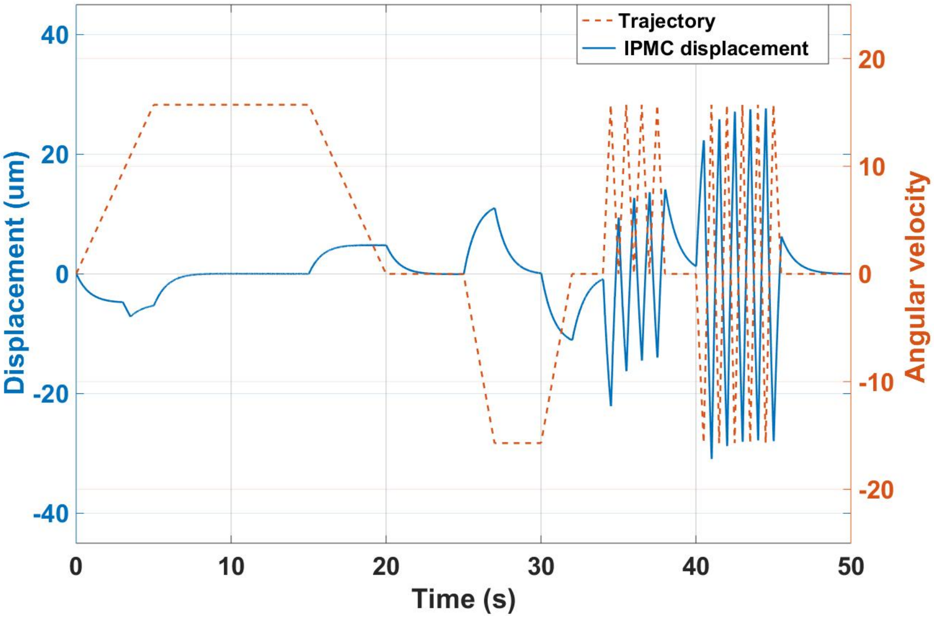

Figure 7.9: The input trajectory to the circular canal with the correspondence sensor displacements.

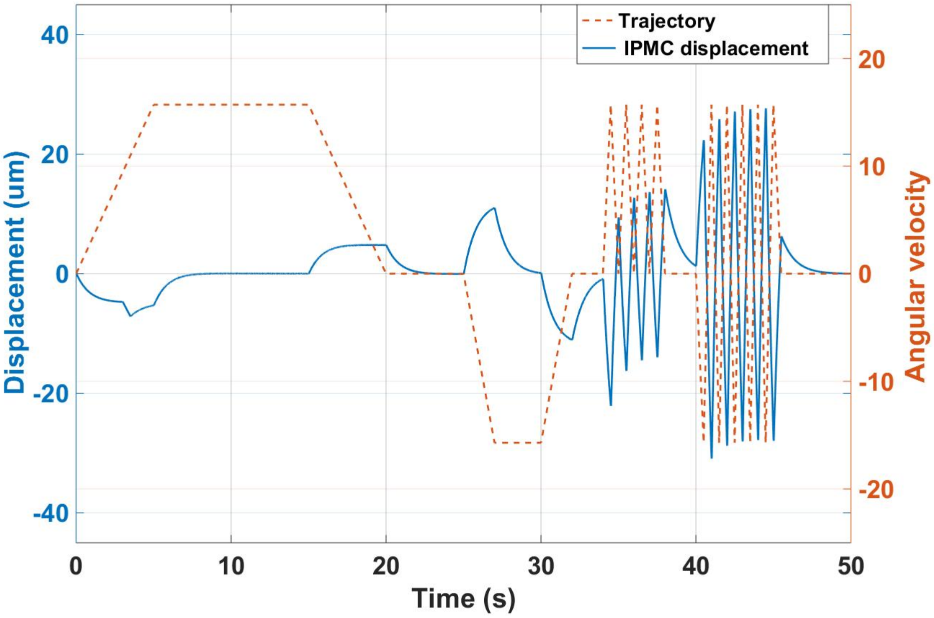

Figure 7.10: The IPMC sensor tip displacement and the IPMC sensor output (short circuit current).

to the whole body (canal, cupula-inspired IPMC sensor, and the fluid) rotating as a single object, which in turn lead to no displacement of the cupula. Fig. 7.10 further shows the tip displacement amplitude of the IPMC structure and the corresponding IPMC sensing signal.

7.2 Comparison between Experimental Measurements and Simulation Results

It can be noted that the displacement magnitude of the IPMC tip shows a behavior that is consistent with the IPMC sensor output observed in experiments (Fig. 7.4 and Fig. 7.5), which suggests that finite-element simulation could be used as an instrumental tool for further understanding and optimization of the canal sensor device. Fig. 7.11 shows the comparison between the measured sensor outputs and the finite-element model (FEM) sensor outputs under one angular velocity with different angular acceleration stimuli. Overall, the figure shows good agreement between the measurement and FEM. We used the Young's modulus of the cupula and diffusion constant of the IPMC sensor to fit the model. Specifically, the FEM is able to capture the magnitude and the polarity of the sensor response. For example, the polarity of the sensing signal is determined only by the acceleration or deceleration trend of the stimulus.

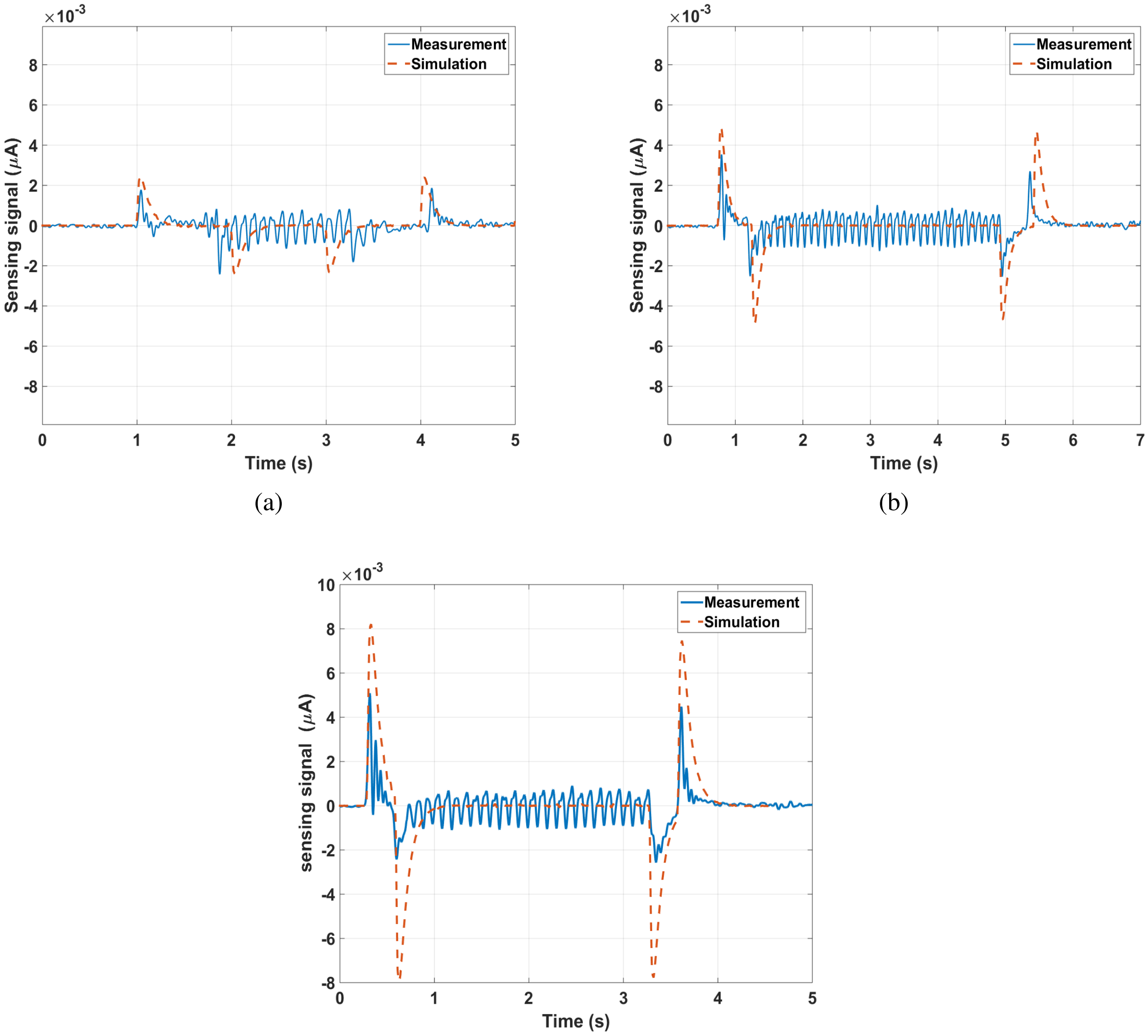

(a)

(b)

(c)

Figure 7.11: Comparison between the FE model and the experimental measurements of the sensor response under different acceleration stimuli and one angular velocity which is 16 rad/s: (a) Angular acceleration 15.6 rad/s^2 with viscous fluid; (b) Angular acceleration is 31.2 rad/s^2 with viscous fluid; (c) Angular acceleration is 40.3 rad/s^2 with viscous fluid.

Chapter 8

Conclusions and Future Work

8.1 Conclusion

We reported a new physics-based model for a tubular IPMC sensor subjected to a torsional load. The model was built upon the Poisson-Nernst-Planck (PNP) equations for capturing the movement of cations. A key innovation of this work was the proposal of relating the shear strains to the local anion concentration. An experimental setup was created for applying twist at one end of the IPMC tube while keeping the other end fixed. Experiments involving stimuli of different magnitudes, loading orientations, and loading/unloading speeds were conducted, and the proposed model was shown to be able to capture the trends observed experimentally.

Inspired by the lateral line system of the fish, we explored the sensitivity of the IPMC-based artificial superficial and canal neuromasts based on their dimensions, shapes, and cupula stiffness. For the canal-type lateral line system, modeling, fabrication, and experimental testing of were investigated. Instead of water, the canal was filled with a viscous fluid to emulate the biological canals. The IPMC sensor physics was coupled to the FSI module for the cupula, allowing the computation of the sensor output in the presence of a dipole flow. The fabrication process of the IPMC flow sensor and cupula-like structure were described in detail. Experimental testing in a dipole flow was conducted to explore the canal performance. Simulation was conducted to examine the effects of cupula size and stiffness on its displacement under a dipole stimulus. In particular, the computation results from the finite-element model were compared with those predicted by an analytical model to explore the valid regimes of the analytical model. Such comparisons yielded useful insight as to when to use the analytical model for quick exploration of the design space, and when to resort to the finite element model for higher-fidelity predictions. By using the later finite element model, we have modeled the superficial lateral line and compared the simulation results with an analytical model to have connection with the engineering counterpart.

we presented the fabrication, experimental testing, and simulation of a fish canal lateral line-inspired pressure difference sensor and illustrated its use in underwater applications via a feedback control experiment. The sensor consisted of a 3D-printed rigid semicircular channel and a 3D-printed soft cupula, which housed an IPMC sensor that served as a hair cell. Experimental testing in a dipole flow was conducted to explore performance of the sensor, and the collected data on the IPMC sensor output was analyzed. The experimental results confirmed that the sensor was able to effectively capture the pressure difference between the pores. Finite-element simulation, with parameters identified using experimental data, was conducted to capture the fluid-structure interactions within the proposed sensor. It was found that the simulated displacement of the cupula structure demonstrated similar behavior as observed in the experimental sensor output, when the sensor was oriented at different angles relative to the dipole source. A sliding discrete Fourier transform (SDFT) algorithm was used to effectively compute the IPMC sensor magnitude, which enabled real-time feedback control of the orientation of the fish-like body.

We presented a new IPMC-based flow sensing structure that exploits self-generated von Krmn vortices. A 3D-printed soft material sheath was fabricated to house the IPMC flow sensor. A key innovation of this work was the proposal of combining the direct mechanosensory property of the IPMC with the structural design of the sensor. Experimental testing in a laminar flow setting was conducted, and the collected data on mechanical vibration and IPMC sensor output were analyzed to reveal the dependence of both signal magnitudes and frequency contents on the flow speed. Specifically, it is found that the average magnitude of the IPMC current output could serve as a sensitive representation of the flow speed.

Finally, we reported the fabrication, experimental characterization and the simulation of a novel angular accelerometer inspired by the vestibular system. The sensor consist of a 3D-printed rigid torus canal and a 3D-printed soft cupula, which housing an IPMC sensor that served as a hair cell. Experimental characterization with a rotational movement stimuli was conducted to explore the performance of the angular sensor, and the collected data on the IPMC sensor was recorded. The experimental results confirmed that the sensor was able to capture the angular acceleration of the rigid body, and provided evidence that the fluid-filled the canal play a key role in the sensor performance. Finite-element simulations were conducted to capture the fluid structure interaction between the cupula-inspired IPMC sensor and the fluid-filled the canal and to gain more insights about the behavior of the angular acceleration device.

8.2 Future Work

First, in the study of the artificial lateral line system, further simulation results will be collected to conduct non-dimensionalized analysis on the sensitivity. Experiments will be designed to characterize the sensing response of the IPMC flow sensor for both types (superficial and canal) of lateral lines.

Second, in the study of the bio-inspired pressure gradient sensor, a finite-element simulation can be conducted, where IPMC physics is explicitly incorporated. Model parameters can obtained from experimental data, so that the model captures the physical device with high fidelity. Such a model will be used to optimize the geometry and materials of different parts of the device (the U-channel, cupula, etc) as well as the viscosity of the canal fluid.

Third, for the flow sensor using self-generated vortices's, a finite-element modeling capturing the fluid-structure interactions and the IPMC physics will also be instrumental to further understand the experimentally observed phenomena. Such a model can also be used to optimize the geometry and material properties of the flow sensor structure. Real-time algorithms for processing the IPMC output can be developed to predict the flow speed.

BIBLIOGRAPHY

BIBLIOGRAPHY

[1] C. Von Campenhausen, I. Riess, and R. Weissert, “Detection of stationary objects by the blind cave fishanoptichthys jordani (characidae),” *Journal of Comparative Physiology*, vol. 143, no. 3, pp. 369–374, 1981.

[2] T. Stalbaum, D. Pugal, S. E. Nelson, V. Palmre, and K. J. Kim, “Physics-based modeling of mechano-electric transduction of tube-shaped ionic polymer-metal composite,” *Journal of Applied Physics*, vol. 117, no. 11, p. 114903, 2015.

[3] Y. Bar-Cohen, *Electroactive polymer (EAP) Actuators as Artificial Muscles: Reality, potential, and Challenges*. SPIE press, 2004, vol. 136.

[4] M. Shahinpoor and K. Kim, “Ionic polymer-metal composites: I. Fundamentals,” *Smart Materials and Structures*, vol. 10, pp. 819–833, 2001.

[5] M. ul Haq and Z. Gang, “A comprehensive review on ionic polymer metal composite applications,” *Emerging Materials Research*, vol. 5, no. 1, 2016, DOI:10.1680/jemmr.15.00026.

[6] D. Pugal, K. Jung, A. Aabloo, and K. J. Kim, “Ionic polymer–metal composite mechano-electrical transduction: review and perspectives,” *Polymer international*, vol. 59, no. 3, pp. 279–289, 2010.

[7] K. J. Kim and M. Shahinpoor, “Ionic polymer-metal composites: II. manufacturing techniques,” *Smart Materials and Structures*, vol. 15, pp. 65–79, 2003.

[8] L. N. Hao, Y. Chen, and Y. S. Zhao, “Research on enhanced performance of ionic polymer metal composite by multiwalled carbon nanotubes,” *Materials Research Innovation*, vol. 19, no. 1, pp. 477–481, 2015.

[9] H. Lei, W. Li, G. Zhu, and X. Tan, “Evaluation of encapsulated IPMC sensor based on thick parylene coating,” ser. Proceedings of ASME 2012 Conference on Smart Materials, Adaptive Structures and Intelligent Systems. Stone Mountain, GA: ASME, 2012, pp. SMASIS2012–7975.

[10] S. Sareh, J. Rossiter, A. Conn, K. Drescher, and R. E. Goldstein, “Swimming like algae: biomimetic soft artificial cilia,” *Journal of the Royal Society Interface*, vol. 100, no. 78, p. 20120666, 2013.

[11] B. Sivasubramanian and D. Kim, “Development, analysis, and comparison of electromechanical properties of buckypaper IPMC actuator,” in *Electroactive Polymer Actuators and Devices (EAPAD) XIV*, ser. Proceedings of SPIE, Y. Bar-Cohen, Ed., vol. 9056. Bellingham, WA: SPIE, 2014, p. 2045287.

[12] M. Shahinpoor, Y. Bar-Cohen, J. Simpson, and J. Smith, “Ionic polymer-metal composites (IPMCs) as biomimetic sensors, actuators and artificial muscles - a review,” *Smart Materials and Structures*, vol. 7, no. 6, pp. R15–R30, 1998.

[13] M. Shahinpoor and M. Mojarrad, “Ionic polymer sensors and actuators,” US patent, US Patent Office, No. 6475639, November 5 2002.

[14] V. Palmre, D. Pugal, K. J. Kim, K. K. Leang, K. Asaka, and A. Aabloo, “Nanothorn electrodes for ionic polymer-metal composite artificial muscles,” *Scientific Reports*, vol. 4, p. 6176, 2014.

[15] Y. Cha, M. Aureli, and M. Porfiri, “A physics-based model of the electrical impedance of ionic polymer metal composites,” *Journal of Applied Physics*, vol. 111, no. 2, p. 124901, 2012.

[16] H. Lei, C. Lim, and X. Tan, “Humidity-dependence of IPMC sensing dynamics: Characterization and modeling from a physical perspective,” *Meccanica*, vol. 50, no. 11, pp. 2663–2673, 2015.

[17] Z. Sun, L. Hao, W. Chen, Z. Li, and L. Liu, “A novel discrete adaptive sliding-mode-like control method for ionic polymer-metal composite manipulators,” *Smart Materials and Structures*, vol. 22, no. 9, p. 095027, 2013.

[18] H. Lei, C. Lim, and X. Tan, “Modeling and inverse compensation of dynamics of base-excited ionic polymer-metal composite sensors,” *Journal of Intelligent Material Systems and Structures*, vol. 24, no. 13, pp. 1557–1571, 2013.

[19] Y. Xiong, Y. Chen, Z. Sun, L. Hao, and J. Dong, “Active disturbance rejection control for output force creep characteristics of ionic polymer metal composites,” *Smart Materials and Structures*, vol. 23, no. 7, p. 075014, 2014.

[20] M. Aureli and M. Porfiri, “Nonlinear sensing of ionic polymer metal composites,” *Continuum Mechanics and Thermodynamics*, vol. 25, no. 2, pp. 273–310, 2013.

[21] L. Hao and Z. Li, "Modeling and adaptive inverse control of hysteresis and creep in ionic polymer-metal composite actuators," *Smart Materials and Structures*, vol. 19, no. 2, p. 025014, 2010.

[22] K. Farinholt and D. J. Leo, "Modeling of electromechanical charge sensing in ionic polymer transducers," *Mechanics of Materials*, vol. 36, no. 5, pp. 421–433, 2004.

[23] R. Dong and Y. Tan, "A model based predictive compensation for ionic polymer metal composite sensors for displacement measurement," *Sensors and Actuators A: Physical*, vol. 224, no. 1, pp. 43–49, 2015.

[24] U. Zangrilli and L. Weiland, "Prediction of the ionic polymer transducer sensing of shear loading," *Smart Materials and Structures*, vol. 20, no. 9, p. 094013, 2011.

[25] Y. Bahramzadeh and M. Shahinpoor, "Dynamic curvature sensing employing ionic-polymer-metal composite sensors," *Smart Materials and Structures*, vol. 20, p. 094011, 2011.

[26] F. Cellini, C. Intartaglia, L. Soria, and M. Porfiri, "Effect of hydrodynamic interaction on energy harvesting in arrays of ionic polymer metal composites vibrating in a viscous fluid," *Smart Materials and Structures*, vol. 23, no. 4, p. 045015, 2014.

[27] Y. Cha, M.Verotti, H. Walcott, S. D. Peterson, and M. Porfiri, "Energy harvesting from the tail beating of a carangiform swimmer using ionic polymer metal composites," *Bioinspiration & Biomimetics*, vol. 8, no. 3, p. 036003, 2013.

[28] Y. Cha, L. Shen, and M. Porfiri, "Energy harvesting from underwater torsional vibrations of a patterned ionic polymer metal composite," *Smart Materials and Structures*, vol. 22, no. 5, p. 055027, 2013.

[29] S. D. Peterson and M. Porfiri, "Energy exchange between a vortex ring and an ionic polymer metal composite," *Applied Physics Letters*, vol. 100, no. 11, p. 114102, 2012.

[30] H. Lei, W. Li, and X. Tan, "Microfabrication of IPMC cilia for bio-inspired flow sensing," in *Electroactive Polymer Actuators and Devices (EAPAD) XIV*, ser. Proceedings of SPIE, Y. Bar-Cohen, Ed., vol. 8340. Bellingham, WA: SPIE, 2012, p. 83401A.

[31] ——, "Encapsulation of ionic polymer-metal composite (IPMC) sensors with thick parylene: Fabrication process and characterization results," *Sensors and Actuators A: Physical*, vol. 217, pp. 1–12, 2014.

[32] J. D. Carrico, N. W. Traeden, M. Aureli, and K. K. Leang, “Fused filament 3d printing of ionic polymer-metal composites (IPMCs),” *Smart Materials and Structures*, vol. 24, no. 12, p. 125021, 2015.

[33] J. D. Carrico and K. K. Leang, “Fused filament 3d printing of ionic polymer-metal composites for soft robotics,” in *Electroactive Polymer Actuators and Devices (EAPAD) 2017*, vol. 10163. International Society for Optics and Photonics, 2017, p. 101630I.

[34] L. DeVries, F. D. Lagor, H. Lei, X. Tan, and D. A. Paley, “Distributed flow estimation and closed-loop control of an underwater vehicle with a multi-modal artificial lateral line,” *Bioinspiration & Biomimetics*, vol. 10, no. 2, p. 025002, 2015.

[35] F. Zhang, F. D. Lagor, H. Lei, X. Tan, and D. A. Paley, “Robotic fish: flow-relative control behaviors using distributed flow sensing,” *Mechanical Engineering*, vol. 138, no. 3, p. S2, 2016.

[36] A. Ahrari, H. Lei, M. A. Sharif, K. Deb, and X. Tan, “Design optimization of an artificial lateral line system incorporating flow and sensor uncertainties,” *Engineering Optimization*, vol. 49, no. 2, pp. 328–344, 2017.

[37] ——, “Reliable underwater dipole source characterization in 3d space by an optimally designed artificial lateral line system,” *Bioinspiration & biomimetics*, vol. 12, no. 3, p. 036010, 2017.

[38] H. Lei, M. A. Sharif, D. A. Paley, M. J. McHenry, and X. Tan, “Performance improvement of IPMC flow sensors with a biologically-inspired cupula structure,” in *Electroactive Polymer Actuators and Devices (EAPAD) 2016*, vol. 9798. International Society for Optics and Photonics, 2016, p. 979827.

[39] K. Oguro, N. Fujiwara, K. Asaka, K. Onishi, and S. Sewa, “Polymer electrolyte actuator with gold electrodes,” in *Electroactive Polymer Actuators and Devices (EAPAD) XIV*, ser. Proceedings of SPIE, Y. Bar-Cohen, Ed., vol. 3669. Bellingham, WA: SPIE, 1999, pp. 3669–39.

[40] S. J. Kim, D. Pugal, J. Wong, K. J. Kim, and W. Yim, “A bio-inspired multi degree of freedom actuator based on a novel cylindrical ionic polymer-metal composite material,” *Robotics and Autonomous Systems*, vol. 62, no. 1, pp. 53–60, 2014.

[41] H. Lei and X. Tan, “Fabrication and characterization of a two-dimensional IPMC sensor,” in *Electroactive Polymer Actuators and Devices (EAPAD)*, ser. Proceedings of SPIE, Y. Bar-Cohen, Ed., vol. 8687. San Diego, CA: SPIE, 2013, p. 868707.

[42] L. Shen, Y. Cha, A. Shams, and M. Porfiri, "Fabrication and buckling analysis of ionic polymer metal composite pipes," *Smart Materials and Structures*, vol. 22, no. 10, p. 105032, 2013.

[43] H. Lei and X. Tan, "A novel tubular thin-wall IPMC sensor capable of two-dimensional sensing: Fabrication, characterization and modeling," ser. Proceedings of ASME 2014 Conference on Smart Materials, Adaptive Structures and Intelligent Systems. Newport, RI: ASME, 2014, pp. SMASIS2014–7594.

[44] H. Lei, M. A. Sharif, and X. Tan, "Dynamics of omnidirectional IPMC sensor: Experimental characterization and physical modeling," *IEEE/ASME Transactions on Mechatronics*, vol. 21, no. 2, pp. 601–612, 2016.

[45] ——, "A dynamic physics-based model for tubular IPMC sensors under torsional excitation," in *Electroactive Polymer Actuators and Devices (EAPAD) 2016, ser. Proceedings of SPIE, Y. Bar-Cohen, Ed., vol. 9798,.* International Society for Optics and Photonics, 2016, p. 979836.

[46] T. J. Pitcher, B. L. Partridge, and C. Wardle, "A blind fish can school," *Science*, vol. 194, no. 4268, pp. 963–965, 1976.

[47] R. Weissert and C. Von Campenhausen, "Discrimination between stationary objects by the blind cave fishanoptichthys jordani (characidae)," *Journal of comparative physiology*, vol. 143, no. 3, pp. 375–381, 1981.

[48] S. Coombs, J. Janssen, and J. C. Webb, "Diversity of lateral line systems: evolutionary and functional considerations," in *Sensory Biology of Aquatic Animals*, J. Atema, R. R. Fay, A. N. Popper, and W. N. Tavolga, Eds. New York, US: Springer, 1988, ch. 22, pp. 553–593.

[49] J. Engelmann, W. Hanke, J. Mogdans, and H. Bleckmann, "Hydrodynamic stimuli and the fish lateral line," *Nature*, vol. 408, no. 6808, pp. 51–52, 2000.

[50] C. Barbier and J. A. Humphrey, "Drag force acting on a neuromast in the fish lateral line trunk canal.i. numerical modelling of external–internal flow coupling," *Journal of The Royal Society Interface*, vol. 6, no. 36, pp. 627–640, 2009.

[51] H. Bleckmann, "Peripheral and central processing of lateral line information," *Journal of Comparative Physiology A*, vol. 194, no. 2, pp. 145–158, 2008.

[52] S. Coombs, "Smart skins: information processing by lateral line flow sensors," *Autonomous Robots*, vol. 11, no. 3, pp. 255–261, 2001.

[53] A. Ahrari, H. Lei, M. A. Sharif, K. Deb, and X. Tan, “Optimum design of artificial lateral line systems for object tracking under uncertain conditions,” in *Proceedings of the 2016 on Genetic and Evolutionary Computation Conference Companion*. ACM, 2016, pp. 123–124.

[54] C. Liu, “Micromachined biomimetic artificial haircell sensors,” *Bioinspiration & Biomimetics*, vol. 2, no. 4, pp. S162–9, 2007.

[55] A. G. P. Kottapalli, M. Asadnia, J. Miao, and M. Triantafyllou, “Touch at a distance sensing: lateral-line inspired mems flow sensors,” *Bioinspiration & Biomimetics*, vol. 9, no. 4, p. 046011, 2014.

[56] A. Klein and H. Bleckmann, “Determination of object position, vortex shedding frequency and flow velocity using artificial lateral line canals,” *Beilstein Journal of Nanotechnology*, vol. 2, no. 1, pp. 276–283, 2011.

[57] A. T. Abdulsadda and X. Tan, “Underwater tracking of a moving dipole source using an artificial lateral line: algorithm and experimental validation with ionic polymer-metal composite flow sensors,” *Smart Materials and Structures*, vol. 22, no. 4, p. 045010, 2013.

[58] M. A. Sharif and X. Tan, “A pressure gradient sensor inspired by the canal neuromasts of fish,” in *SPIE Smart Structures and Materials+ Nondestructive Evaluation and Health Monitoring*. International Society for Optics and Photonics, 2018, pp. 979 827–979 827.

[59] H. Herzog, A. Klein, H. Bleckmann, P. Holik, S. Schmitz, G. Siebke, S. Tätzner, M. Lacher, and S. Steltenkamp, “$\mu-$biomimetic flow sensors introducing light-guiding pdms structures into mems,” *Bioinspiration & Biomimetics*, vol. 10, no. 3, p. 036001, 2015.

[60] H. Herzog, S. Steltenkamp, A. Klein, S. Tätzner, E. Schulze, and H. Bleckmann, “Micromachined flow sensors mimicking lateral line canal neuromasts,” *Micromachines*, vol. 6, no. 8, pp. 1189–1212, 2015.

[61] E.-S. Hassan, “Mathematical description of the stimuli to the lateral line system of fish derived from a three-dimensional flow field analysis,” *Biological Cybernetics*, vol. 66, no. 5, pp. 443–452, 1992.

[62] Z. Ren and K. Mohseni, “A model of the lateral line of fish for vortex sensing,” *Bioinspiration & Biomimetics*, vol. 7, no. 3, p. 036016, 2012.

[63] S. P. Windsor, S. E. Norris, S. M. Cameron, G. D. Mallinson, and J. C. Montgomery, “The flow fields involved in hydrodynamic imaging by blind mexican cave fish (astyanax fascia-

tus). part i: open water and heading towards a wall," *Journal of Experimental Biology*, vol. 213, no. 22, pp. 3819–3831, 2010.

[64] ——, "The flow fields involved in hydrodynamic imaging by blind mexican cave fish (astyanax fasciatus). part ii: gliding parallel to a wall," *Journal of Experimental Biology*, vol. 213, no. 22, pp. 3832–3842, 2010.

[65] M. J. McHenry, J. A. Strother, and S. M. Van Netten, "Mechanical filtering by the boundary layer and fluid–structure interaction in the superficial neuromast of the fish lateral line system," *Journal of Comparative Physiology A*, vol. 194, no. 9, pp. 795–810, 2008.

[66] S. M. van Netten, "Hydrodynamics of the excitation of the cupula in the fish canal lateral line," *The Journal of the Acoustical Society of America*, vol. 89, no. 1, pp. 310–319, 1991.

[67] ——, "Hydrodynamic detection by cupulae in a lateral line canal: functional relations between physics and physiology," *Biological cybernetics*, vol. 94, no. 1, pp. 67–85, 2006.

[68] M. A. Sharif, M. J. McHenry, and X. Tan, "Modeling of a bio-inspired canal-type lateral line system," in *ASME 2017 Conference on Smart Materials, Adaptive Structures and Intelligent Systems*. American Society of Mechanical Engineers, 2017, pp. V001T06A004–V001T06A004.

[69] H. L. M. A. Sharif and X. Tan, "Ionic polymer-metal composites torsional sensor: Physics-based modeling and experimental validation," *Smart Materials and Structures*, accepted.

[70] F. D. Lagor, L. D. DeVries, K. M. Waychoff, and D. A. Paley, "Bio-inspired flow sensing and control: Autonomous rheotaxis using distributed pressure measurements," in *Journal of Unmanned System Technology*. 1, pp.78-88,, 2013.

[71] A. T. Abdulsadda and X. Tan, "An artificial lateral line system using IPMC sensor arrays," *International Journal of Smart and Nano Materials*, vol. 3, no. 3, pp. 226–242, 2012.

[72] J. Chen, J. Engel, N. Chen, S. Pandya, S. Coombs, and C. Liu, "Artificial lateral line and hydrodynamic object tracking," in *Micro Electro Mechanical Systems, 2006. MEMS 2006 Istanbul. 19th IEEE International Conference on*. IEEE, 2006, pp. 694–697.

[73] Y. Yang, A. Klein, H. Bleckmann, and C. Liu, "Artificial lateral line canal for hydrodynamic detection," *Applied Physics Letters*, vol. 99, no. 2, p. 023701, 2011.

[74] E. Jacobsen and R. Lyons, "The sliding DFT," *IEEE Signal Processing Magazine*, vol. 20, no. 2, pp. 74–80, 2003.

[75] S. Shatara and X. Tan, “An efficient, time-of-flight-based underwater acoustic ranging system for small robotic fish,” *IEEE Journal of Oceanic Engineering*, vol. 35, no. 4, pp. 837–846, 2010.

[76] A. T. Abdulsadda and X. Tan, “Underwater tracking of a moving dipole source using an artificial lateral line: algorithm and experimental validation with ionic polymer–metal composite flow sensors,” *Smart Materials and Structures*, vol. 22, no. 4, p. 045010, 2013.

[77] A. Ahrari, H. Lei, M. A. Sharif, K. Deb, and X. Tan, “Design optimization of artificial lateral line system under uncertain conditions,” ser. 2015 IEEE Congress on Evolutionary Computation (CEC). Sendai, Japan: IEEE, 2015, pp. 1807–1814.

[78] G. Di Pasquale, S. Graziani, A. Pollicino, and S. Strazzeri, “A vortex-shedding flowmeter based on IPMCs,” *Smart Materials and Structures*, vol. 25, no. 1, p. 015011, 2015.

[79] T. Stalbaum, S. Trabia, Q. Shen, and K. J. Kim, “Fluid flow sensing with ionic polymer-metal composites,” in *SPIE Smart Structures and Materials+ Nondestructive Evaluation and Health Monitoring*. International Society for Optics and Photonics, 2016, pp. 97 982E–97 982E.

[80] F. Patane, C. Laschi, H. Miwa, E. Guglielmelli, P. Dario, and A. Takanishi, “Design and development of a biologically-inspired artificial vestibular system for robot heads,” in *Intelligent Robots and Systems, 2004.(IROS 2004). Proceedings. 2004 IEEE/RSJ International Conference on*, vol. 2. IEEE, 2004, pp. 1317–1322.

[81] C.-L. Li, C.-L. Lin, and C.-K. Chen, “Stabilizing postural control for emulated human balancing systems,” *International Journal of Engineering Science*, vol. 46, no. 11, pp. 1120–1135, 2008.

[82] M. Marcinkiewicz, R. Kaushik, I. Labutov, S. Parsons, and T. Raphan, “Learning to stabilize the head of a quadrupedal robot with an artificial vestibular system,” in *Robotics and Automation, 2009. ICRA’09. IEEE International Conference on*. IEEE, 2009, pp. 2512–2517.

[83] G. Ciaravella, U. Bertocchi, C. Stefanini, P. Dario, and A. Berthoz, “A vestibular interface for natural control of steering in the locomotion of robotic artifacts: preliminary experiments.”

[84] D. E. Angelaki and K. E. Cullen, “Vestibular system: the many facets of a multimodal sense,” *Annu. Rev. Neurosci.*, vol. 31, pp. 125–150, 2008.

[85] M. E. Gurtin, “The linear theory of elasticity,” in *Linear Theories of Elasticity and Thermoelasticity*. Springer, 1973, pp. 1–295.

[86] T. Ganley, D. L. Hung, G. Zhu, and X. Tan, "Modeling and inverse compensation of temperature-dependent ionic polymer–metal composite sensor dynamics," *IEEE/ASME Transactions on Mechatronics*, vol. 16, no. 1, pp. 80–89, 2011.

[87] D. Stathakis, "How many hidden layers and nodes?" *International Journal of Remote Sensing*, vol. 30, no. 8, pp. 2133–2147, 2009.

[88] *Fit Data with a Neural Network, Tutorial (R2014b)*, The Mathworks, Inc., Natick, Massachusetts, 2014.

[89] M. H. Sadd, *Elasticity: theory, applications, and numerics*. Academic Press, 2009.

[90] A. Dagamseh, T. Lammerink, M. Kolster, C. Bruinink, R. Wiegerink, and G. Krijnen, "Dipole-source localization using biomimetic flow-sensor arrays positioned as lateral-line system," *Sensors and actuators A: Physical*, vol. 162, no. 2, pp. 355–360, 2010.

[91] M. A. Sharif and X. Tan, "IPMC flow sensor exploiting self-generated vortices," *SPIE Smart Structures and Materials+ Nondestructive Evaluation and Health Monitoring*, p. 105941B, 2018.

[92] H. Lei, W. Li, and X. Tan, "Encapsulation of ionic polymer-metal composite (IPMC) sensors with thick parylene: Fabrication process and characterization results," *Sensors & Actuators: A. Physical*, vol. 217, pp. 1–12, 2014.

[93] H. Lei, C. Lim, and X. Tan, "Modeling and inverse compensation of dynamics of base-excited ionic polymer–metal composite sensors," *Journal of Intelligent Material Systems and Structures*, vol. 24, no. 13, pp. 1557–1571, 2013.

[94] M. A. Sharif and X. Tan, "A pressure gradient sensor inspired by the canal neuromasts of fish," in *Electroactive Polymer Actuators and Devices (EAPAD) XX*, vol. 10594. International Society for Optics and Photonics, 2018, p. 105941P.